POLITECNICO DI MILANO
DEPARTMENT OF ELECTRONICS,
INFORMATION AND BIOENGINEERING
DOCTORAL PROGRAMME IN ELECTRONICS ENGINEERING

MEMS MAGNETOMETERS: FROM APPLICATION SPECIFICATIONS TO THE DEVELOPMENT AND CHARACTERIZATION OF A PROTOTYPE BEYOND THE STATE OF THE ART

Doctoral Dissertation of:
Giacomo Laghi

Supervisor:
Prof. Antonio Longoni
Prof. Giacomo Langfelder

Tutor:
Prof. Carlo Fiorini

The Chair of the Doctoral Program:
Prof. Andrea Bonarini

2016 – XXIX Cycle

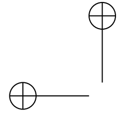
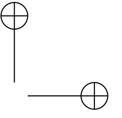

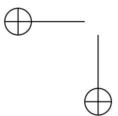
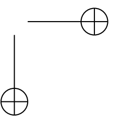

Acknowledgments

THis work would have never been possible without the precious help of the Sensors and Detectors Laboratory team, within the Department of Electronics, Information and Bioengineering of Politecnico di Milano.

The author would like to thank in a particular way Prof. Antonio Longoni and Prof. Giacomo Langfelder for their guidance and supervision along all the different project steps.

A great acknowledgment goes to Paolo Minotti for the very helpful collaboration, especially for the first part of this work and all the preliminary activities which led to the design and fabrication of the presented devices.

The author gratefully acknowledges also Luciana Molfetta and Cristiano Marra for their precious help in the electronics design, experimental characterization and data analysis.

The work was supported by ENIAC under grant agreement n. 325622 (Lab4MEMS project).

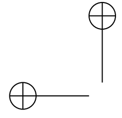
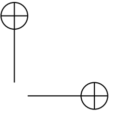
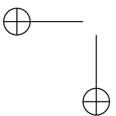
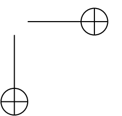

Abstract

MEMS magnetometers have been under research for more than a decade. A wide range of options have been explored: different physical principles - embedded magnetic materials, Lorentz-Force, parametric amplification - as well as different sensing techniques - optical, capacitive, piezoresistive. Despite this strong interest in the research world and the huge request of inertial sensors of the last years, particularly from the consumer world, nowadays there are no commercial products based on MEMS magnetometers.

Their most limiting features with respect to the current commercial technologies such as AMR, GMR and Hall, are a marked bandwidth-noise density trade-off and large area occupation. Consumer applications, which are the target of this work, are based on battery-powered objects, thus requiring the smallest and the less consuming devices possible.

This work aims to solve the presented issues - combining new techniques with refined existing ones - in order to bring Lorentz-Force based MEMS magnetic field sensors beyond the state of the art and towards their integration, as a commercial product, into a 6-axis eCompass (3-axis accelerometer + 3-axis magnetometer) for portable devices.

The most relevant technique exploited to enhance the performance of these sensors are:

- *Design of multi-loop structures:* in this work three 1-axis 10-loop structures are presented. Making the driving current recirculate within the three devices - in series - a 30-fold improvement is gained in terms of power dissipation required to obtain the desired resolution;

- This can be achieved, together with the *stability with temperature* and the *solution of the bandwidth-noise density trade-off* typical of Lorentz-Force MEMS magnetometers, thanks to:
  - *Off-resonance operation*: injection of a driving current at a frequency slightly lower than the resonance one;
  - MEMS resonator fabricated within the same package of the sensor. As a side but not negligible effect, this enables the possibility of re-using electronic stages well refined for MEMS gyroscopes, which have been deeply investigated in the last decades;
- The *area issue* is addressed in the last part of this work through the design of an innovative 3-axis monolithic structure, which guarantees a 15-fold saving in terms of area occupation with respect to the 3-axis solutions based on three uniaxial structures.

The industrial orientation of the work is also underlined by two additional factors:

- The *extensive characterization* performed on the sensor: aspects as the stability with temperature and vibration rejection have been taken into consideration. Usually in the research field these second order effects are not characterized, but they are essentials for the correct operation of a MEMS device as a commercial product;
- They are *fabricated in a standard industrial technology* (*ThELMA* by STMicroelectronics), respecting all its design rules and constraints. This potentially makes the sensor ready to be fabricated and put into the consumer market with strong guaranteed reliability and repeatability.

Summary

AN overview of literature, theory and issues of MEMS Lorentz-Force magnetometers is given in chapters 1 and 2. A complete sensing system based on a Lorentz-Force 3-axis device composed by three different 1-axis structure, together with its detailed characterization, is presented in chapter 3 and 4. In chapter 5 is finally presented a monolithic 3-axis structure which promises performance beyond the state of the art. It is also compatible with standard MEMS process (currently used for accelerometers and gyroscopes) and thus with the realization of 6- and 9-axis inertial combo sensors.

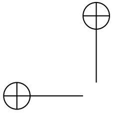
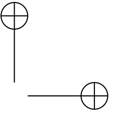

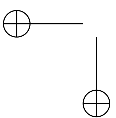

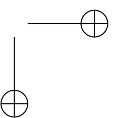

Contents

1 Magnetic field sensing: an eye on MEMS magnetometers **1**
1.1 Magnetic field sensing in consumer application 1
1.1.1 Compassing and navigation specifications 5
1.2 MEMS magnetometers as a real option 5
1.3 Lorentz-Force MEMS magnetometers 7
1.3.1 Operating principle 7
1.3.2 Phenomenological system overview 9
1.3.3 Resonance operation issues 10
1.3.4 State of the art 12
1.3.5 Considerations on power consumption 13

2 Theoretical analysis of Lorentz-Force MEMS Magnetometers **17**
2.1 Off-Resonance operation 17
2.1.1 Advantages with respect to resonance operation . . . 20
2.1.2 Critical points of off-resonance operation 22
2.2 Key parameters evaluation 22
2.2.1 Sensitivity (scale-factor, SF) 23
2.2.2 Resolution 24
2.2.3 Bandwidth 28
2.3 Offset 28
2.3.1 Offset in multi-loop architectures 31
2.3.2 Feed-through offset contribution 33
2.3.3 Offset compensation 34

3 A 3-axis MEMS magnetic field sensing system 37
3.1 Fabrication Process Challenges 37
3.2 Device Design 40
3.2.1 Module at a glance 40
3.2.2 Project criteria 43
3.2.3 Out-Of-Plane magnetic field sensing device 45
3.2.4 In-Plane magnetic field sensing device 51
3.2.5 Tang Resonator 54
3.3 Drive and sense electronics 55
3.3.1 Electronics overview 55
3.3.2 Sense electronics 57
3.3.3 Drive electronics 60
3.4 Key parameters prediction 65
3.4.1 Sensitivity 65
3.4.2 Electronic noise 65
3.4.3 Damping coefficient and total noise estimation 66
3.4.4 Considerations on power consumption 67

4 Performance characterization 69
4.1 Measurement Setup 69
4.2 Performance Evaluation 70
4.2.1 Sensitivity 70
4.2.2 Bandwidth 72
4.2.3 Noise 73
4.2.4 Offset 76
4.2.5 Temperature behavior 77
4.2.6 Accelerations rejection 78
4.2.7 Tolerance to magnetic field disturbances 83
4.2.8 Performance summary 84

5 An innovative single-mass 3-axis Lorentz-Force MEMS Magnetometer 85
5.1 Motivations and constraints 85
5.2 Structure design 86
5.2.1 Mechanical design 86
5.2.2 Electrical design 93
5.3 Key parameters evaluation 96
5.3.1 Sensitivity 96
5.3.2 Resolution 96
5.4 Future perspectives of the research 98
5.4.1 Future work on the presented device 98

5.4.2 Further performance improvements 100

Bibliography **105**

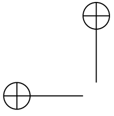
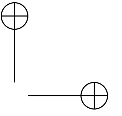

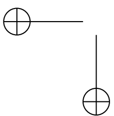
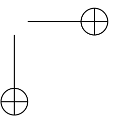

List of Abbreviations

BW - Bandwidth
CA - Charge Amplifier
DRIE - Deep Reactive Ion Etching
DOF - Degree Of Freedom
FEM - Finite Element Method
FOM - Figure Of Merit
FSR - Full Scale Range
IMU - Inertial Measurement Unit
INEMD - Intrinsic (MEMS only) Noise Equivalent Magnetic Density
IP - In Plane
LIA - Lock-In Amplifier
MEMS - Micro Electro Mechanical System
NEMD - (System) Noise Equivalent Magnetic Density
OOP - Out Of Plane
PSD - Power spectral Density
SNR - Signal-to-Noise ratio
T - Temperature
ThELMA - Thick Epitaxial Layer for Microactuators and Accelerometers
TCE - Temperature Coefficient of Young Modulus
TCF - Temperature Coefficient of Frequency

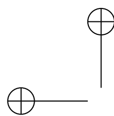
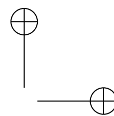
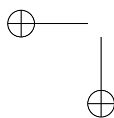
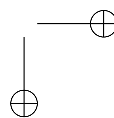

List of Symbols

α - Thermal expansion coefficient
β_{CC} - Modal constant
ϵ_0 - Vacuum permittivity
η - Electromechanical transduction factor
Δf - Frequency split between drive and resonance one
ΔV_{opt} - Optimum voltage difference between stators polarizations
A - Total facing area of all parallel plates and rotor
A_{1P} - Facing area of one parallel plate and rotor
b - Damping coefficient
b_{area} - Damping coefficient per unit area
B_{min} - Minimum detectable magnetic field
B_{ext} - External magnetic field
B_X, B_Y, B_Z - X-, Y- or Z- external magnetic field
C_{eq} - Equivalent capacitance of a MEMS resonator
C_F - Feedback Capacitance
C_P - Parasitic Capacitance
d - Torque arm
F_{el} - Electrostatic force
F_L - Lorentz Force
$f_0 = \omega_0 \ (2\pi)$ - Resonance frequency
f_d - Drive frequency
g - Gap between rotor and stator
G_{eln} - Electronic gain
i - Driving current

$\mathbf{i_{out}}$ - MEMS output sense current
$\mathbf{k}$ - Stiffness
$\mathbf{k_{eff}}$ - Effective stiffness
$\mathbf{k_B}$ - Boltzmann constant
$\mathbf{L}$ - Length on which the Lorentz Force acts
$\mathbf{L_{eq}}$ - Equivalent inductance of a MEMS resonator
$\mathbf{m}$ - mass
$\mathbf{N_e}$ - Number of electrons
$\mathbf{N_{loop}}$ - Number of current loops withing the structure
$\mathbf{N_{loop,eff}}$ - Effective number of loops
$\mathbf{N_{PP}}$ - Parallel plates number
$\mathbf{q}$ - Elementary charge
$\mathbf{Q}$ - Quality factor
$\mathbf{Q_{eff}}$ - Effective quality factor
$\mathbf{R_{eq}}$ - Equivalent resistance of a MEMS resonator
$\mathbf{R_F}$ - Feedback Resistance
$\mathbf{S_{n,R}}$, $\mathbf{S_{v,R}}$, $\mathbf{S_{B,R}}$ - PSD of the equivalent current thermal noise generator of a resistance in terms of, respectively: current, voltage at the CA output and magnetic field at the system input
$\mathbf{S_{n,I}}$, $\mathbf{S_{v,I}}$, $\mathbf{S_{B,I}}$ - PSD of the equivalent current noise generator of an operational amplifier in terms of, respectively: current, voltage at the CA output and magnetic field at the system input
$\mathbf{S_{n,V}}$, $\mathbf{S_{v,V}}$, $\mathbf{S_{B,V}}$ - PSD of the equivalent voltage noise generator of an operational amplifier in terms of, respectively: current, voltage at the CA output and magnetic field at the system input
$\mathbf{S_{F,M}}$, $\mathbf{S_{B,M}}$ - PSD of intrinsic MEMS noise in terms of force and magnetic field at the system input respectively
$\mathbf{S_{B,tot}}$ - PSD of the total noise at the system input in terms of magnetic field
SF - Scale Factor, Sensitivity
$\mathbf{SF_C}$, $\mathbf{SF_V}$ - Scale factor in terms of capacitance and voltage variation per unit magnetic field change
$\mathbf{T_{xF}}$ - Force-displacement transfer function
$\mathbf{v}$ - Electron velocity
$\mathbf{V_{bias}}$ - Stator biasing voltage
$\mathbf{V_{SR}}$ - Voltage between rotor and stator
$\mathbf{V_{rot}(t)}$ - Electrical offset (voltage)
$\mathbf{x_{acc}}$ - Displacement due to acceleration
$\mathbf{x_{os}}$ - Mechanical offset (displacement)

CHAPTER 1

Magnetic field sensing: an eye on MEMS magnetometers

1.1 Magnetic field sensing in consumer application

Magnetic field sensing has always been important for humankind. It all started more than 2000 years ago [1] with the invention of the first compasses for gems finding and direction finding in navigation. Nowadays magnetic field sensors are used in a very broad range of applications: from the military to the aerospace, automotive, consumer ones and many others. This has progressively led to the adoption of different technologies to sense different magnetic field ranges [2].
An overview of the most important applications is shown in figure 1.1, where a comparison between most diffused technologies for the consumer market, which is the target of this work, is also present. The aim is indeed to conceive and develop a 3-axis magnetic field sensor fabricated with MEMS technology, that would allow to build up - together with accelerometer and gyroscope - a single-chip, single-process, multi degrees of freedom (DOF) inertial measurement unit (IMU) with performance suitable for inertial navigation.

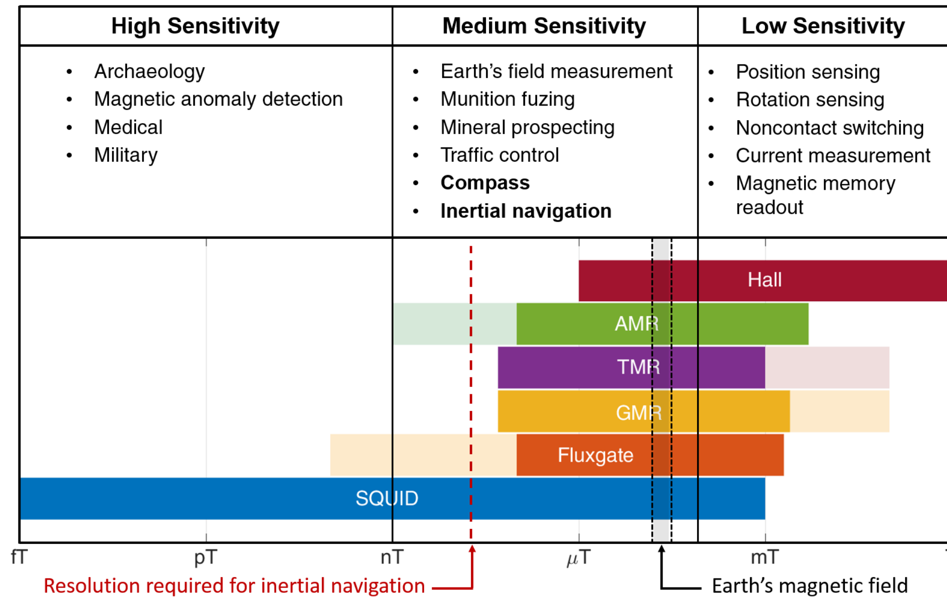

Figure 1.1: *Magnetometers applications and magnetic field ranges covered by the most important technologies for consumer application. The lighter bars stand for the potentiality of the technology that could be reached overcoming technological limitations. Squid is not a competitor for consumer application, but it is the most sensitive existing magnetometer.*

Table 1.1 reports the most important parameters used to characterize magnetic field sensors, together with the target values needed to achieve e-compass application.

An overview of the most diffused commercial products is given in table 1.2, with all the associated relevant parameters:

- *AMR (Anisotropic Magneto Resistance)* sensors [3] have been around for more than 50 years. They are characterized by a good resolution, but they exhibit limited FSR (due to linearity issues), and need for a set-reset procedure, which raises their power consumption. They are also based on magnetic materials, carrying with them problems related to hysteresis and magnetic domains flipping [4];
- *Hall effect* sensors are very cheap, compatible with CMOS technology and have a wide FSR. They are however characterized by poor resolution and high offset [5];

Parameter	Unit	Target
Sensitivity (scale-factor)	V/T	-
Resolution	nT/$\sqrt{\text{Hz}}$	100
Bandwidth	Hz	25
FSR	mT	± 5
Linearity FSR	%	1
Power consumption (sensor + ASIC)	mW	1
Package footprint	mm^2	2×2

Table 1.1: *Key parameters for the characterization of magnetic field sensors*

- *GMR (Giant Magneto Resistance) and TMR (Tunneling Magneto Resistance)* sensors [6] are based on magnetic materials, as AMR ones. They have a good resolution, but can be permanently damaged by high magnetic fields. They also exhibit high offset and temperature dependence [6];
- *Fluxgate* sensors [7] have a very good resolution, but need for magnetic materials. Their fabrication process is complex, they are bulky, have a limited bandwidth and exhibit a high power consumption and a limited FSR. In the end, they are not compatible with portable applications;
- *Magnetoinductive* sensors [3] are simple to design, low cost and low power. Nevertheless, they are bulky, difficult to align in the assembly process, and have a limited temperature range.

Product	Sensing Principle	FSR [±mT]	Current [µA]	Resolution [nT/$\sqrt{\mathrm{Hz}}$]	BW [Hz]	FOM [µTµA /$\sqrt{\mathrm{Hz}}$]	Size [mm^2]
			3-axis magnetometer				
AKM [8] AK8963	Hall	4.9	280	-	4	-	1.6x 1.6x 0.5
AKM [9] AK09911	Hall	4.9	2400	-	50	-	1.2x 1.2x 0.5
Bosch [10] BMM150	Fluxgate + Hall	1.3	4900	95	10	155	1.56x 1.56x 0.6
Freescale [11] MAG3110	MTJ (TMR)	1	900	64	40	19	2x2x 0.85
Honeywell [12] HMC5883	AMR	0.8	100	200	3.75	6.6	3x3x 0.9
MEMSIC [13] MMC3316	AMR	1.6	100	107	3.5	3.5	2x2x1
STM [14] LIS3MDL	AMR	1.6	270	101	10	9	2x2x1
Yamaha [15] YAS537	GMR	2	4000	300	-	400	1.2x 1.2
Alps [16] HSCDTD008	GMR	2.4	600	50	50	10	1.6x 1.6x 0.7
			6-axis eCompass				
Bosch [17] BMC156	MEMS + Fluxgate + Hall	1.3	4900	95	10	155	2.2x 2.2x 0.95
Freescale [18] FXOS8700	MEMS + MTJ (TMR)	1.2	150	85	50	4.2	3x3x 1.2
Kionix [19] KMX62	MEMS + MI	1.2	295	43	25	4.2	3x3x 0.9
mCube [20] MC6470	MEMS + GMR	2.4	600	50	50	10	2x2x 0.95
STM [21] LSM303AGR	MEMS + AMR	4.9	300	95	10	9.5	2x2x1

Table 1.2: *Most diffused commercial products for consumer application. For 6-axes eCompass the values (besides the size) are referred to magnetometers only; the other 3 axes are made up by a 3-axis MEMS accelerometer.*

1.1.1 Compassing and navigation specifications

Compassing and navigation deal with Earth magnetic field: for this reason a little of background on it becomes compulsory. In a first approximation, Earth can be seen as a magnetic dipole, whose orientation differs by a certain angle (*declination angle*) from the north-south geographic axis. Depending on geographical position, it also forms a certain angle with respect to the Earth surface (*inclination angle*).
For *compassing* the information of interest is the orientation of the magnetic field vector in the plane of the Earth surface, which, depending on the position, has an intensity between *20* and *70 μT*. In commercial eCompasses an accelerometer is usually integrated near the magnetometer, in order to compensate for the different orientation of the sensor with respect to the surface (*dip angle*).
For *navigation*, it is instead necessary to detect magnetic fields much smaller than the Earth one. The accuracy is usually defined in terms of rotation degrees the sensor is able to resolve. Looking at the sensor, this stands for the change in magnetic field intensity that corresponds to the relative rotation of sensor and magnetic field of a certain angle.

It is possible to define three main ranges of sensor accuracy [2], each one allowing to target a different application. Considering a 50 μT magnetic field intensity:

- *Cardinal Points*: 22° resolution, which leads to a minimum detectable field of 13 μT;
- *Heading*: 2° resolution, which leads to a minimum detectable field of 1.2 μT;
- *Navigation*: 0.2° resolution, which leads to a minimum detectable field of 120 nT.

1.2 MEMS magnetometers as a real option

MEMS magnetic field sensors have been studied for more than a decade [22], [2], but they are not yet available as commercial products in consumer application. Nevertheless the research in this field is very active as they have many potential advantages with respect to competing technologies.
Most of them are directly related to MEMS technology itself, that is nowadays the leading one for accelerometers and gyroscopes in the consumer field:

- Multi-DOF IMU could be fabricated in a single chip, leading to *area* and again *cost* saving. Indeed companies do not have to own more than one fabrication technology, also saving in terms of needed *equipment and maintenance*;
- Almost perfect alignment of accelerometer, gyroscope and magnetometer axes comes naturally, avoiding alignment and calibration problems typical of multi-DOF hybrid IMUs. This guarantees in a simpler way a better precision of the measurement, as it also depends on the misalignment between different sensors [23], [24];
- Unlike other technologies, they show an almost unlimited full-scale-range (FSR), and the sensing of magnetic field along all the three axes can be achieved with all planar structures.
- It is avoided the need for magnetic flux concentrators, used instead by AMR, GMR, TMR, Hall sensors to change the direction of the external field to a sensible one, or to mitigate the 1/f noise [25]. In this way there is no risk to incur in problems related to the thinning trend of packages for the next future.

Different approaches for building up MEMS magnetometers have been developed and tested during the past years, two of which turned out to be of particular interest:

- MEMS magnetic sensors exploiting the deposition of *magnetic materials* on top of the silicon structure
- MEMS magnetic sensors based on the *Lorentz-Force principle*
- MEMS-CMOS hybrid devices based on magnetoelectric effect [26]

For what concern the Lorentz-Force based MEMS magnetometers, an extensive treatise is presented in the following sections and chapters.
MEMS sensors with magnetic materials exploit the force generated by the response of the ferromagnetic material to the external magnetic field to create a torque on a MEMS structure. Interesting results have been achieved with this approach, such as in [27], the $0.3\mathrm{nT}/\sqrt{\mathrm{Hz}}$ resolution reached by DiLella et al. [28], or the work of Ettelt et al. in [29].

Being the force generated by the magnetic material itself in presence of an external magnetic field, this approach has the advantage - in terms of power consumption - of not requiring a current flowing through the device.

On the other hand, the presence of magnetic material is exactly the main issue of these devices. First of all it carries all problems related to hysteresis, and the consequent trade-off between sensitivity and maximum detectable field. Magnetic materials could also be permanently damaged if a large magnetic field occurs, unless reset coils are present, involving more area and power consumption. Moreover, unless modulating the external field in some way [25], the operation frequency of these kind of devices is the one of the external magnetic field, around DC. This could cause problems in terms of 1/f noise, if it turns out to be the dominant noise contribution as in [29].

1.3 Lorentz-Force MEMS magnetometers

1.3.1 Operating principle

Lorentz-force based MEMS magnetic sensors exploit the Lorentz force acting on one or more current-carrying beams to cause a movement of a suspended mass. This could be sensed in multiple ways: the most common ones are capacitive, piezoresistive and optical [22].

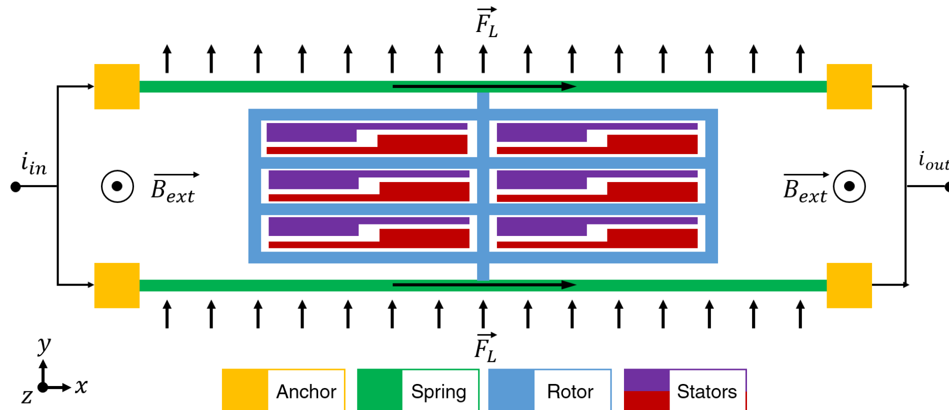

Figure 1.2: *Operating principle of a simple capacitive Lorentz-Force based MEMS magnetic sensor, sensitive to magnetic field along the z direction.*

Figure 1.2 shows an example of a Lorentz-Force MEMS magnetometer based on capacitive readout and sensitive to magnetic field along the z-direction (*out-of-plane, OOP*). In its simplest implementation, it is composed of two *springs* with both ends *anchored* to the substrate (*clamped-clamped beams*) through which a current is made flow. Their mid points hold a suspended frame (*rotor*), through which ideally no current flows and

that is suitably shaped to include nested anchored *stators*. In presence of an out-of-plane magnetic field, a Lorentz Force (F_L) arises on the springs. For a current carrying beam of length *L*, the force can be written as:

$$\mathbf{F_L} = N_e \cdot q \cdot \mathbf{v} \times \mathbf{B_{ext}} = L \cdot \mathbf{i} \times \mathbf{B_{ext}} \tag{1.1}$$

where $\mathrm{N_e}$ represents the number of electrons inside the beam, q is the elementary charge and v is the electrons velocity. This causes the springs to deform, giving place to a rigid displacement of the rotor. As the stators do not move, the capacitance value between rotor and stators changes in a way proportional to the external magnetic field. Being able to read the capacitance variation means thus being able to know the external applied magnetic field.

The first problem to face when dealing with Lorentz-Force magnetometers is Lorentz force itself. Considering typical dimensions of MEMS devices, Lorentz force generated by a typical value of magnetic field FSR ($\approx$ 5 mT) turns out to be approximately two orders of magnitude lower than Coriolis forces obtained for a typical rate gyroscope FSR ($\approx$ 2000 dps), and three orders of magnitude lower than the inertia one for a typical accelerometer FSR ($\approx$ 20 $\hat{\mathrm{g}}$). This difference directly affects the displacement (*x*) of the moving mass and thus the sense capacitance variation to be measured.

This led to the research of a way to improve the movement of the mass without increasing the current. The current increase would be the easiest way to boost the Lorentz-Force, but would also cause a directly proportional increase in power consumption.

Being MEMS devices modeled as second order spring-mass-damper [30], it is well known that their force-to-displacement transfer function is not constant in frequency: in particular a mechanical resonance frequency ($\mathrm{f_0}$) exists for the structure. An excitation at that frequency amplifies the motion amplitude by a quantity dependent on the quality factor (*Q*) and on the device stiffness (*k*).

$$\left|\frac{x}{F}\right|_{f=f_0} = \frac{Q}{k} \tag{1.2}$$

In a Lorentz-Force MEMS magnetometer this could be achieved by injecting a driving current at the structure resonance frequency [31]. In this way the force would be modulated and the displacement amplified.

1.3.2 Phenomenological system overview

Figure 1.3 shows a phenomenological overview of a magnetic field sensing system based on a Lorentz-Force MEMS magnetometer.

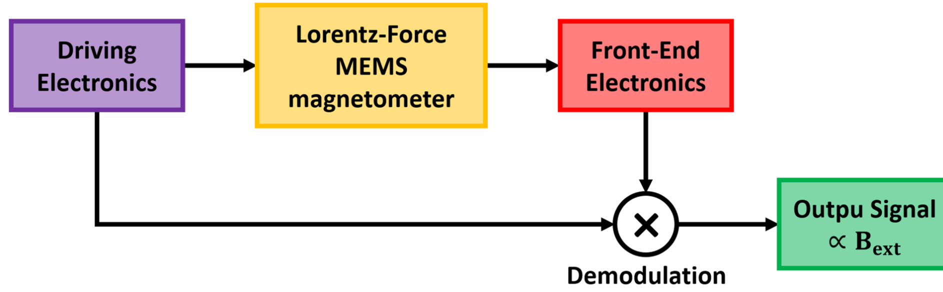

Figure 1.3: *Phenomenological overview of a magnetic field sensing system based on a Lorentz-Force MEMS magnetometer.*

The driving electronics (presented in section 3.3.3) allows to inject into the structure a current at its resonance frequency (f_m). An external magnetic field causes an amplitude modulation (AM) of the resonant displacement of the mass, which is also amplified by the Q factor, as stated by equation 1.2. This means that for the same external magnetic field - and thus for the same arising Lorentz-Force - the displacement of a resonance-operated device is greater with respect to a static-operated one of a factor Q/k, which is generally much higher than one. Modulation has also the advantage of putting the working condition of the system at a frequency typically in the order of 10 to 100 kHz, so that 1/f noise contribution can be neglected.

The displacement is capacitively transduced into an electrical signal, and read by means of the sense front-end electronics presented in section 3.3.2. At the output of the front-end stage, a voltage signal, whose frequency is equal to the one of the driving current (f_m) (summed to possible low-frequency components of the external field ($f_{B,L}$)) and whose amplitude is proportional to the magnetic field intensity, is obtained. In the frequency-domain, these low-frequency components appear as carrier sidebands, at frequencies $f_m + f_{B,L}$ and $f_m - f_{B,L}$.

A demodulation is then performed through a Lock-In amplifier, in order to recover the signal amplitude information, and thus the magnetic field intensity in which the sensor is plunged in. After the first demodulation step - a multiplication of the reference signal (f_m) by the signal at the output of the front-end electronics - these carriers are brought back to the baseband, at frequencies $f_{B,L}$ and $-f_{B,L}$. The second stage of the demodulation process, which is a low-pass filter, keep this baseband signal only, providing

a system output directly proportional to the external magnetic field, which follows all its time variations.

Performing this operation on all the three X-, Y- and Z- axes enables the continuous reconstruction of the intensity and direction of the 3D magnetic field vector.

1.3.3 Resonance operation issues

This *resonance operation* has some drawbacks though:

- *Bandwidth-Noise density trade-off*: in capacitive amplitude-modulation (AM) devices, resolution and bandwidth are both dependent on quality factor. Naming b the damping coefficient, the input referred rms magnetic field spectral noise density, which in this work is defined as *Intrinsic Noise Equivalent Magnetic Density* (*INEMD*) and whose origin is better explained and derived in section 2.2.2, can be written as:

$$b = \frac{\omega_0 m}{Q} \tag{1.3}$$

$$INEMD = \frac{2}{iL}\sqrt{4 \cdot k_B \cdot T \cdot b} \quad \left[\frac{T}{\sqrt{Hz}}\right] \tag{1.4}$$

  where m is the device mass, $\mathrm{k_B}$ is the Boltzmann constant, and T is the temperature in which the device is plunged, which is generally the ambient temperature ($\approx 300K$). Being the system bandwidth *BW* defined by the resonance peak of the device, also this parameter depends on quality factor. Comparing the two relations

$$INEMD \propto \sqrt{b} \qquad BW = \frac{f_0}{2Q} = \frac{f_0 b}{2\omega_0 m} \propto b \tag{1.5}$$

  it is clear that with a smaller damping coefficient both the resolution and bandwidth decrease, and while it is an improvement for the former, it represents a worsening for the latter. This leads, depending on application requirements, to the impossibility to simultaneously match bandwidth and resolution requirements;

- *Drive current generation* is not trivial, as the current frequency must always match the exact resonance frequency of the device. An oscillator circuit is needed, and two options are available for the resonant item:

  - *External* resonant item: this option is not viable because of the strong dependence of the MEMS resonance frequency on temperature, aging and process variance.
  - *MEMS itself* as resonant item: the motion induced by Lorentz-Force superposes to the motion caused by the oscillation for the generation of the frequency reference. This turns into a very huge offset in the output signal, lowering the dynamic range of the sensor. Additional electronics stage would also be needed for the compensation of the eventual phase error. Furthermore, the area needed for the electrodes responsible for the oscillation decreases the sensing area for the magnetic field induced motion, making this option hardly viable.

  Moreover, because of process spreads and environmental factors, and independently of the resonant item choice, in case of a 3-axis device *three different oscillator circuits* would be necessary.

- Quality factor strongly depends on temperature. This causes problems in terms of sensitivity and resolution long-term stability

- In capacitive amplitude-modulation (AM) devices with parallel-plate based readout, growing the number of parallel-plate cells ($\mathrm{N_{PP}}$), the sensitivity does not improve while the resolution worsens. Indeed the damping coefficient increases linearly with $\mathrm{N_{PP}}$. Being $\mathrm{b_{area}}$ the damping coefficient per unit area, mainly dependent on pressure, and $\mathrm{A_{1P}}$ the area of a parallel-plate cell:

$$b = b_{area} \cdot A_{1P} \cdot N_{PP} \tag{1.6}$$

  Sensitivity (scale-factor) expression is derived and explained in details in section 2.2.1. Evaluated in terms of capacitance variation corresponding to an external magnetic field variation ($\mathrm{SF_C}$), it turns out to be independent on *N*:

$$SF_C = \frac{\partial C}{\partial B} = \frac{\epsilon_0 \; i \; L}{2 \; \omega_0 \; g^2 \; b_{area}} \tag{1.7}$$

  where *g* is the capacitance gap at rest. The only ways for boosting the sensitivity without acting on the damping coefficient are increasing either the current i or the spring length L, incurring in an increasing of power consumption and area occupation respectively.

In order to compare sensors fabricated in different technologies, a *figure of merit* (FOM), firstly introduced in [32] is used in this work for performance evaluation. FOM is defined as resolution per unit bandwidth times unit driving current, and its measurement unit is:

$$FOM = \frac{INEMD \cdot i}{\sqrt{BW}} \quad \left[\frac{\mu T \cdot \mu A}{\sqrt{Hz}}\right] \tag{1.8}$$

The smaller this value, the better the sensor performance in terms of resolution-dissipation trade-off.

1.3.4 State of the art

Starting from the end of nineties [33], [34], almost all the works in literature exploit the Q-amplification of *resonance operation* in order to get the hugest achievable mass displacement. Furthermore, innovative methods, some of which are based on different readout topologies, have been developed in order to push up the sensitivity even more. Two of the most relevant examples are parametric amplification (PA) [35] and internal thermal-piezoresistive amplification [36], [37]. These two solutions deal with the increase of quality factor: in the former it is achieved through a modulation at twice the device frequency of the spring stiffness, which directly acts on Q, yet requiring a huge power consumption due to several added electronic blocks; in the latter through a positive feedback involving mechanical, electrical and thermal domain [1]. This leads to a high improvement in quality factor ($1.1{\cdot}10^6$) and resolution ($2.76\mathrm{pT}/\sqrt{\mathrm{Hz}}$), at the expense of a very low bandwidth (0.02 Hz), FSR (3.5 nT) and huge power consumption (several mA).
With the same purpose of amplifying the mass displacement, Kyynäräinen [38] proposed an approach based on the recirculation of the driving current inside a spiral loop. This solution had the advantage of amplifying the displacement without the needing of increasing the quality factor, but the fabrication process was costly and complicated, and the device occupies a huge area ($3.4 \times 3.4\mu\mathrm{m}^2$).

Other techniques have been proposed for offset and associated drifts reduction [39], which is still one of the most relevant issue of Lorentz-Force

[1] Based on piezoresistive sensing, the alternating compressive and tensile stress on the sensing element modulates its electrical resistance. With a constant bias current, this reflects in a modulation of its Joule heating. This turns the beam into a thermal actuation force generator, which can change the resonator vibration amplitude at resonance frequency, depending on the polarity of the material piezoresistive coefficient, which has to be negative to let this feedback work.

based MEMS devices. Force-rebalance principle applied to MEMS magnetometers has recently been investigated [40], showing promising results in terms of bandwidth and sensitivity stability with temperature.

A selection of the most relevant work, together with the related key parameters, are reported in table 1.3. Different devices are presented, with both different sensing topologies (capacitive, piezoresistive), and techniques (amplitude modulation, AM and frequency modulation, FM). Frequency modulated (FM) Lorentz-Force based magnetometers were firstly proposed [41] as a solution to overcome bandwidth-noise density trade-off typical of resonance operation in AM devices. These kind of technique was recently deeply investigated [42], [43], also giving good results in terms of sensitivity stability with temperature [44]. Performance are still not yet compatible with consumer applications: resolution performances are not good enough ($1 \div 20\mu\mathrm{T}/\sqrt{\mathrm{Hz}}$) and power consumption highly overcomes power budget limit ($3 \div 12\mathrm{mW}$ considering a 3V voltage supply).

1.3.5 Considerations on power consumption

One of the most important parameters for inertial navigation is power consumption. Indeed, during navigation, all sensors should be kept always on at their maximum resolution.

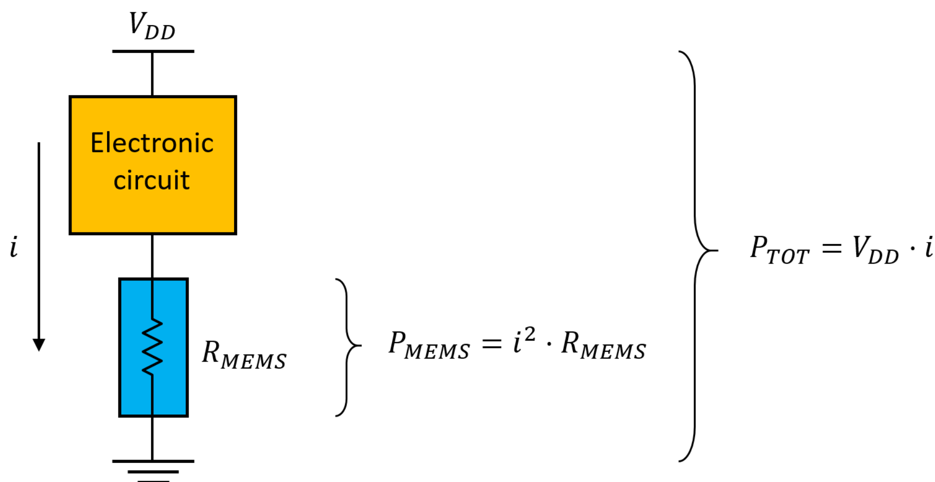

Figure 1.4: *Real power consumption in MEMS magnetometers is dependent on the driving current and on the supply voltage, which is application-constrained. It necessarily takes into account also the electronics in series with the MEMS device.*

Often, in the literature, the sensor power consumption is only ascribed to the driving current (*i*) and the resistance of the MEMS beams ($\mathrm{R_{MEMS}}$) in which this current flows ($\mathrm{P_{MEMS}} = \mathrm{i}^2 \cdot \mathrm{R_{MEMS}}$). As shown in figure 1.4, electronic circuits - at least for driving current generation - are unavoidably present in series with the magnetometer. The supply voltage $\mathrm{V_{DD}}$ is application-constrained, and in particular, for consumer application, is generally in the range 1.8 $\div$ 3.3 V. The total power consumption of the driving current has thus to be computed as $\mathrm{P_{TOT}} = \mathrm{V_{DD}} \cdot \mathrm{i}$, which is higher (often much higher) than $\mathrm{P_{MEMS}}$. The calculation of power consumption as $\mathrm{P_{MEMS}}$ only could lead to consider some devices suitable for consumer application when in practice they are not. Tables 1.2 and 1.3 report driving current instead of power consumption as a key parameter because, while the former is necessary for the correct device operation, the latter is consequently defined once the supply voltage $\mathrm{V_{DD}}$ has been chosen.

Name	Sensing	FSR [±mT]	Current [μA]	Resolution [$nT/\sqrt{Hz}$]	Pressure [mbar]	BW [Hz]	FOM [$\mu T \mu A/\sqrt{Hz}$]	Size [mm^2]
Kyynäräinen * [38]	Capacitive AM	0.2	100	70	0.006	2.5	2.3	> 3.4 x 3.4
Emmerich [34]	Capacitive AM	5	1000	5000	1	6	5000	> 1.5 x 0.8
Ren [45]	Capacitive AM	0.1	30000	59	0.1	0.26	1770	3 x 2
Kadar [33]	Capacitive AM	3	30000	-	0.05	25	-	1.4 x 3.8
Langfelder [46]	Capacitive AM	6	50	2000	0.25	160	100	1.1 x 0.15
Sung * [47]	Capacitive AM	1.2	4300	13800	26.7	2	19780	1 x 1
Chang * [48]	Capacitive AM	1.2	5900	403	1000	-	792	0.6 x 0.58
Thompson [35]	Capacitive AM PA	0.18	2670	87	1000	1	232	> 2.5 x 1.5
Li [42]	Capacitive FM	8	4000	20000	-	-	80000	1.2 x 0.7
Li [44]	Capacitive FM	3.6	900	500	-	50	450	0.4 x 0.4
Sonmezoglu [40]	Capacitive FM	0.4	5000	360	-	38	1800	1 x 1
Zhang [43]	Capacitive FM	100	1000	9000	0.006	1	9000	> 0.8 x 0.6
Bahreyni [41]	Capacitive FM	25	10000	200	0.002	1.33	2000	> 0.52 x 0.5
Mehdizadeh [37]	Piezoresistive AM	9	28000	10	1000	25	280	> 1.5 x 1.5
Kumar [36]	Piezoresistive AM	3.5 nT	7245	2.76pT	1000	0.02	0.02	> 1.5 x 1.5
Herrera-May [49]	Piezoresistive AM	2	30000	43	1000	120	1290	0.7 x 0.45

Table 1.3: ** = Three axial device. Comparison of the most important bibliography works on Lorentz-Force MEMS magnetometers*

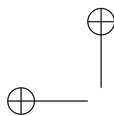
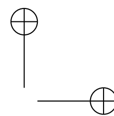

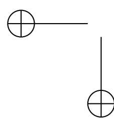
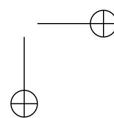

CHAPTER 2

Theoretical analysis of Lorentz-Force MEMS Magnetometers

2.1 Off-Resonance operation

Section 1.3.1 clearly shows that it is hardly possible to rely on a MEMS Lorentz-Force magnetometer based on resonance operation for consumer application, especially when considering a 3-axis sensor, which is required for navigation. Apart from the strategies listed in section 1.3.4, another technique has been recently proposed [32] and patented [50] to overcome all the limitations peculiar to resonance operation. This technique, called *off-resonance* or *mode-split operation*, is further developed adding new ideas, and fully exploited in this work.

Off-resonance operation is defined as the operation of a sensor with an excitation force at a frequency (f_d) slightly different from the mechanical resonance (f_0). The *mismatch* or *split* between the two frequencies is defined as:

$$\Delta f = |f_0 - f_d| \qquad (2.1)$$

It is a well known technique used in gyroscopes, creating a mismatch between sense and drive mode natural frequencies, in order to make the sensor robust to environmental changes and increase its bandwidth [51]. For Lorentz-Force MEMS magnetometers this is accomplished by the injection of the driving current with a frequency mismatch Δf with respect to f_0. The frequency split must be much lower than f_0, and at the same time much higher than the mechanical bandwidth of the resonant peak, as given by equation 1.5. For a typical device operating around 20 kHz with a Q of 1000, acceptable values of Δf could be within $100 \div 2000$Hz.

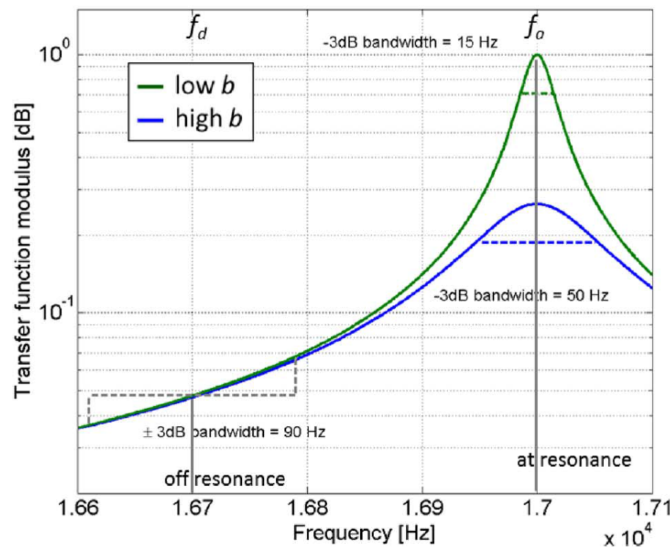

Figure 2.1: *Bandwidth comparison between resonance and off-resonance operation for two different devices with $f_0 = 17kHz$, the first featuring a Q of 600 (resonant peak $BW \approx 15Hz$) while the second with a Q of 150 (resonant peak $BW \approx 50Hz$). In the hypothesis of off-resonance operation with a frequency split $\Delta f = 300Hz$, the bandwidth turns out to be independent of the quality factor ($\approx 90Hz$), and higher than the one obtained for resonance operation.*

As shown in the sample plot of figure 2.1, in this condition the force-to-displacement transfer function turns out to be almost insensible to a change in quality factor. This leads to the definition of a constant gain, called *effective quality factor* (Q_{eff}), that is dependent on Δf but very poorly on Q. Indeed, if the the force-to-displacement transfer function of a MEMS device is considered:

$$T_{xF}(j\omega) = \frac{x(j\omega)}{F(f\omega)} = \frac{1}{m} \cdot \frac{1}{(j\omega)^2 + \frac{\omega_0}{Q} j\omega + \omega_0^2} \tag{2.2}$$

it is possible to evaluate it at the operation frequency f_d substituting ω with $\omega_d = 2\pi f_d$:

$$|T_{xF}(j\omega_d)| = \left|\frac{x(j\omega_d)}{f(j\omega_d)}\right| = \frac{1}{m} \cdot \frac{1}{\sqrt{(\omega_0^2 - \omega_d^2)^2 + \left(\frac{\omega_0}{Q}\omega_d\right)^2}} \tag{2.3}$$

In typical operation conditions of a device with $f_0 \approx 20\text{kHz}$, $Q \approx 1000$ and $\Delta f \approx 300\text{Hz}$, the following requirements are respected:

- $Q \gg 1$
- $\Delta f \ll f_0$
- $\Delta f \gg \frac{f_0}{2Q}$

The force-to-displacement transfer function can be thus simplified in the region around f_d:

$$|T_{xF}(j\omega_d)| = \left|\frac{x(j\omega_d)}{f(j\omega_d)}\right| = \frac{1}{m} \cdot \frac{1}{\sqrt{\omega_0^4 + \omega_d^4 - 2\omega_0^2\omega_d^2 + \cancel{\left(\frac{\omega_0}{Q}\omega_d\right)^2}}} \tag{2.4}$$

and expressing the operating frequency in terms of frequency split $\omega_d = \omega_0 - \Delta\omega$, it is possible to obtain an even more compact expression:

$$|T_{xF}(j\omega_d)| = \left|\frac{x(j\omega_d)}{f(j\omega_d)}\right| \approx \frac{1}{m} \cdot \frac{1}{2\omega_0\Delta\omega - \cancel{\Delta\omega^2}} = \frac{1}{k}\frac{\omega_0}{2\Delta\omega} \tag{2.5}$$

An *effective quality factor* Q_{eff} can thus be defined

$$Q_{eff} = \frac{\omega_0}{2\Delta\omega} \quad \rightarrow \quad \left|\frac{x(j\omega_d)}{f(j\omega_d)}\right| = \frac{Q_{eff}}{k} \tag{2.6}$$

It represents the amplification obtained, with respect to DC operation, when driving the device with a mismatch Δf from its mechanical resonance frequency f_0.

2.1.1 Advantages with respect to resonance operation

Operating off-resonance with a frequency mismatch $\Delta\mathrm{f}$ and a resulting residual amplification $\mathrm{Q_{eff}}$ independent of Q inherently minimizes all the issues related to resonance operation.

- *Bandwidth-Noise density trade-off* is solved.
  - *Bandwidth is no more dependent on b.* As shown in figure 2.1, for different Q (and thus b) values the bandwidth does not change. It is always defined as the $\pm 3\mathrm{dB}$ value of the force-to-displacement transfer function, and choosing a suitable frequency split value $\Delta\mathrm{f}$, BW turns out to be much higher than the one defined by the resonance peak. In real applications it is easy to obtain a $\pm 3\mathrm{dB}$ BW value higher than the application requirements, therefore the bandwidth will be is generally selected by the front-end acquisition electronic chain [46].
  - *Intrinsic resolution (INEMD) still depends on b*, being its expression the same as in resonance operation (equation 1.4). Indeed it does not depend on the device motion but, besides the driving current, only on geometrical and environmental parameters.

  In principle it could be possible to improve sensor intrinsic resolution, even in resonance operation, acting on *i* or *L*, but it would violate the two most critical constraints of consumer application, respectively being *power consumption* and *area*.

  Exploiting off-resonance operation it becomes possible to improve resolution acting on the damping coefficient *b*, either lowering package pressure or acting on the stator geometry [52], without any impact on the bandwidth.

- *Drive current generation* problem is made easier to solve.
  It becomes compulsory the use of an external resonator for the oscillator circuit selecting the drive current frequency. Opposite to resonance operation, drive current frequency has not to exactly match the device resonance frequency: the $\mathrm{Q_{eff}}$ value is tolerant to resonance frequency variations. Consider the typical case already presented in section 2.1 of a device with $\mathrm{f_0} = 20$ kHz, Q = 1000 and $\Delta\mathrm{f} = 300$ Hz. For an $\mathrm{f_0}$ variation of $\partial\mathrm{f} = \pm 5\mathrm{Hz}$, sensitivity (or scale-factor, SF) varies respectively:

– *Resonance operation:*

$$SF_{f_0 \pm \partial f} = \frac{SF_{f_0}}{\sqrt{2}} \approx 0.707 \cdot SF_{f_0} \tag{2.7}$$

– *Off-resonance operation:*

$$SF_{f_0 \pm \partial f} = \frac{f_0 \pm \partial_f}{2(\Delta f \pm \partial f)} \approx 0.984 \cdot SF_{f_0} \tag{2.8}$$

In the hypothesis of a 3-axis device, this enables the use a unique drive frequency for all the three devices, allowing the implementation of only one oscillator circuit, providing about 3-fold saving in power consumption.

- *Sensitivity long-term stability problem* is solved.
  Indeed, being the sensitivity less dependent on Q, off-resonance operation minimizes the effects on the former due to variations of the latter with temperature or other environmental parameters.

- *Sensitivity improves with parallel-plate cells number increase.*
  In resonance operation the $\mathrm{N_{PP}}$ term was present both in the expression of Q and in the $\mathrm{C_0}$ one, so it was canceled out. In off-resonance operation, instead, having $\mathrm{Q_{eff}}$ in place of Q, $\mathrm{N_{PP}}$ is only present in the $\mathrm{C_0}$ expression. As visible in equation 2.14, sensitivity is directly proportional to $\mathrm{C_0}$, and thus to $\mathrm{N_{PP}}$. Compatibly with the area occupation requirement for the specific application, this gives a term of freedom for increasing the sensitivity without acting on power consumption.

- *Intrinsic SNR is the same as resonance operation.*
  In terms of mass displacement, indeed, considering the bandwidth to be application-constrained and thus equal for the two operating conditions, the SNR can be written as:

$$SNR_{resonance} = \frac{F_L \cdot \cancel{\frac{Q}{k}}}{\sqrt{4k_B T b \cancel{\left(\frac{Q}{k}\right)^2} BW}} \tag{2.9}$$

$$SNR_{off-resonance} = \frac{F_L \cdot \cancel{\frac{Q_{eff}}{k}}}{\sqrt{4k_B T b \cancel{\left(\frac{Q_{eff}}{k}\right)^2} BW}} \tag{2.10}$$

2.1.2 Critical points of off-resonance operation

The main issue in off-resonance operation is related to a marked decrease in sensitivity:

$$\frac{SF_{off-resonance}}{SF_{resonance}} = \frac{Q_{eff}}{Q} \tag{2.11}$$

This means smaller capacitance variation, and a consequent lower electric signal at the MEMS output, which may lead to higher power consumption in the front-end electronics chain to guarantee the same input-referred resolution. It is thus necessary to increase the Lorentz Force acting on the device with a geometrical approach.

▷ The solution adopted in this work is based on the recirculation of the driving current inside the device, which will improve the sensitivity in a way directly proportional to the loop number. All the beneficial effects of this solution are detailed in section 2.2.

Even if the issue related to *drive frequency generation* is partially solved, it is still a critical point also in off-resonance operation. The deviation from the theoretical sensitivity is indeed not compatible with navigation application.

▷ In the following a solution to this issue is proposed (chapter 3) and validated (chapter 4). A MEMS resonator, built within the same package of the sensor, is chosen as frequency-selector element. Provided that both sensor and resonator are well-designed, a self-tracking between reference and magnetometers frequency changes versus temperature is achieved, so to keep frequency mismatch Δf, and thus sensitivity, well stable.

2.2 Key parameters evaluation

In figure 2.2 a structure illustrating the principle of multi-loop geometry is presented. Its operating principle is similar to the one of figure 1.2: the main difference is given by the presence of a certain number of loops ($\mathrm{N_{loop}}$) in which the same driving current flows. It is thus clear that the total Lorentz force acting on the structure, for the same external magnetic field, is higher with respect to the simple case of figure 1.2 by a factor $\mathrm{N_{loop}}$.

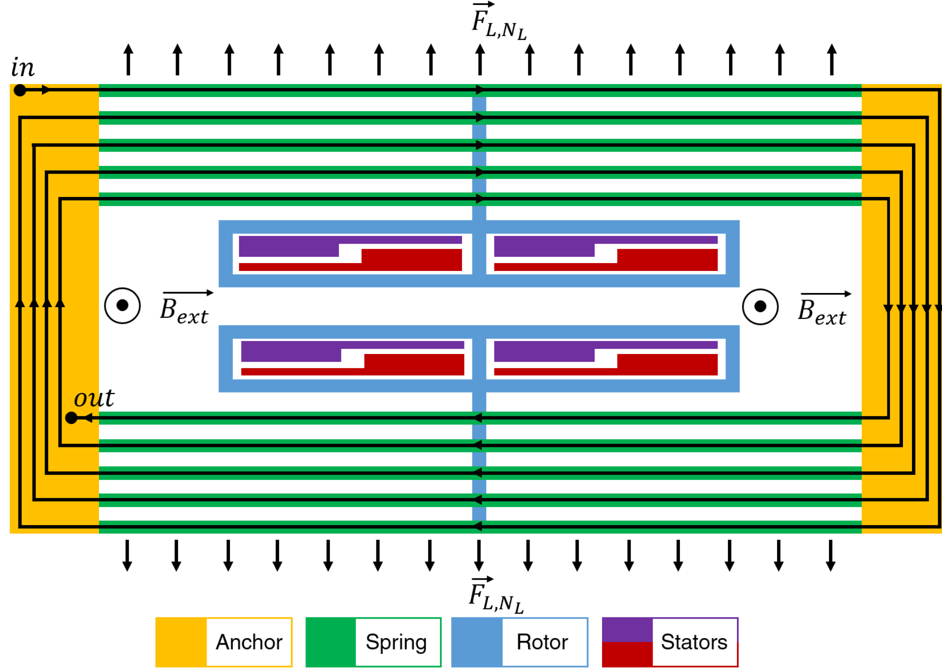

Figure 2.2: *Simplified example of a multi-loop Lorentz-Force MEMS magnetometer geometry sensible to magnetic field in z-direction (OOP). In the presented case the loop number* $\mathrm{N_{loop}}$ *is 5.*

2.2.1 Sensitivity (scale-factor, SF)

In a more rigorous way, the sensitivity, or scale-factor (SF), of a capacitive Lorentz-Force MEMS magnetometer based on a structure as the one presented in figure 2.2 could be written as the variation of the capacitance relative to a variation of the external magnetic field:

$$SF_C = \frac{\partial C}{\partial B} = \frac{\partial F_L}{\partial B} \cdot \frac{\partial x}{\partial F_L} \cdot \frac{\partial C}{\partial x} \tag{2.12}$$

Operating the device off-resonance, the injection of a driving current with frequency $\mathrm{f_d}$ causes a Lorentz force at the same frequency to act on the structure springs. This force is amplified by a factor $\mathrm{N_{loop}}$ with respect to the case of figure 1.2:

$$F_L = B \cdot i \cdot L \cdot \mathbf{N_{loop}} \tag{2.13}$$

As seen in section 2.1, the force-to-displacement transfer function ($\partial x/\partial F_L$) in this operating condition is $\mathrm{Q_{eff}/k_{eff}}$. $\mathrm{k_{eff}}$ is the effective stiffness of the

device in terms of N/m, which also takes into account the distributed nature of Lorentz-Force acting on the springs. The capacitance transduction factor $\partial C/\partial x = 2 \cdot \mathrm{C_0/g}$ is the typical one of differential parallel-plate readout architecture [30], where $\mathrm{C_0}$ and g are the rest capacitance and gap respectively. The derived expression for differential sensitivity ends up to be directly proportional to the loop number $\mathrm{N_{loop}}$:

$$SF_C = \frac{\partial C}{\partial B} = \mathbf{N_{loop}}\, i\, L \cdot \frac{Q_{eff}}{k_{eff}} \cdot 2\frac{C_0}{g} \tag{2.14}$$

2.2.2 Resolution

As in all sensor-based systems, two are the main noise contributions: the intrinsic sensor one and the electronics one. This is true also for MEMS-based systems:

- *Sensor Noise:* the main noise contribution for a MEMS device is the intrinsic Brownian one, which is generated by gas particles-MEMS rotor walls interactions [53]. Its power spectral density in terms of force $[\mathrm{N^2/Hz}]$ is:

$$S_{F,M} = 4k_BTb \tag{2.15}$$

  where the damping coefficient *b* is mainly dependent on pressure and on the structure geometry. For the magnetometer case it is convenient to write all noise contributions in terms of input-referred magnetic field, thus obtaining the system resolution (*INEMD*) in terms of $\left[\mathrm{T}/\sqrt{\mathrm{Hz}}\right]$ (i.e. in terms of magnetic field noise density). For the Brownian contribution:

$$INEMD = \sqrt{S_{B,M}} = \frac{\sqrt{S_{F,M}}}{\frac{\partial F}{\partial B}} = \frac{2}{\mathbf{N_{loop}}\, i\, L}\sqrt{4k_BTb} \tag{2.16}$$

  The factor 2 arises because the noise, dominated by squeeze-film damping phenomena in parallel-plates cells, directly acts on the suspended frame, and not distributed along the springs like Lorentz force does.

- *Electronic noise:* supposing an operational-amplifier based front-end stage with a feedback resistance and capacitance [54], the main electronics noise contributions are due to equivalent *voltage* and *current*

noise of the op-amp and to the *Johnson noise* contribution of the feedback resistance.

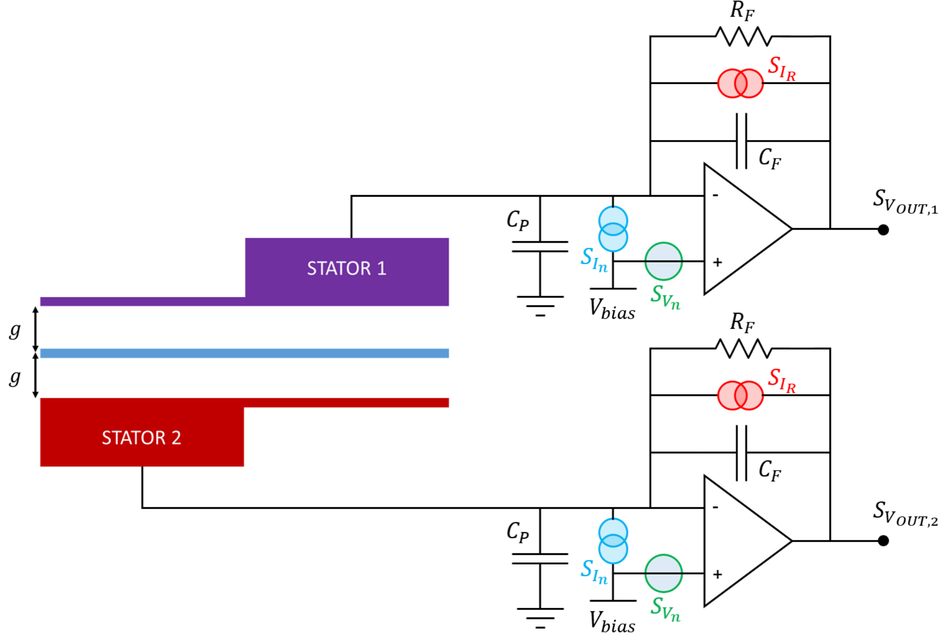

Figure 2.3: *Main electronics noise contribution of a front-end electronics based on an operational-amplifier with feedback resistance and capacitance.*

Referring to figure 2.3, a parasitic capacitance including i.e. pads and interconnections is always present at the op-amps virtual ground. Naming $\mathrm{S}_{\mathrm{n,V}}$ and $\mathrm{S}_{\mathrm{n,I}}$ the voltage and current equivalent noise generators of the operational amplifier, and $\mathrm{S}_{\mathrm{n,R}}$ the current equivalent noise generator of the feedback resistance, it is convenient to write all their contributions in terms of input-referred magnetic field. This makes them comparable to intrinsic device noise, and directly gives information about total system resolution. Supposing to use the stage as an integrator:

– *Voltage noise of the operational amplifier* can be written, in terms of voltage noise density at the output, as:

$$S_{v,V} \approx S_{n,V} \cdot \left(1 + \frac{C_P}{C_F}\right)^2 \tag{2.17}$$

neglecting the MEMS capacitance C_0, being this typically much lower (of an order of magnitude or more) with respect to the parasitic capacitance C_P.
The transfer function between capacitance variation and output voltage variation is:

$$\frac{\partial V}{\partial C} = \frac{V_{bias}}{C_F} \tag{2.18}$$

thus leading to a single-ended sensitivity in terms of voltage for an external magnetic field variation of:

$$SF_V = \frac{\partial V}{\partial B} = SF_C \cdot \frac{\partial V}{\partial C} = \mathbf{N_{loop}}\, i\, L \cdot \frac{Q_{eff}}{k_{eff}} \cdot \frac{C_0}{g} \cdot \frac{V_{bias}}{C_F} \tag{2.19}$$

Considering the two stages shown in figure 2.3, operational amplifier total voltage noise can finally be brought back to the system input, in terms of magnetic field noise density:

$$S_{B,V} = \frac{2 \cdot S_{v,V}}{SF_V} = \\ = 2 \cdot S_{n,V} \cdot \left(\frac{C_P}{V_{bias}} \frac{g \cdot k_{eff}}{C_0\, Q_{eff}\, i\, L \cdot \mathbf{N_{loop}}} \right)^2 \tag{2.20}$$

where the factor 2 is due to the presence of the two identical front-end stages.

- *Current noise of the operational amplifier* is directly transferred as a current noise at the output. In order to bring back this contribution at system input, it is useful to define a transfer function between the external magnetic field and the current at the operational amplifier output. At one stator output, the current can be written as:

$$i_{out} = \frac{d}{dt}[C \cdot V] = V \cdot \frac{\partial C}{\partial t} + C \cdot \frac{\partial V}{\partial t} \tag{2.21}$$

where *C* and *V* are respectively the single-ended capacitance and voltage difference between rotor and stator. Being the voltage difference constant and equal to V_{bias}, this expression can be simplified:

$$i_{out} = V \cdot \frac{\partial C}{\partial t} = V \cdot \frac{\partial C}{\partial x} \cdot \frac{\partial x}{\partial t} = V \cdot \frac{\partial C}{\cancel{x}} \cdot \cancel{x} \omega_d \tag{2.22}$$

This defines the sensitivity between external magnetic field and output current:

$$SF_i = SF_C \cdot \frac{\partial i_{out}}{\partial C} = \mathbf{N_{loop}}\, i\, L \cdot \frac{Q_{eff}}{k_{eff}} \cdot \frac{C_0}{g} \cdot \omega_d \cdot V_{bias} \tag{2.23}$$

This leads the current noise of the operational amplifier to be expressed in terms of magnetic field density at the system input as:

$$\begin{aligned} S_{B,I} = \frac{2 \cdot S_{n,I}}{SF_i} = \\ = 2 \cdot S_{n,I} \cdot \left(\frac{g \cdot k_{eff}}{C_0\, V_{bias}\, Q_{eff}\, \omega_d\, i\, L \cdot \mathbf{N_{loop}}} \right)^2 \end{aligned} \tag{2.24}$$

– *Johnson noise of the feedback resistance* is also directly transferred as a current noise at the output. Bringing it back to the system input as the current noise of the operational amplifier:

$$\begin{aligned} S_{B,R} = \frac{2 \cdot S_{n,R}}{SF_i} = \\ = \frac{8 k_B T}{R_F} \cdot \left(\frac{g \cdot k_{eff}}{C_0\, V_{bias}\, Q_{eff}\, \omega_d\, i\, L \cdot \mathbf{N_{loop}}} \right)^2 \end{aligned} \tag{2.25}$$

From these calculations is possible to write an expression for the total input referred rms magnetic field spectral noise density of the system, which in this work is addressed as *Noise Equivalent Magnetic Density (NEMD)* $\left[\mathrm{T}/\sqrt{\mathrm{Hz}}\right]$:

$$\begin{aligned} NEMD = \sqrt{S_{B,tot}} = \sqrt{S_{B,M} + S_{B,V} + S_{B,I} + S_{B,R}} = \\ = \frac{1}{iL\mathbf{N_{loop}}} \cdot \sqrt{4\,(k_B T b)^2 + \left(\sqrt{2 \cdot S_{n,V}} \cdot \frac{C_P}{V_{bias}} \cdot \frac{g \cdot k_{eff}}{C_0\, Q_{eff}} \right)^2 +} \\ \overline{+ \left(\sqrt{\frac{8 k_B T}{R_F} + 2 \cdot S_{n,I}} \cdot \frac{g \cdot k_{eff}}{C_0\, V_{bias}\, Q_{eff}\, \omega_d} \right)^2} \end{aligned} \tag{2.26}$$

Multiplying the obtained noise by the square root of the chosen bandwidth, the minimum measurable magnetic field for a given bandwidth is finally obtained.

Adding re-circulation loops improves all noise contributions, being device intrinsic or electronics one, leading thus to a beneficial effect both in terms of sensitivity and resolution of the system.

The only limitation to N_{loop} increase is the area occupation of the device, which is an important parameter of merit when speaking of consumer application. Devices targeting consumer applications should also be low power consuming. Even if the increase of the loop number could seem an issue from this point of view, because of the resistance increase, in chapter 3 it is shown that it is not, thanks to a particular technological implementation involving low resistance metal layer for the current path definition.

2.2.3 Bandwidth

As stated in section 2.1, the bandwidth of off-resonance operated devices is reasonably independent on the quality factor. Provided to correctly set the frequency mismatch Δf, this gives more freedom in the bandwidth choice. Referring to figure 2.1, as an empiric rule, the $\pm 3dB$ bandwidth can be considered to be $BW \approx \Delta f/3$. Indeed, in order to avoid the amplification of harmonics at frequency $f = \Delta f$, and to control the minimum measurable field ($B_{min} = NEMD \cdot \sqrt{BW}$), it is generally preferred to electronically filter the bandwidth. To guarantee this possibility, resonance peak has not to occur before electronic filtering: using as an example a Δf of 300 Hz, a BW of 50 Hz is readily achievable [46].

2.3 Offset

Offset is a common issue when dealing with MEMS devices. In several case, as accelerometers [55], due to stresses and typical low stiffness, and in gyroscopes, due to quadrature error [56], it reaches magnitudes even larger than the FSR. This is also the case of MEMS magnetometers. Taking into account the simplified structure of figure 1.2, whose resistive model is pictured in figure 2.4, the current signal at each stator output can be written as in equation 2.21. It shows that two are the terms which could generate an undesired, non-zero signal: a capacitance (C) variation or a voltage (V_{SR}) variation between rotor and stators. Two are thus the typical offset sources:

- *Electrical*: assuming the structure to be perfectly symmetric from a mechanical point of view, the voltage on the rotor is ideally con-

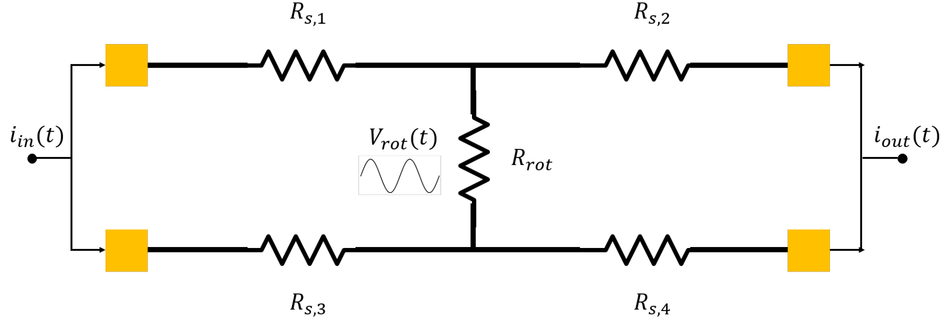

Figure 2.4: *Simplified resistive model of the structure of figure 1.2.*

stant in all its points. Nevertheless, due to fabrication process non-uniformities, the four ideally identical resistances ($R_{s,1}, R_{s,2}, R_{s,3}$ and $R_{s,4}$) turn out to be different. In this condition a residual voltage on the rotor, which is time-varying at the drive current frequency, appears ($V_{rot}(t)$).

- $C \cdot \frac{\partial V_{SR}}{\partial t}$ is not null, but exactly equal for the two stators of the differential parallel-plate cell. The two signals would be thus automatically canceled out in any differential readout;
- $V_{SR} \cdot \frac{\partial C}{\partial t}$ (struck through) is always null: in the hypothesis of a mechanically balanced structures, $C_1 = C_2$, so the two electrostatic forces are always equal, holding the rotor in its rest position.

If only this contribution exists, no offset signal is visible at the output.

- *Mechanical*: so far it has been assumed that, in absence of magnetic field, the rotor is ideally in the middle between the two stators. Also assuming the structure ideally symmetric from an electrical point of view, due to residual stresses, in the release fabrication step the rotor could be displaced from its ideal position of a quantity x_{os}, as shown in figure 2.5.
  - $C \cdot \frac{\partial V_{SR}}{\partial t}$ (struck through) is null. In the ideal case of perfectly balanced resistances R_s, the voltage difference between rotor and stators is constant;
  - $V_{SR} \cdot \frac{\partial C}{\partial t}$ is, initially, not null. The two electrostatic forces are indeed not equal because of the different gap between rotor and

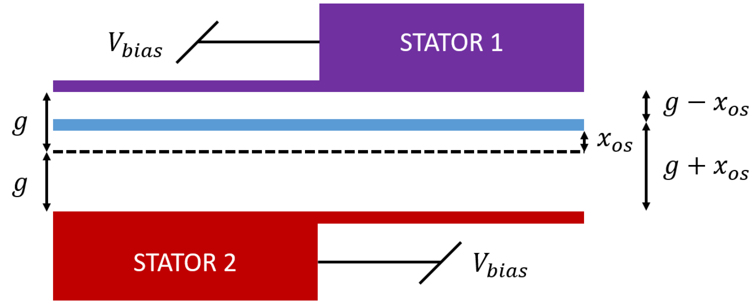

Figure 2.5: *The rotor is displaced by its ideal rest position of a quantity x_{os} toward one stator. This is called mechanical offset.*

stators. This leads to a movement of the rotor toward an equilibrium position, causing a capacitance variation in time and a consequent offset signal. As shown in the simulation result presented in figure 2.6, once equilibrium has been achieved, no more offset signal is observed at the output if no external magnetic field is applied.

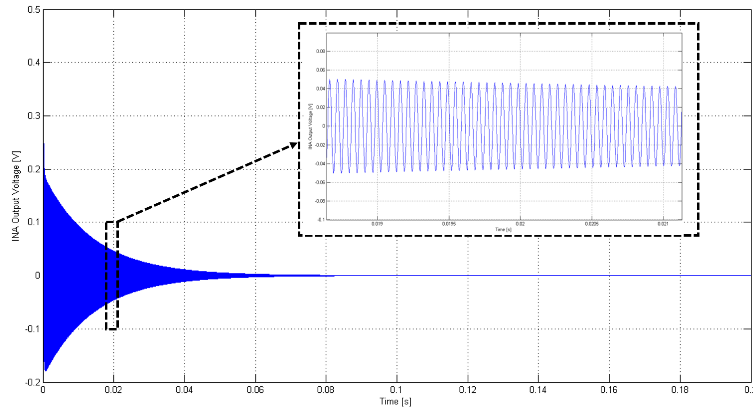

Figure 2.6: *Time response of system output in presence of mechanical offset. The rotor oscillates at the start-up, but once the equilibrium position has been reached, no offset signal is observed at the output.*

Provided to wait for the initial transient, if only this contribution is present, no offset signal is visible at the system output.

- *Real case*: unfortunately, in a real case, electrical and mechanical offset contributions are simultaneously present. Both capacitances and electrostatic forces are thus different:

$$C_1 = \frac{\epsilon_0 A}{g - \mathbf{x_{os}} - x(t)} \qquad C_2 = \frac{\epsilon_0 A}{g + \mathbf{x_{os}} + x(t)} \tag{2.27}$$

$$F_{el1} = \frac{\epsilon_0 A(V_{bias} - \mathbf{V_{rot}(t)})^2}{2(g - \mathbf{x_{os}} - \mathbf{x(t)})^2} \qquad F_{el2} = \frac{\epsilon_0 A(V_{bias} - \mathbf{V_{rot}(t)})^2}{2(g + \mathbf{x_{os}} - \mathbf{x(t)})^2} \tag{2.28}$$

Electrostatic forces are indeed DC unbalanced due to the presence of mechanical offset, with an AC component due to the presence of a residual rotor voltage $\mathrm{V_{rot}(t)}$. This causes a *sinusoidal displacement x(t)* to arise and persist also after the settling of the transient caused by the presence of $\mathrm{x_{os}}$.

- $C \cdot \frac{\partial V_{SR}}{\partial t}$ is not null. In this case it is also different for the two stators, being $\mathrm{C_1} \neq \mathrm{C_2}$ due to the presence of mechanical offset;
- $V_{SR} \cdot \frac{\partial C}{\partial t}$ is not null. Due to the rotor movement x(t) it is of opposite sign for the two stators, as when the rotor approaches stator one $\mathrm{C_1}$ increase while $\mathrm{C_2}$ decreases, and viceversa.

This leads the system offset to be a sinusoidal signal, with frequency equal to the one of the drive current ($\mathrm{f_d}$) and in phase with the rotor displacement. For a sample device with resonance frequency $\mathrm{f_0}$ of 20 kHz and Q of 1000, the simulated residual offset signal due to the simultaneous effect of a mechanical offset $\mathrm{x_{os}}$ of 50 nm and an electrical offset $\mathrm{V_{rot}}$ of 5 mV is shown in figure 2.7. Comparing it with figure 2.6 - where no offset was present once the equilibrium condition had been reached - in the inset is highlighted the residual sinusoidal voltage due to the presence of both offset sources at the same time, without any external magnetic field applied. This offset signal features an amplitude comparable with the one of the desired signal relative to an external magnetic field of about 1 mT.

2.3.1 Offset in multi-loop architectures

Because multi-loop architectures require a spiral path, they are intrinsically asymmetric. Looking at figure 2.2, if the resistance of the structural link connecting two springs is $\mathrm{R_{link}}$ and the resistance of a half spring is $\mathrm{R_P}$, much lower than $\mathrm{R_{link}}$ thanks to springs metalization, the simple resistive model of figure 2.8 is obtained.

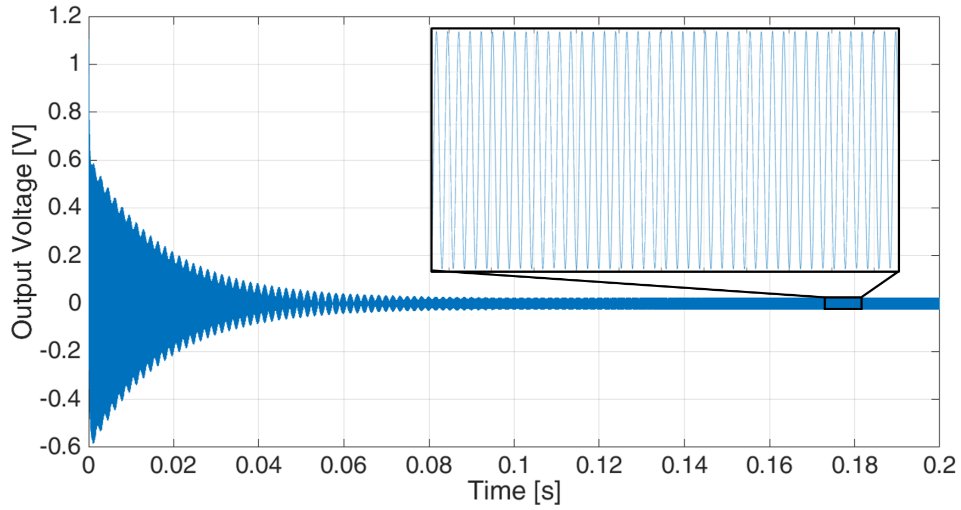

Figure 2.7: *Output offset voltage for a device with f_0 of 20 kHz, Q of 1000, a mechanical offset x_{os} of 50 nm and an electrical offset V_{rot} of 5mV. The peak voltage of the undesired signal is comparable to the one of an external magnetic field of about $1mT$.*

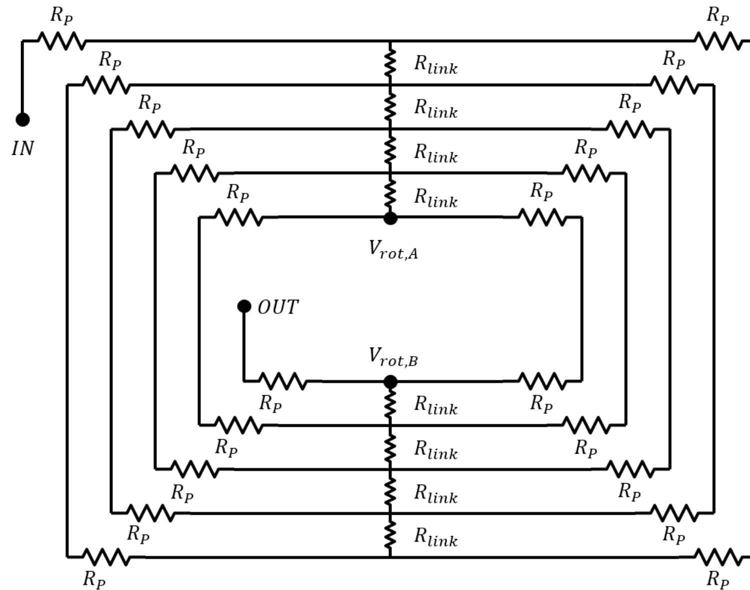

Figure 2.8: *Resistive model of the multi-loop structure of figure 2.2. R_P represents the resistance of a half spring, R_{link} represents the resistance of the structure links between the springs. R_P is a lot lower than R_{link} thanks to metalizations, which decrease springs resistances.*

The rotor is no more ideally at the same (null) voltage as in the simple case of section 2.3, but it has structure-dependent voltages ($V_{rot,A}$, $V_{rot,B}$), which are time-varying with the drive current. Being mechanical offset technology dependent, and electrical offset both technology and structure dependent, a sinusoidal offset signal is unavoidably present at the output of these structures.

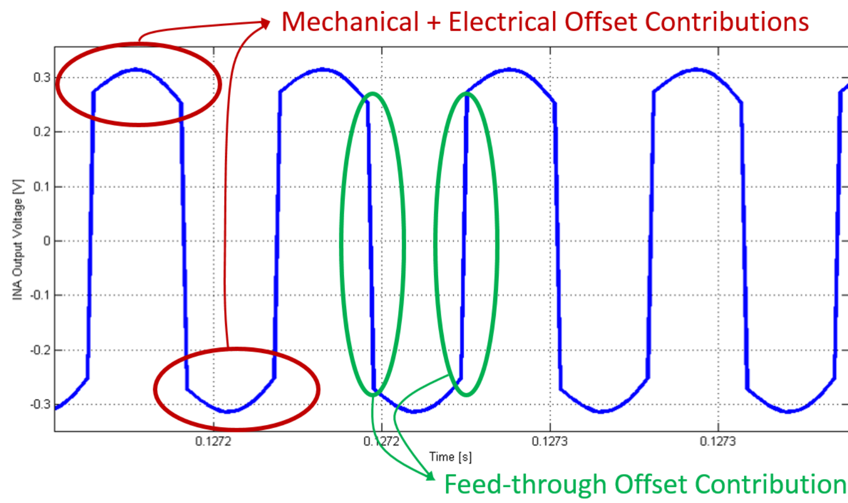

Figure 2.9: *Voltage waveform at the system output in absence of external magnetic field. While all the offset phenomena are visible, it is clear that the dominant one is the feed-through contribution.*

2.3.2 Feed-through offset contribution

A third offset contribution may be present. Being of the same shape of the drive signal, it is caused by a *direct coupling* between drive and sense signals. As visible in figure 2.9, where the device is driven through a square-wave current, this coupling effect turns out to be the dominant contribution. It is directly related to the layout of structures and electrical interconnections used to bring signals in and out from the package. Being a layout-dependent offset, it is not significantly drifting with environmental changes, as the coupling capacitances should be stable with temperature.

Neglecting the structure link resistances of figure 2.8, it is possible to obtain the model shown in figure 2.10, where this last offset contribution is modeled with two *feed-through* capacitances directly coupling drive path and sense electrodes.

All the simplifying assumption made through this section to explain different offset contributions are directly derived from a more accurate anal-

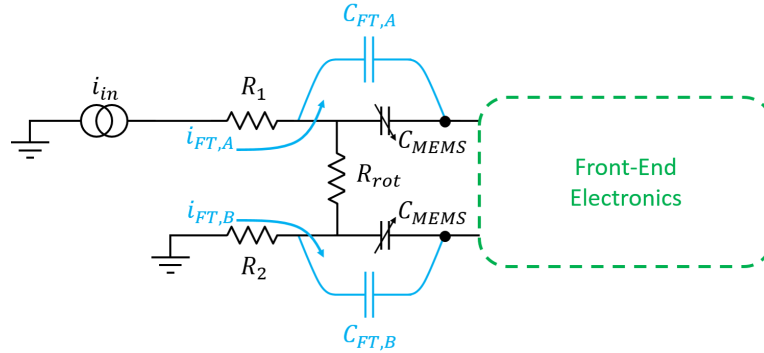

Figure 2.10: *Simplified resistive model for the multi-loop structure of figure 2.2 with the presence of feed-through capacitance to model the feed-through offset contribution. R_{rot} is the resistance between the two rotor ends, while R_1 and R_2 represent the equivalent resistances respectively between the input pad and the rotor and the output pad and the rotor.*

ysis of the offset phenomenon through a *Simulink* model, shown in figure 2.12, in which the three dominant offset contributions are put in evidence.

2.3.3 Offset compensation

Compensation of such offsets is needed at a rough level to avoid saturation, at a higher level to guarantee the possibility to fully exploit the whole electronic dynamic range, and at the highest level to compensate also possible offset drifts. Options for offset compensation in MEMS are in general split into two categories: electronic compensation and electro mechanical compensation. The former is usually based on the injection of a signal equal and opposite to the offset at a certain point in the electronic chain, before signal saturation [57]. The latter, instead, generally compensates for mechanical anomalies, as the Tatar quadrature-compensation scheme for gyroscopes [56].

The chosen offset compensation technique for this work is an electro mechanical one. The technique (a similar one was proposed in [58]) consists in the application of a small DC voltage difference to the two stators of the differential capacitive cell. This puts the rotor in a position such that the differences in the capacitive gains of the two stators compensate the differences in crosstalk between drive and sense electrodes. This avoids the addition of more electronics stages, which would increase the power consumption in view of an integrated implementation. Indeed, a trimming of

the DC bias applied to the stators would only be required during the calibration phase, which is however mandatory for any commercial product. Any change in total power consumption of the system would thus be required.

Figure 2.11 shows simulation results for a test structure respectively adding and subtracting a voltage ΔV to the two stators. In the first case (figure 2.11a) x_{os} and V_{rot} are varied, while in figure 2.11b offset compensation dependence on the feed-through capacitance is shown.

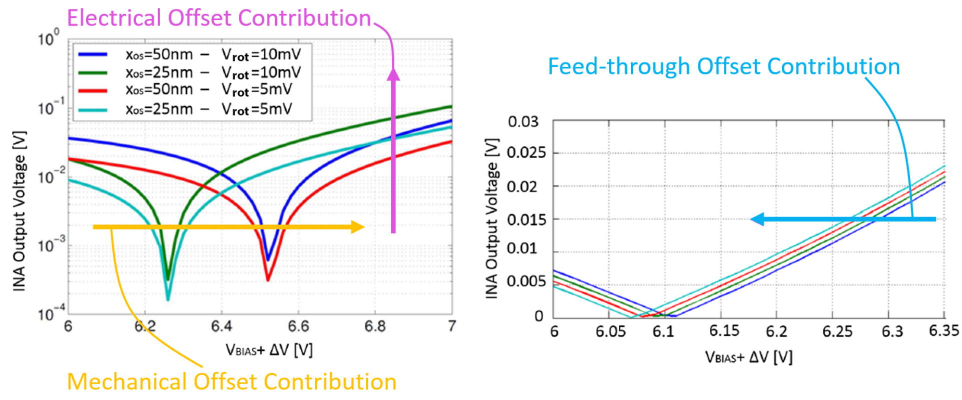

Figure 2.11: *Offset compensation unbalancing stator voltages of a quantity $\pm\Delta V$ with respect to the initial V_{bias} value of 6 V. Dependences of the ΔV_{opt} value on different offset contributions are shown.*

Dependence of the voltage needed to minimize offset (ΔV_{opt}) are then clear:

- *Mechanical Offset*: ΔV_{opt} increase with increasing values of x_{os};
- *Electrical Offset*: ΔV_{opt} is independent on the amplitude of the residual voltage on the rotor V_{rot};
- *Feed-through Offset*: ΔV_{opt} varies with the variation of the crosstalk between drive and sense electrodes. The direction of the variation depends on the relative intensity of the couplings for the two sense electrodes.

From simulations it is visible that a reduction of more than two orders of magnitude could be achieved with the right value of voltage unbalancing ΔV, and that the more precise is the voltage regulation, the lower becomes the offset.

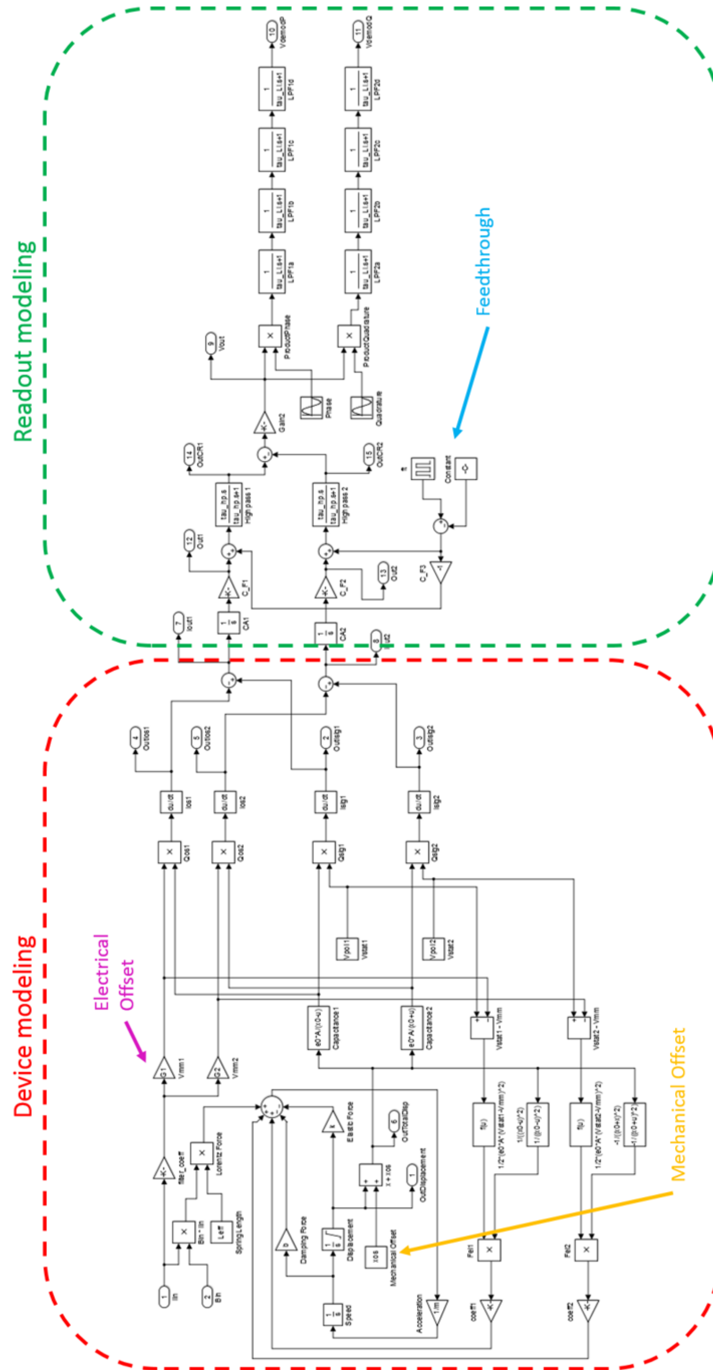

Figure 2.12: *Simulink model comprising device and readout behaviors together with all the offset phenomena.*

CHAPTER 3

A 3-axis MEMS magnetic field sensing system

3.1 Fabrication Process Challenges

All the devices designed to integrate the innovative elements described in chapter 2 are fabricated with the 22-μm-thick *ThELMA* technology by *ST Microelectronics*. *ThELMA - Thick Epitaxial Layer for Microactuators and Accelerometers* - is a surface micro-machining process similar to other industrial fabrication technologies, featuring deep reactive ion etching (DRIE) for structural parts definition, and hydrofluoric acid attack for device release. The process is currently used for mass production of accelerometers and gyroscopes. More informations about it can be found in [59] and [60].

In order to exploit current recirculation, it is compulsory to control the current path, which is not trivial in the used MEMS technology. Figure 3.1 shows that, without any additional layer, the current, flowing through polysilicon, would not follow the desired path. It would indeed choose the less resistive way to flow from the input to the output, which is not the spiral one, loosing all the benefit related to current recirculation. As the sensors,

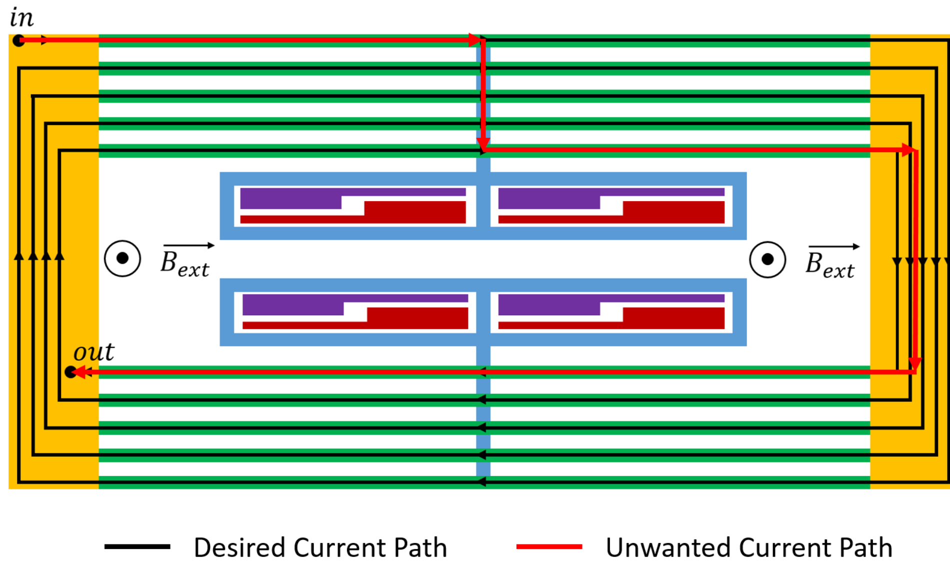

Figure 3.1: *Current paths on multi-loop Lorentz-Force magnetometer architecture. In black the desired spiral paths allowing the current recirculation with consequent force amplification; in red the less resistive path, that the current would follow without any additional layer to the poly-silicon one.*

in their final applications, require full compatibility with the industrial process, it is necessary to evaluate the options available on ThELMA process to create a controlled low-resistive path which can be followed by the driving current.

The only available option is to exploit the metal deposition step, already available for creation of pads and electrical interconnections. Following this guideline, two options were investigated: (i) the deposition of metal paths isolated from the structural layer through an insulating material (SiC) and (ii) the deposition of metal paths directly on the polysilicon layer. The former option has the obvious advantage of allowing an optimum definition of the current paths, completely decoupling the electrical domain from the mechanical one. However, it proved to be technologically challenging due to residual stresses on the different materials forming the stack. The second option was therefore selected. The challenge in the design of multiple loops within a standard industrial process is thus represented by the absence of an insulating layer between the metal forming the loops and the heavily doped polysilicon layer. This allows the current to more easily follow leaky paths which could be created by the direct contact between structural and metal layers. The effective current trajectory depends (i) on the resistivity

of the two materials, (ii) on the contact resistance between the two materials ($2.7\text{k}\Omega \cdot \mu\text{m}^2$), and (iii) on the structure geometry. The former is defined by the process: Aluminum square resistance is 0.04 $\Omega/\square$, PolySi square resistance is 20 $\Omega/\square$.

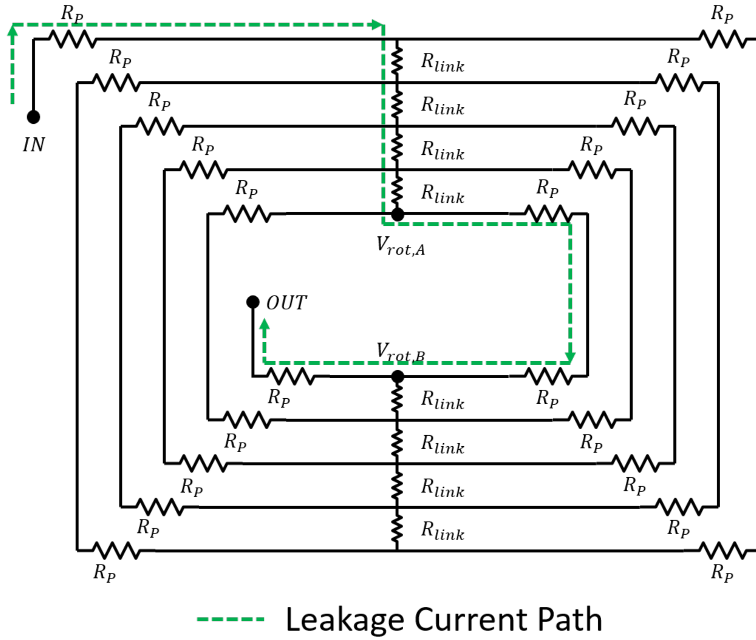

Figure 3.2: *Schematic representation of the resistive model of a generic multi-loop magnetometer. The desired current trajectory is a long spiral of low-resistivity Aluminum, which follows the R_p resistnaces. Lekage trajectories, as the one presented with a dashed line, arise from short paths of high-resistivity polysilicon (R_{link}). The contact resistance between the layers was estimated to be $2.7\ k\Omega \cdot \mu m^2$.*

Referring to the resistive model of figure 3.2, even if the Al square resistance is much lower, the aspect ratio of its path, due to the adopted recirculation loops, can be orders of magnitude longer than for parasitic paths through polysilicon. Along the desired spiral path there are contributions R_p given by the Al resistance; along parasitic paths there are contributions R_link given by the polysilicon resistance. These links between adjacent spiral loops are unavoidable to keep them rigidly connected, so to obtain a single mechanical resonant sensing mode, as will be shown in the following. As part of the current flows through these undesired leaky paths, lower amount of current will contribute to the Lorentz force generation, resulting in a reduction of sensitivity. This leads to the definition of an *effective loops*

number $N_{loop,eff}$, which is lower than the structural loop number N_{loop} and takes into account the current losses in the polysilicon parasitic path. Due to the fact that loops are nested one another, and more in general to the complexity of the geometry, the calculation of the coefficient $N_{loop,eff}$ will be carefully performed via finite element simulations.

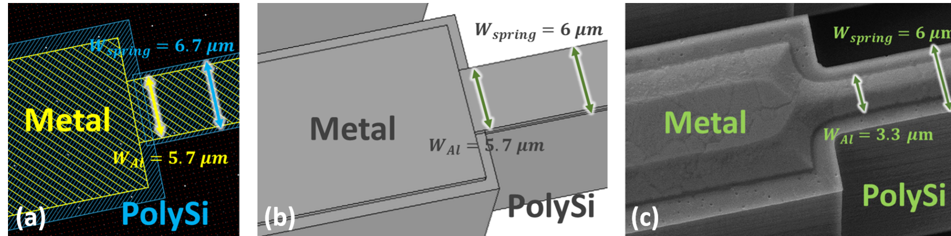

Figure 3.3: *Metal layer on structural poly-silicon: (a) layout for masks fabrication (b) 3D CAD expected result (c) real fabrication result. The etching on the structural layer is the expected one, while the width of the metal layer is 3.3μm instead of the expected 5.7μm.*

A further effect contributing to the reduction of the effective loops number is shown in figure 3.3, where the layout for masks definition is visible, together with the 3-D CAD expected result and the real fabrication result of the metal layer above the polysilicon one. Though the expected geometry had a rectangular section metal layer 5.7 µm wide and 600 nm thick, the obtained one is a roughly triangular section metal layer 3.3 µm wide and 500 nm thick. This excessive Aluminum etching both in width and thickness makes the metal path more resistive, increasing the amount of current flowing in the structural leaky paths. The effective loops number $N_{loop,eff}$, and thus the sensitivity, are consequently decreased with respect to theoretical values.

3.2 Device Design

3.2.1 Module at a glance

The module, sensitive to 3-axis magnetic field, is composed by four different structures:

- *One* device for the sensing of *out-of-plane* magnetic field;
- *Two* identical devices, rotated by 90°, for the sensing of *in-plane* field;
- *One resonator*, used as frequency-selector for the drive current.

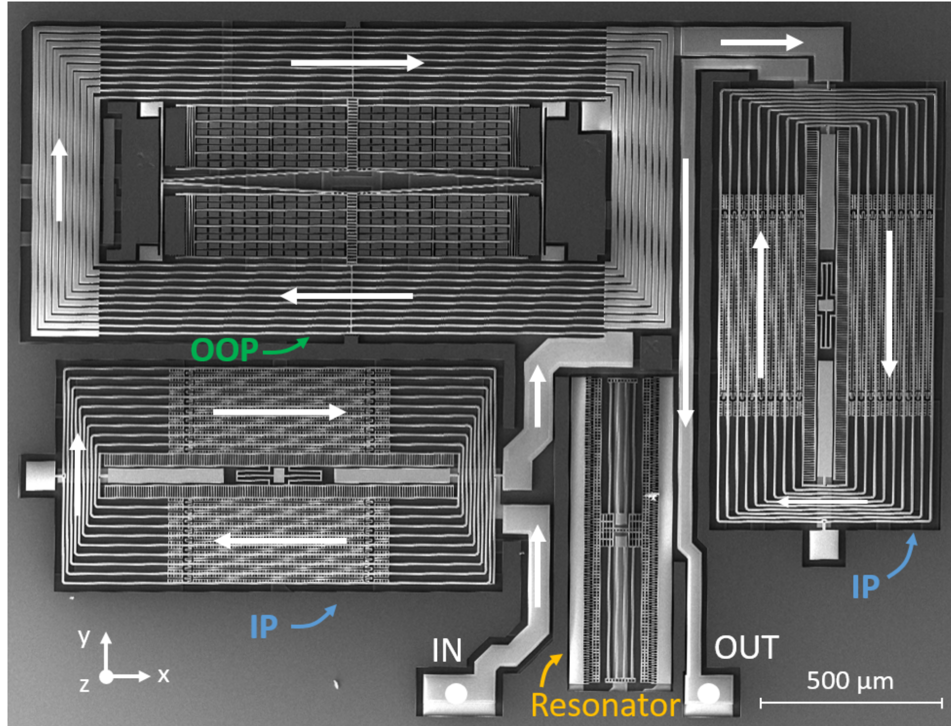

Figure 3.4: *SEM image of the complete 3-axis module, composed by one Out-Of-Plane (OOP) field sensitive device, two In-Plane (IP) field sensitive device and a Tang resonator to select the drive frequency. White arrows indicate the current path.*

In figure 3.4 a SEM image of the entire module is presented, with the whole current path highlighted. The drive current not only flows within each device itself, but also *from one device to another*. This feature is achievable thanks to off-resonance operation. In this case only one oscillator circuit is needed, and the total current contributing to the MEMS power consumption is the one flowing into the three devices. Referring to figure 3.5, in case of off-resonance operation a 3-fold saving in terms of drive circuit power dissipation - actuation current included - is guaranteed with respect to resonance operation. The full, ready-to-use module, including the design area, the sealing area and the pad area, can be sized to a single chip with square dimensions of about $4\mathrm{mm}^2$.

Even if it is not necessary to reach the same precision as in the hypothesis of resonance operation, also for off-resonance operation a good match of the mismatch $\Delta\mathrm{f}$ is required, and thus a good control of the relative distance between the drive frequency $\mathrm{f_d}$ and the sense frequency $\mathrm{f_0}$. Referring e.g. to equations 2.7 and 2.8, in the hypothesis of a device with the in-

dicated parameters, a mismatch variation of $\pm$ 5 Hz induces a sensitivity variation of 1.6%, that is better than the 29.3% which would be obtained with resonance operation, but is still not negligible. All devices have hence to be equipped with tuning electrodes, in order to give the possibility to shift their resonance frequency f_0 to the desired value. The module will then operate with all the devices frequencies set at $f_X, f_Y, f_Z = f_0$, and the drive frequency f_d at a mismatch Δf from f_0.

All the shown finite element simulations (FEM) of this work are performed using the full 3-D geometries in *Comsol Multiphisics*, with at least five elements within the smallest dimension of every structural part.

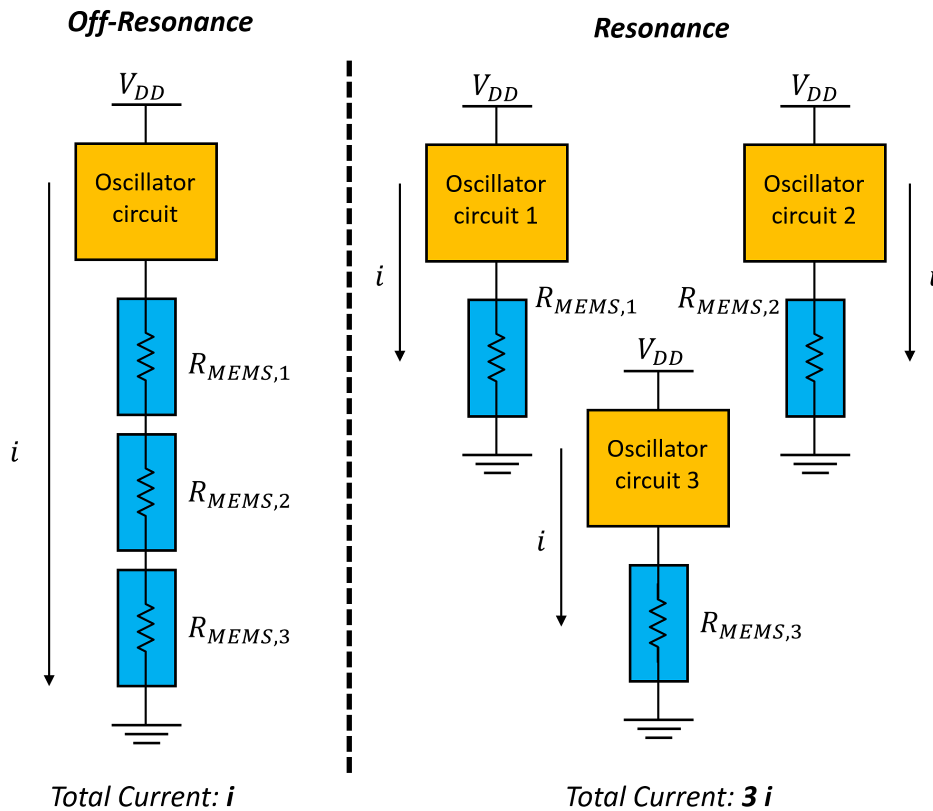

Figure 3.5: *Power consumption comparison between off-resonance and resonance operation. In off-resonance operation the same current can be exploited to drive all three sensors, leading to a power consumption saving of a factor three.*

3.2.2 Project criteria

All the design choices presented in the following, concerning both single-axis devices and the Tang resonator, have been made to comply with the following criteria:

- *Resonance Frequency*: the target resonance frequency has to be at the upper limit of the audio band ($\approx$ 20 kHz), in order to avoid audio disturbances and to obtain the lowest stiffness possible, increasing the Lorentz-induced displacement;
- *Overall size*: all the structures and their connections have to fit within a $2.5 \times 2\ \mathrm{mm}^2$ active area;
- *Loops number*: there is no trade-offs for the loops number but the one with the device dimension. The bigger the loops number, the higher the displacement, but the bigger is also the area occupation. The choice for all the device has then been of 10 loops each;
- It is not possible ato fit more than one metal loop onto a single polysilicon spring, because of the absence of an insulator between the two layers.

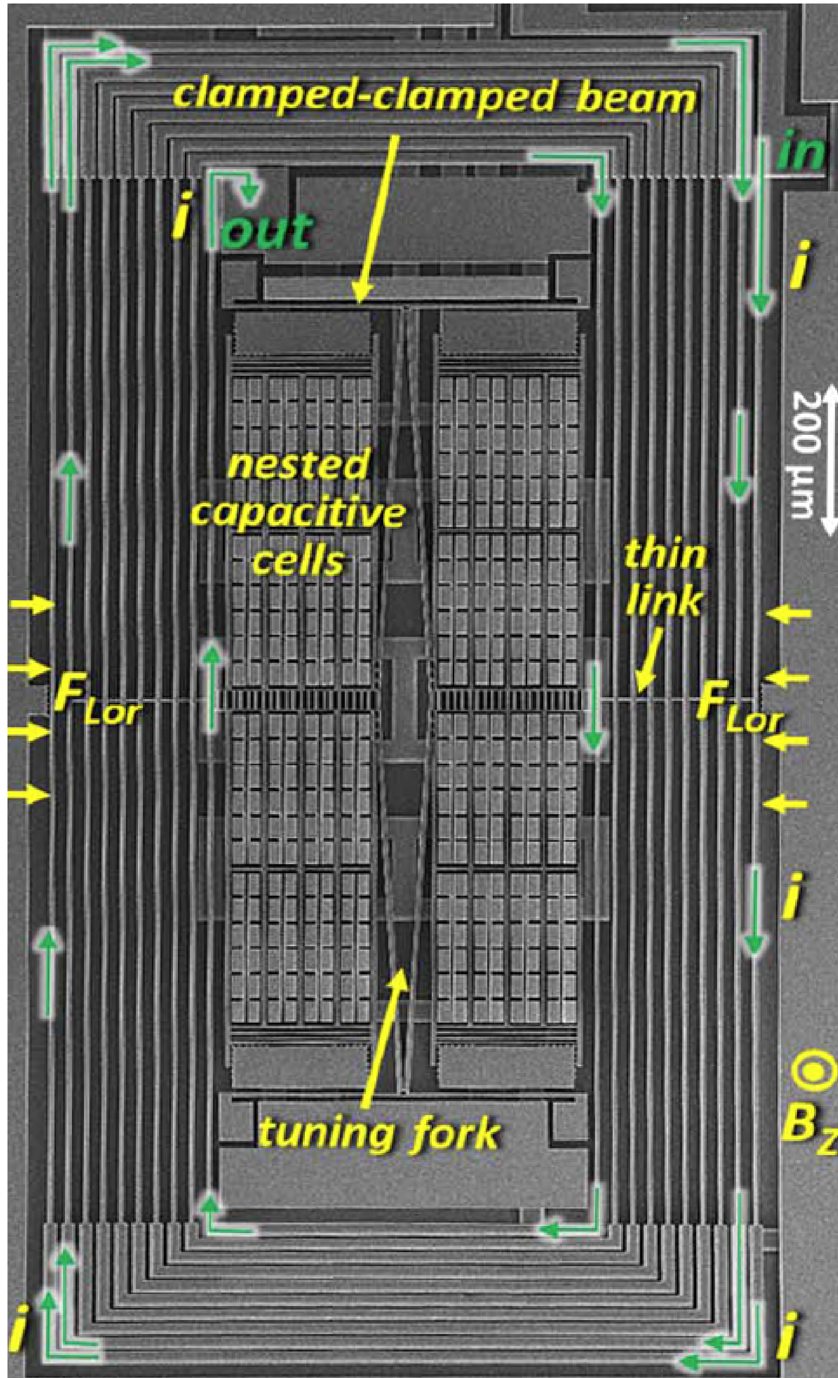

Figure 3.6: *SEM image showing the top view of the magnetometer sensible to the out-of-plane magnetic field. Current inlet and outlet, together with its spiral path and the arising Lorentz forces are put in evidence.*

3.2.3 Out-Of-Plane magnetic field sensing device

The device sensitive to the out-of-plane magnetic field, following the right hand rule, performs a translational planar movement. Its structure is shown in figure 3.6, where also its working principle is put in evidence. Its mechanical part is made of two springs, each formed by ten beams of length L of 1400 µm, holding a suspended frame (rotor). The beams of each spring are rigidly connected one another through thin links at their center. The frame suspends a battery of nested cells for in-plane capacitive motion sensing. A diamond-shaped tuning fork, first presented in [61], is suspended at its end by 410-µm-long clamped-clamped beams, connecting the two halves. Looking at the electrical domain, all along the 20 beams, a 30-mm-long Al path is deposited in order to create the 10-loops current recirculation spiral. As visible in figure 3.3 each beam has a width of 6 µm, covered by a 3.3-µm-wide Aluminum strip, leading to a total resistance of the current path of 480Ω. According to section 3.1, the smaller than expected width for the metal paths generates a non-negligible leakage current through the straight links connecting the beams. Their overall resistance along the most critical parasitic path turns out to be in the order of 1.5 kΩ: this lowers the improvement in sensitivity and resolution.

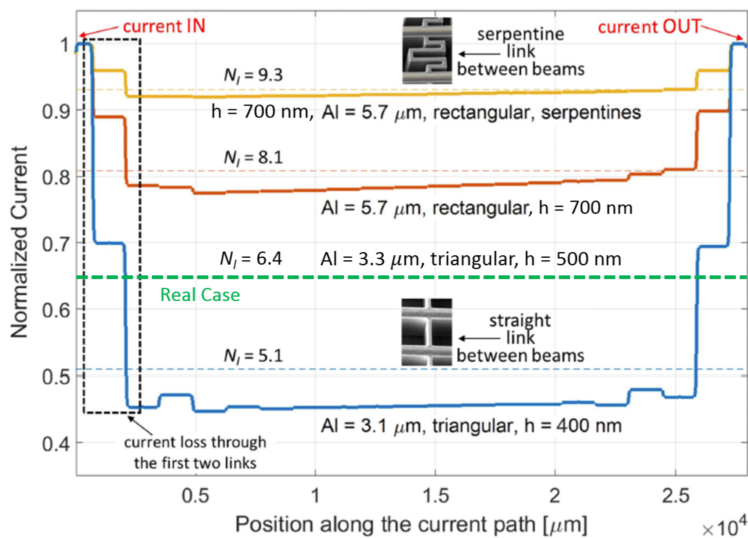

Figure 3.7: *Simulation for the Lorentz current flowing through the device. The curves refer to different metal widths and cross-sections or to different link geometries. The partial current loss in the first loop decreases if the resistance of the Al path is decreased (wide metal), or when the links resistance increases (serpentines).*

As shown in figure 3.7, this brings the effective number of loops to be $N_{loop,eff} = 5.1$ instead of the ideal $N_{loop} = 10$. It is worth notuce that there is not a trade-off for the loop number increase in the structure design but the area occupation, which is the reason why the presented structure features 10 recirculation loops. They become $N_{loop,eff} = 6.4$ with triangular metal layer 3.3μm wide and 500 nm thick. If the metal layer were fabricated as it was drawn by layout, the loss in equivalent number of loops would have been lower, featuring $N_{loop,eff}$ =8.1. Moreover, if a non-straight link were used - as the serpentine one shown in the inset and exploited in the in-plane device - a further improvement would be obtained, leading to an almost ideal situation, with only a 7% current loss.

One option to improve $N_{loop,eff}$ could be to place the sensing cells in between the springs, in order to increase the length of the thin links. This would reduce the current loss, but the sensing cells would always be at different voltages, due to the absence of the insulating layer between metal and polysilicon, making this strategy not pursuable.

Looking at figure 3.6, in operation, the AC current flows through the two springs in opposite directions, so that an out-of-plane component of magnetic field gives rise to in-plane, opposite Lorentz forces F_{Lor}. The presence of the tuning-fork determines the existence of both an in-phase and an anti-phase in-plane translational modes. The opposite direction of the Lorentz current excites the anti-phase mode, whose shape is indicated in the eigen-frequency FEM simulation of figure 3.8a: the readout of its movement gives information about the external magnetic field.

On the contrary, an external acceleration causes concordant forces for the two sub-frames, as shown in the in-phase mode FEM simulation of figure 3.8b. In this way, the action generated by the magnetic field results in a differential signal, while external accelerations are ideally rejected as a common mode and, to first order, do not provide any differential capacitance variation. This approach is to be pursued because the Lorentz force, as stated in section 1.3.1, can be orders of magnitude smaller than inertial forces. Moreover, the particular tuning-fork shape allows to push the in-phase mode at a frequency nearly doubled with respect to the anti-phase mode one.

Indeed - as visible in the insets of figure 3.8 and in figure 3.9 - while the anti-phase motion excites the first mode of the holding bars, the in-phase motion of the sub-frames excites their second mode, shifting upward the corresponding mode of the whole structure. This makes the device more tolerant to higher order effects induced by the presence of accelerations and vibrations. Further experimental details on the tolerance to accelerations

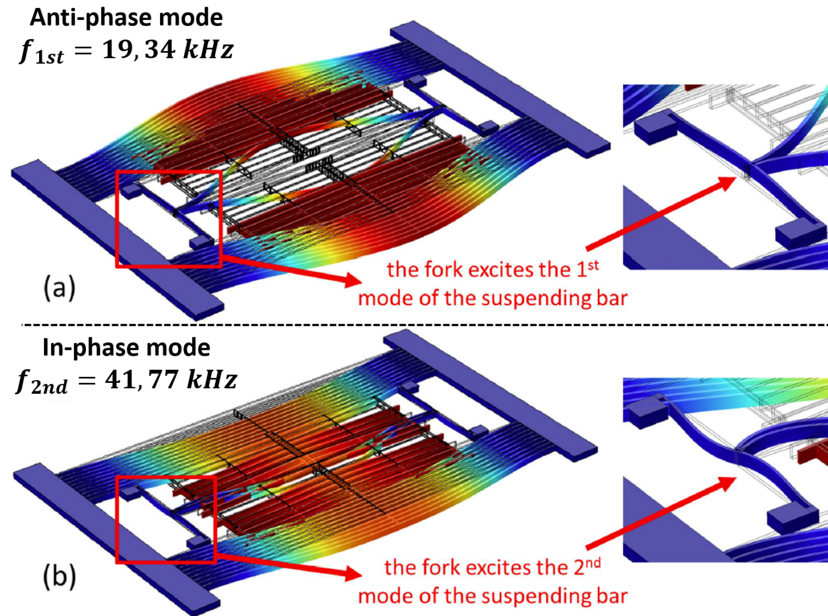

Figure 3.8: *Results of FEM simulations for (a) the anti-phase mode, excited by the Lorentz current flowing in opposite directions through the springs, and for (b) the in-phase mode, excited by external accelerations. The insets show how the tuning-fork geometry, coupled to the holding bars, helps in shifting the in-phase mode to frequencies higher than for the anti-phase mode.*

are shown in section 4.2.6.

The nominal frequency of the anti-phase mode is $f_Z = f_0 = 18.3$ kHz in operation, including the softening caused by electrodes biasing. Like in gyroscopes, this value is at the margin of the typical acoustic disturbance bandwidth [62], which generally ends around 20 kHz. This anti-phase displacement is readout through a special geometry of sensing electrodes, connected as in figure 3.10 in order to sense the differential motion of the device with the stators that see the rotor approaching to them all connected to the same front-end stage, and the other half of the stators all connected to another front-end stage.

Each fixed stator features interspersed apertures that act as escape paths for squeezed gas [52], thus reducing, with respect to a classical parallel-plates scheme, the damping coefficient and in turn the thermomechanical noise. According to electrical FEM simulations and to Montecarlo test particle damping simulations [63], this approach guarantees about the same capacitance variation per unit displacement and 45% lower damping with

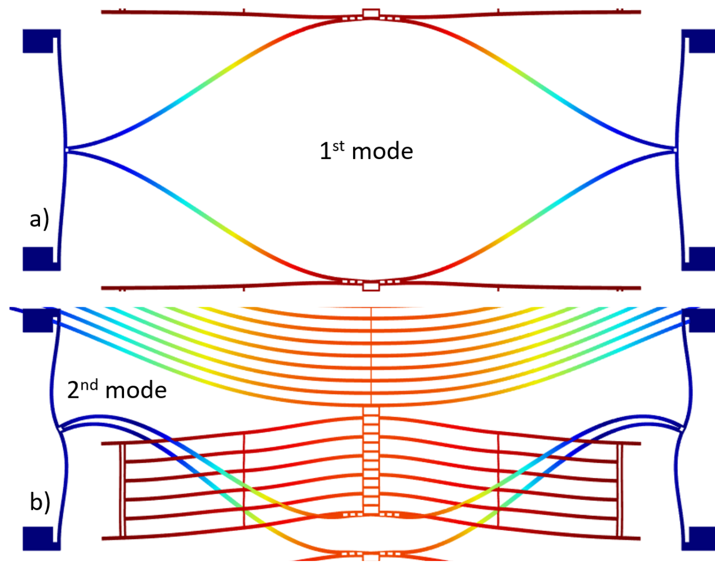

Figure 3.9: *Schematic representation of the effect of the tuning fork holding bars on the structure vibrational modes.*

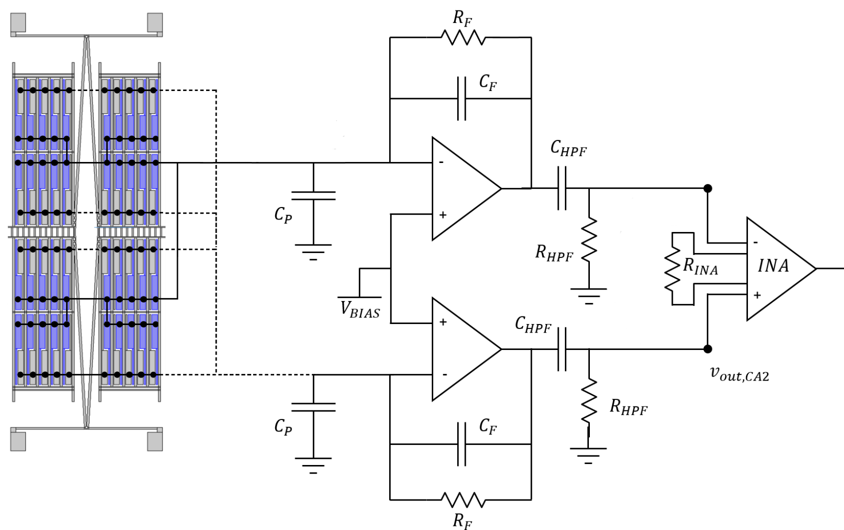

Figure 3.10: *Connection scheme of the electrodes for the sensing of the structure motion.*

respect to continuous stators [64]. The penalty of this solution is the larger area occupied by each differential stator (the number of sensing cells fitting in the same overall area is roughly 85% lower). Details of these electrodes (holed stators), whose optimization was itself part of this thesis, are visible

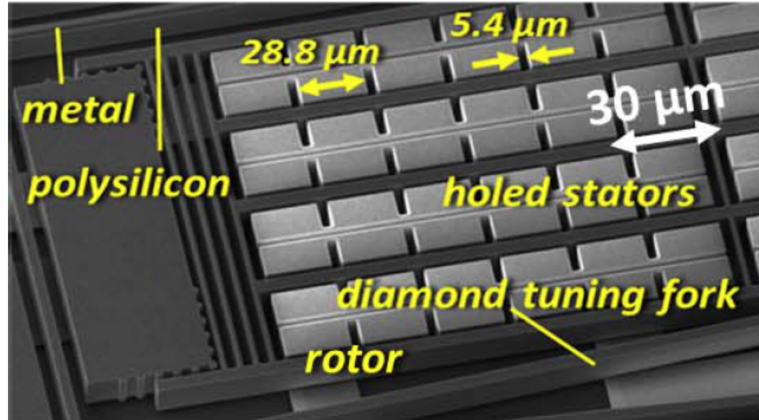

Figure 3.11: *Holed stators sensing architecture, featuring interspersed escape paths for squeeze-film damping reduction.*

in figure 3.11: a 5.4 μm aperture is provided every 28.8 μm of plate length. The former dimension is sized to be well larger than the gap, while the latter dimension is sized to be comparable to the structural thickness. The nominal gap between the rotor and the stators is 2.1 μm. The overall device area, including the anchor points, is 1600 μm×850 μm, while in Table 3.1 the most relevant parameters of the structure are listed.

Parameter	Unit	Value
Area	μm^2	1600 x 850
Effective stiffness	N/m	59
Quality factor	-	790
Single-ended rest capacitance	fF	445
Average Lorentz length	μ m	1400
Natural (untuned) frequency (B_Z mode) (f_0)	kHz	19.34
Natural (untuned) frequency (a_y mode) ($f_{0,2}$)	kHz	41.77

Table 3.1: *Most relevant parameters for OOP device.*

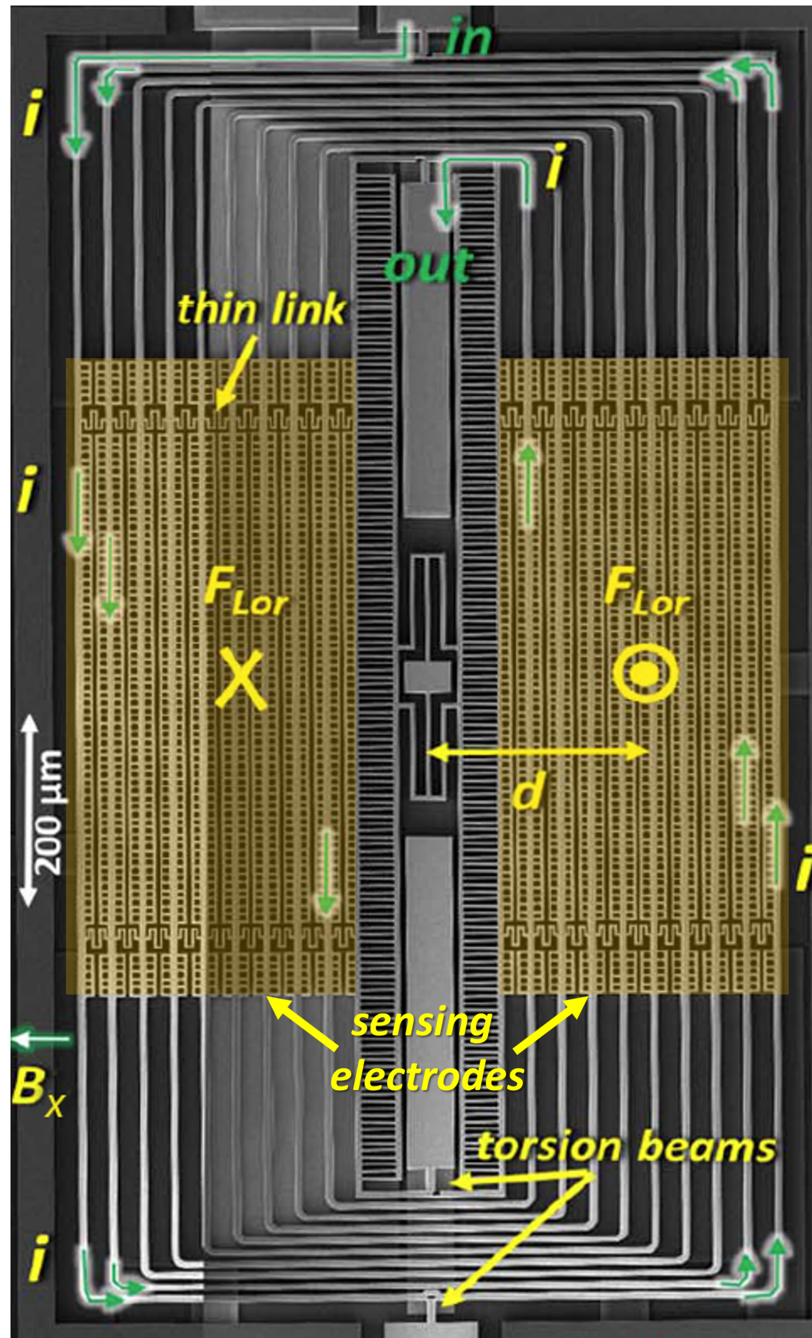

Figure 3.12: *SEM image showing the top view of the magnetometer sensible to the in-plane magnetic field along X direction. The structure for the sensing of the Y field is identical but rotated by 90°. Current inlet and outlet, together with its spiral path and the arising Lorentz forces are put in evidence.*

3.2.4 In-Plane magnetic field sensing device

The device to sense an in-plane field along the X-direction is shown in figure 3.12 (the device to sense the IP field along the Y-direction is a replica, rotated in plane by 90°). In presence of a magnetic field in the sensible direction, as schematically shown in figure 3.13, the structure performs a torsional movement. The information about external magnetic field is read in a differential way by means of a couple of electrodes placed beneath the structure, visible in figure 3.13b and c.

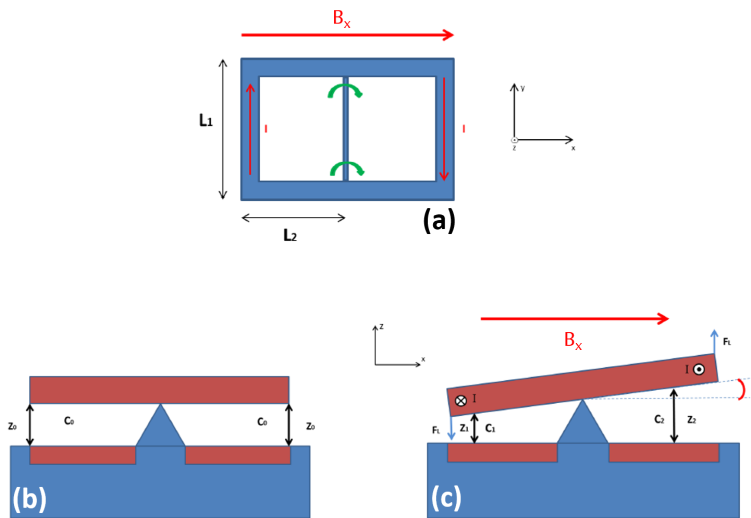

Figure 3.13: *Schematic working principle of the in-plane field sensing structure. It is a torsional structure, shown (b) at rest, and (c) under the effect of an external magnetic field in x direction.*

The real device (figure 3.12) is formed by four torsional beams, suspending a frame constituted by a 10-loop spiral, where individual loops are connected one another via two couples of thin links, to form the unique rigid frame. Maximization of the electrical resistance $\mathrm{R_{link}}$ in between parallel, adjacent paths of the spiral is achieved by using serpentine links instead of direct links. This turns into a 4-fold larger resistance value along each link with respect to a direct connection, and thus minimizes leakage of Lorentz current between adjacent loops. The structural frame is also anchored at the center, and nominally balanced along the rotation axis, so to minimize effects of accelerations along the sensing mode. On top of the frame, the Aluminum layer is deposited so to define - though the thin links - the effectively desired spiral trajectory of the Lorentz current. Suspending torsional beams have a width of 6.3 μm and a length of 21.7 μm.

In operation, an AC current is made flow through the device from the anchor point labeled 'in' in figure 3.12. The current follows the 27-mm-long spiral path (as indicated by i and the arrows for the first two loops and for the final one) and exits from the anchor point labeled 'out'. In presence of a magnetic field B_x along the X-direction, a pair of Lorentz forces will act, on average, as schematically indicated in the figure, determining a differential, out-of-plane, torsional motion. This is shown by the finite element method (FEM) simulation of figure 3.14.

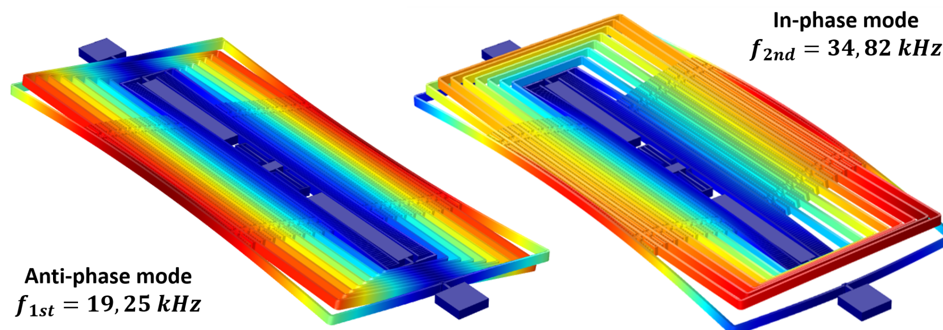

Figure 3.14: *Results of FEM simulations for (a) the anti-phase mode, excited by the Lorentz current flowing in opposite directions through the springs, and for (b) the in-phase mode, excited by external accelerations*

Such a current recirculation directly generates a 9.5× improvement in sensitivity and resolution. According to SEM measurements, the width of the spiral polysilicon path is 6 µm (as expected by design, accounting for nominal polysilicon over-etch predictions), while the width of deposited Al strips, as already mentioned in section 3.1, is 3.3 µm. Out-of-plane motion is detected via capacitance variation between the frame (which forms the top electrode) and two planar differential electrodes designed beneath the structure. The nominal vertical gap at rest between the rotor and the underneath planar electrodes is 1.8 µm. In the area corresponding to these bottom electrodes, the frame geometry is defined to increase the rest capacitance and the capacitance variation per unit displacement: figure 3.15 is a detail that shows how this is accomplished by adding rectangular blocks. The blocks are suitably holed not to impair the damping coefficient (and in turn thermomechanical noise) via extra squeezed-film damping.

Using SEM measured dimensions, the overall resistance of the 27-mm-long Al path is estimated to be 350 Ω, while the resistance along the shortest leaky path is about 5.5 kΩ. The device is designed to have the torsional

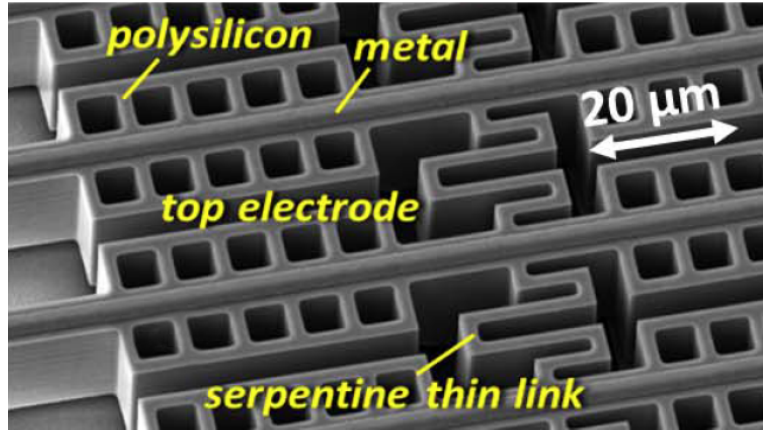

Figure 3.15: *IP magnetic field sensing structure detail, showing the serpentine links connecting the spiral loops and the top-electrode frame right above one bottom electrode*

mode (the first mode, to sense the Lorentz force as described above) at about $f_x = f_0 = 18.3$ kHz, already including effects of electrostatic softening in operation. The mode sensitive to Z-axis accelerations and vibrations, as well as all other high-order modes, us pushed up at frequencies larger than 32 kHz, thanks to the system of springs designed and anchored at the device center. In this way, immunity to mechanical vibrations induced by e.g. acoustic speakers is maximized even if the sensing frequency f_0 is not strictly above the audio range. The overall device area, including the anchor points, is 1300 μm$\times$640 μm, while in Table 3.2 the most relevant parameters of the structure are listed.

Parameter	Unit	Value
Area	μm^2	1300 x 640
Effective stiffness	N/m	83.3
Quality factor	-	1060
Single-ended rest capacitance	fF	487
Average Lorentz length	μm	1100
Natural (untuned) frequency (B_x mode) (f_0)	kHz	19.25
Natural (untuned) frequency (a_z mode) ($f_{0,2}$)	kHz	34.82

Table 3.2: *Most relevant parameters for IP device.*

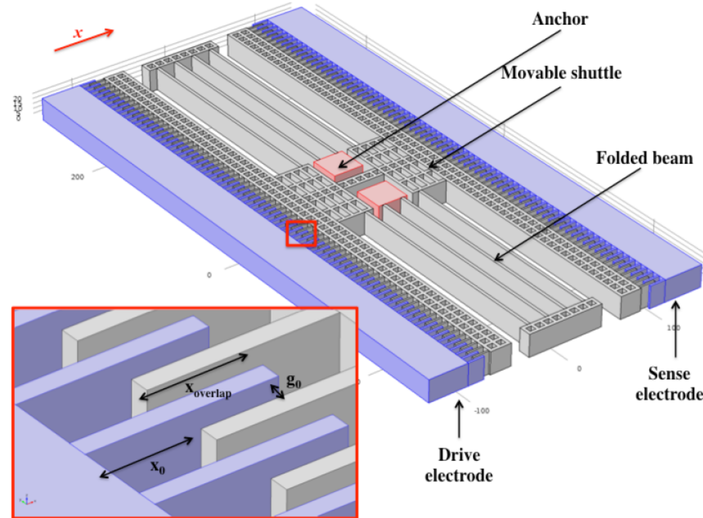

Figure 3.16: *3-D CAD geometry of the Tang resonator. A detail of drive and sense comb-fingers is shown in the inset.*

3.2.5 Tang Resonator

The same module also features a Tang resonator [65], which is used to generate the single reference frequency for simultaneous off-resonance operation of the three magnetometers, and whose geometry is shown in figure 3.16. The resonator structure is implemented as a 3-port configuration (see the top view of the device in the SEM image of figure 3.17), with motion actuation and detection based on symmetric comb-driven ports, each featuring 113 fingers with a nominal 8 µm overlap length and a nominal 2.1 µm gap.

The resonance frequency of the first mode (in-plane translational mode, shown on figure 3.18 is designed at $f_R = f_d = 18.1$ kHz, in order to operate with a $\Delta f = (f_0 - f_d) = 200$ Hz nominal mismatch with respect to the resonance frequency of the biased magnetometers.

Suspending springs are designed through four 2-fold beams of identical length (details can be seen in 3.19): such first expedient, as described in [66], has the purpose to guarantee that frequency changes under temperature variations are only due to Young's modulus changes rather than to temperature induced stress effects. Further, these beams are designed exactly with the same width as for the beams of the three magnetometers, so that local effects of under or over-etching affect the frequencies of the resonator and of the magnetometers in the same way. This second expedi-

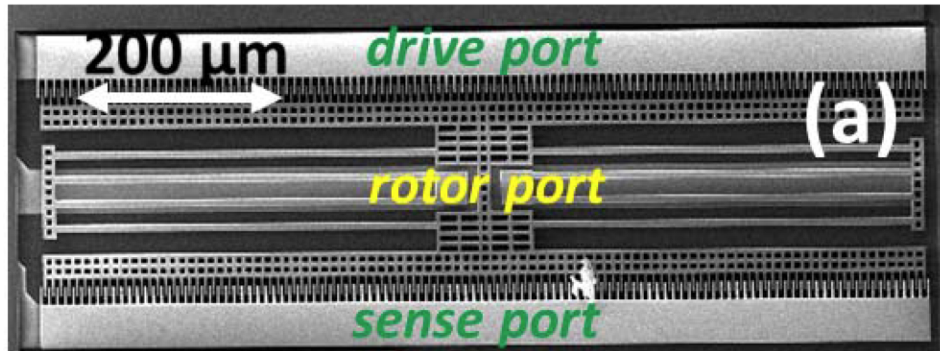

Figure 3.17: *SEM image showing the top view of the Tang resonator, used as closing element for the oscillator loop, responsible for the drive frequency selection.*

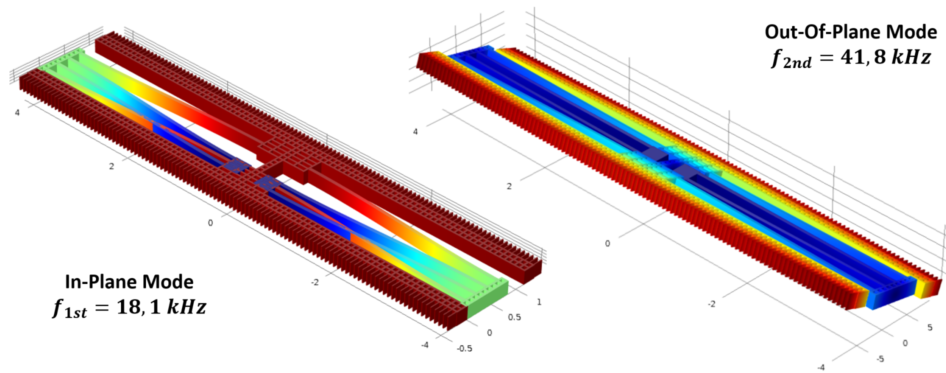

Figure 3.18: *Results of FEM simulations for (a) the in-plane desired mode, used to select the drive frequency within the oscillator circuit (b) the out-of-plane mode, at a frequency more than double with respect to the first mode one.*

ent should ensure a constancy of the frequency difference from part to part. The overall area taken up by the resonator is 290 µm×840 µm.

3.3 Drive and sense electronics

3.3.1 Electronics overview

Thanks to off-resonance operation, the three magnetometers can share the same driving current. They are also read out by the same front-end electronics topology, as the signal to be processed is a current flowing out the stators for all the devices.

The discrete-components characterization PCB, schematically shown in figure 3.20 would then be composed by one driving and three identical

Figure 3.19: *Detail of temperature-induced stress effects tolerant springs and comb-fingers for driving and sensing of the Tang resonator.*

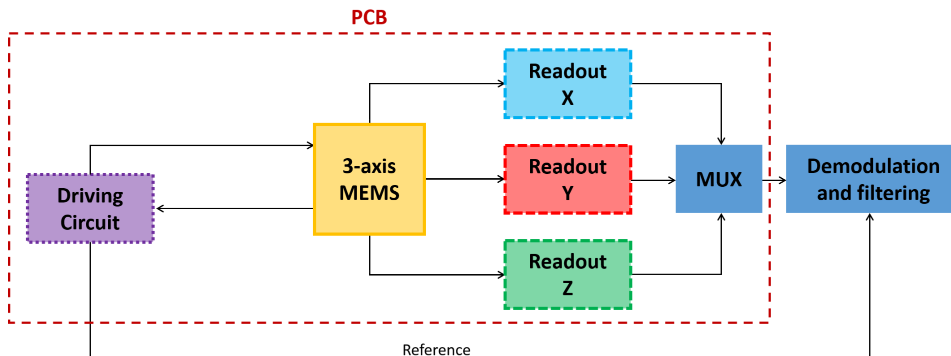

Figure 3.20: *Diagram representing the functional blocks of the whole characterization PCB for a 3-axis MEMS Lorentz-Force based magnetometer with capacitive readout.*

sensing blocks. The possibility to identically replicate the same circuit is only guaranteed by the non-trivial achievement of obtaining well-matched sensitivities for all the devices, along the different sensing axes. This also enables the possibility for the output signals of the three front-end circuits to be sequentially directed, through a multiplexer driven by suitable digital logic, to a single gain, demodulation and filtering chain, implemented using lock-in (LIA) techniques. Multiplexing can occur at a frequency up to 300 Hz, compatible with a system output data rate of 100 Hz per channel, and thus - according to the sampling theorem - with a maximum theoretical bandwidth of 50 Hz for the entire system. This bandwidth value is set by a tunable low-pass filter after the demodulation stage.

3.3.2 Sense electronics

Front-end stage

The front-end stage for the device readout needs to convert the current flowing out from the stators to a voltage signal to be processed.

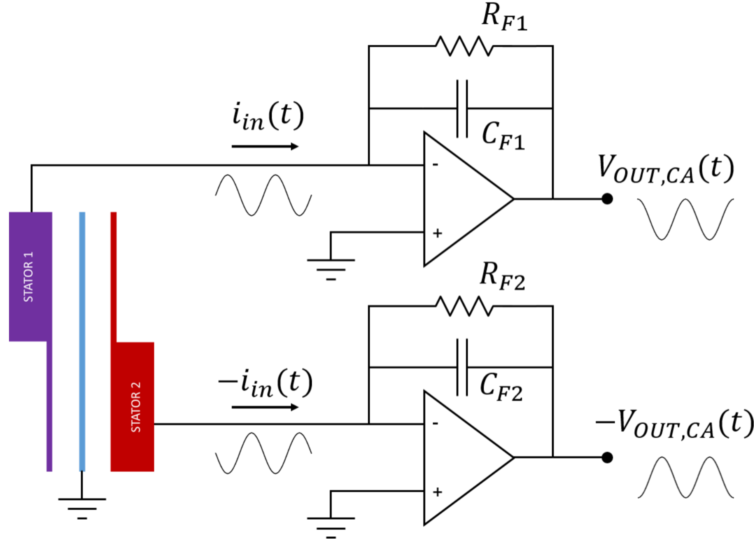

Figure 3.21: *Front-end stage for the conversion in a voltage signal of the current flowing out the MEMS stators.*

The chosen configuration, also described in [46] and [67], is the one shown in figure 3.21, where one stage is connected to the corresponding stator of the differential parallel-plate cell through its virtual ground. The half of the device stators seeing the rotor approaching at a given time instant is all connected together, as well as the other half which in the same instant sees the rotor going away. In this way the amount of charge flowing into the two front-end stages is doubled with respect to the single-ended configuration. The two pairs of stators are biased through the virtual ground by a constant voltage V_{bias} applied to the positive input of the operational amplifiers. The same circuit topology could be used both as a trans-impedance amplifier (TIA) and a charge-amplifier (CA) configuration, depending on the pole frequency:

$$|T(s)| = \left|\frac{V_{out}(s)}{I_{in}(s)}\right| = \frac{R_F}{1 + sC_F R_F} \qquad f_p = \frac{1}{2\pi C_F R_F} \tag{3.1}$$

Noise analyses [68] show that working with a charge-amplifier configu-

ration, which means dimensioning the pole frequency well before the system operating frequency, shows better performance in terms of noise while the signal behavior is not altered. This gives more freedom in the feedback component choice: the capacitance has to be the lowest possible, as it is responsible for the signal gain ($1/\mathrm{sC_F}$). Looking at equation 2.26, the resistance has instead to be high enough to make its noise contribution negligible and to push the pole at a low enough frequency. Indeed the operation frequency of $\approx$ 20 kHz of the system puts a constraint on the pole frequency, which has to be at least lower than 2 kHz. This led to the choice of a feedback capacitance $\mathrm{C_F}$ of 0.5pF and a feedback resistance $\mathrm{R_F}$ of 600MΩ. Such a high resistance value, in the perspective of an integrate implementation, could be reached by means of transistors in off-state. Indeed it is not needed a precise resistance value, being the feedback dominated by the capacitance from a certain resistance value on. A very low-noise operational amplifier has also been chosen: AD8065 from Analog Devices [69], which features an equivalent input voltage noise of $7\frac{\mathrm{nV}}{\sqrt{\mathrm{Hz}}}$ and an equivalent input current noise of $0.6\frac{\mathrm{fA}}{\sqrt{\mathrm{Hz}}}$.

A sinusoidal MEMS capacitance variation directly induces a current into the charge amplifier virtual ground:

$$I_{in}(t) = V_{bias} \cdot \frac{\partial C}{\partial t} + \cancel{C \cdot \frac{dV_{bias}}{dt}} = V_{bias} \cdot \partial C \cdot \omega \cdot sin(\omega t) \tag{3.2}$$

leading to a transfer function between capacitance variation and output voltage:

$$V_{out} = V_{bias}\, \partial C\, \omega\, sin(\omega t) \cdot \frac{1}{j\omega C_F} \quad \rightarrow \quad \frac{\partial V_{out}}{\partial C} = \frac{V_{bias}}{C_F} \tag{3.3}$$

The voltage at each CA output is thus a signal at the same frequency of the rotor displacement (thus of the drive current) with an amplitude which is directly proportional to the capacitance variation. Referring to equation 2.14 it turns out to be also proportional to the external magnetic field. The only difference between the signals at the two charge amplifier outputs is the phase: as one stator sees the rotor approaching while the other sees it going away, a phase shift of π is present between the two signals.

Amplifier stage

These two signals are then high-pass filtered - in order to remove any undesired DC component, e.g. generated by offsets in the op-amp, which has

no meaning in terms of magnetic field - and sent to the differential inputs of an instrumentation amplifier (INA 129 from Texas Instruments [70]), as visible in figure 3.22.

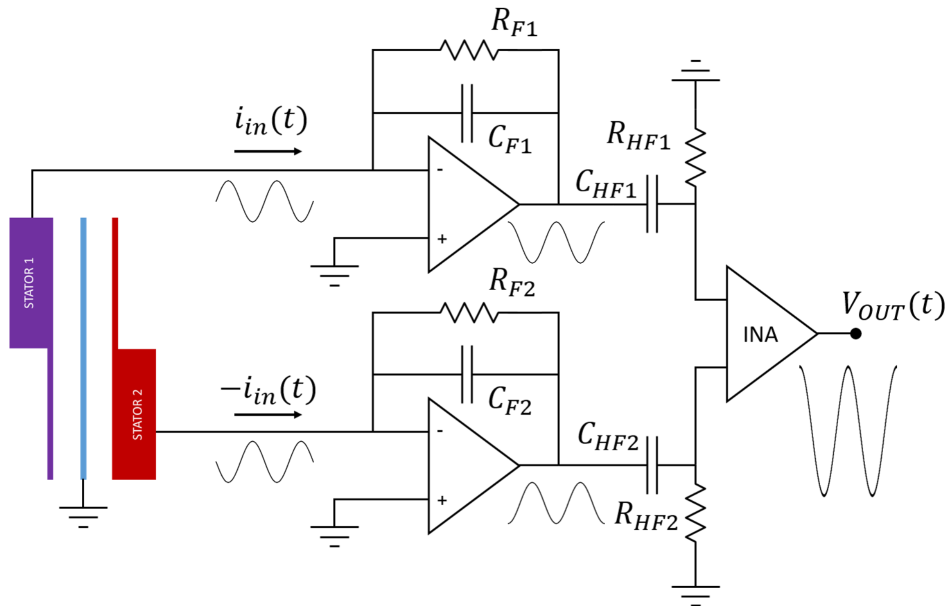

Figure 3.22: *Complete uni-axial readout chain with an high-pass filtering stage at each charge amplifier output and an INA stage to amplify the signals difference.*

As the two inputs are sinusoidal signals with a phase shift of π, the output signal will be again a sinusoidal signal at the drive frequency, whose amplitude is amplified according to the chosen gain $\mathrm{G_{INA}} = 1 + 49.4\mathrm{k}\Omega/\mathrm{R_G}$. With an $\mathrm{R_G}$ of $2.54\mathrm{k}\Omega$, the selected gain of the amplifier stage is $\mathrm{G_{INA}}$ = 20.45.

3.3.3 Drive electronics

The driving electronics is composed by two blocks: (i) the oscillator circuit to select the frequency of the drive current and (ii) the current generator.

Oscillator Circuit

The resonant element of the oscillator circuit is the Tang resonator shown in section 3.2.5. It is well known [65], [60], [66] that a MEMS resonator can be modeled with an RLC series network, where each electrical parameter is directly related to a mechanical device parameter:

$$R_{eq} = \frac{b}{\eta^2} \quad C_{eq} = \frac{\eta^2}{k} \quad L_{eq} = \frac{m}{\eta^2} \quad \eta = V_{DC} \cdot \frac{\partial C}{\partial x} \tag{3.4}$$

where η is an electromechanical transduction factor between the rotor-stator applied voltage and the resulting electrostatic force. MEMS resonators are also characterized by the presence of a *feed-through capacitance* (C_{ft}) directly coupling the drive and sense port. This ends up in a circuital model as the one shown in figure 3.23, adding a contribution growing with ω which becomes eventually dominant for large frequencies.

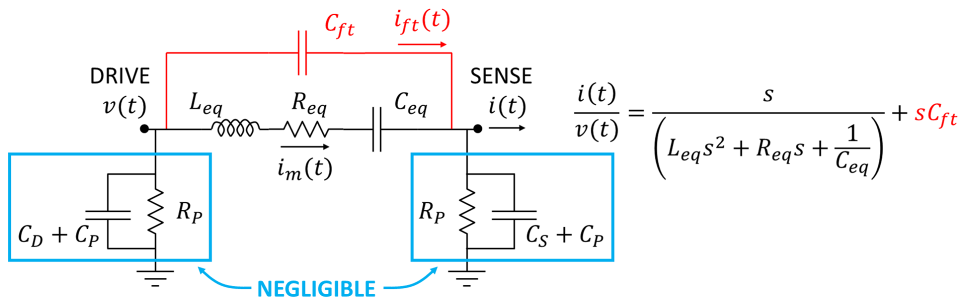

Figure 3.23: *Electrical model and transfer function of a MEMS resonator.*

This could cause the oscillator circuit to have more than one point which satisfies the Barkhausen conditions, resulting in more than one possible oscillation frequency, as visible in figure 3.24. This effect can be avoided, in a first approximation, adding low-pass filtering stages at frequencies higher than the resonance, but lower than the operational amplifier intrinsic one.

In the circuital model of figure 3.23 the resistances connecting drive and sense ports to ground (R_P) are so big that can easily be neglected, and the parasitic capacitances related to drive and sense stages and other parasitisms (($C_D + C_P$) and ($C_S + C_P$)) are between ground and another low

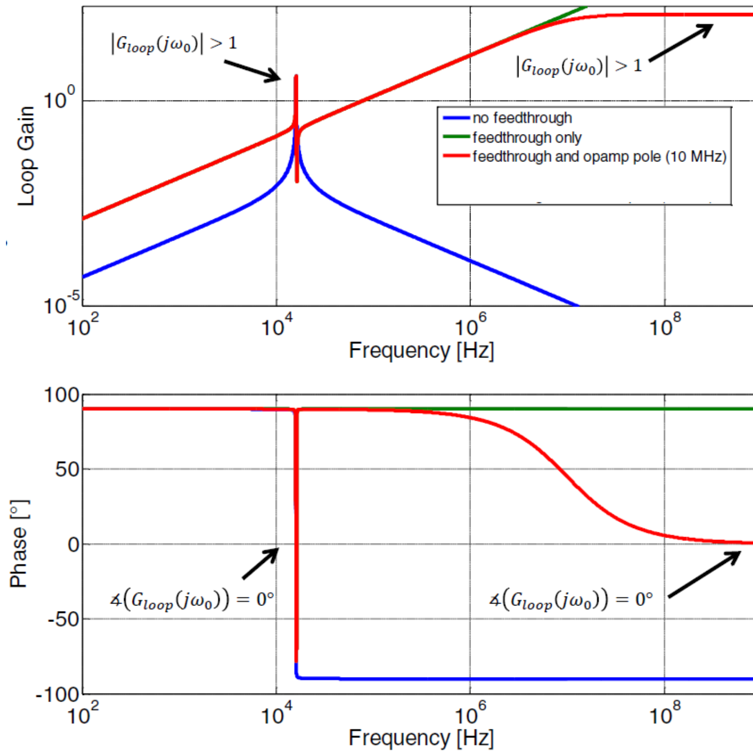

Figure 3.24: *Effect of the feed-through capacitance on the MEMS resonator transfer function. A second resonance frequency appears, and it needs to be filtered out.*

impedance - being it the output impedance or a virtual ground of an operational amplifier. Therefore, almost no current flows through them, and they can easily be neglected. The oscillator circuit, depicted in figure 3.25 is based on a trans-impedance amplifier front-end (40MΩ feedback resistance), because it induces a different phase shift on the signal with respect to the charge amplifier configuration, and in this implementation high performance as in the sense front-end stage are not needed. This is followed by an inverting high-gain stage that (i) provides the -180° phase shift to satisfy the Barkhausen criterion on the phase, and (ii) leads to saturation, thus providing the nonlinearity that lowers the loop gain down to 1 after the start-up, so to satisfy also the Barkhausen condition on the modulus [71]. A voltage divider is then used to lower the driving voltage waveform to values compatible with the desired resonator motion (about 3 μm). The oscillator does not need amplitude control (AGC [72]), as its goal is solely to provide a reference frequency.

A 160 kHz low-pass filter has been added to each stage in order to com-

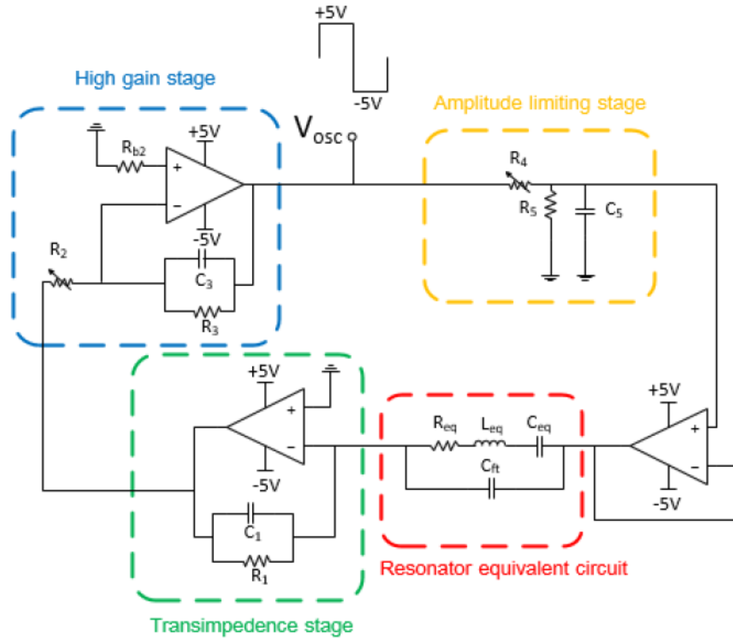

Figure 3.25: *Complete schematic of the oscillator circuit.*

pensate for the feed-through capacitance effects.

Current Generator

The saturated square wave of the oscillator circuit (V_{OSC} in figure 3.25), as well as the external wave in case of this choice, is sent to the input of a differential amplifier (AD8276 from Analog Devices [73]) through a buffer stage.

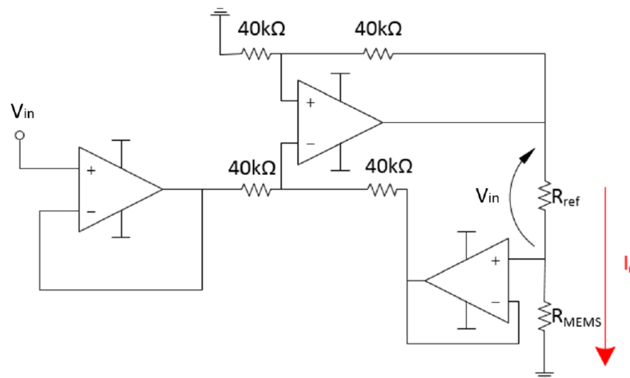

Figure 3.26: *Schematic of the current generator circuit which receives the saturated square wave from the oscillator as input.*

The circuit, visible in figure 3.26, applies the input voltage directly on the reference resistance R_{REF}, which has to be a very low tolerance resistor of a value chosen in order to obtain the desired current. The generated driving current I_0, with a frequency selected by the oscillator circuit, directly flows into the MEMS module as depicted in figure 3.4.

Complete schematic and picture of the 4-layer fabricated PCB are visible in figure 3.27 and 3.28 respectively.

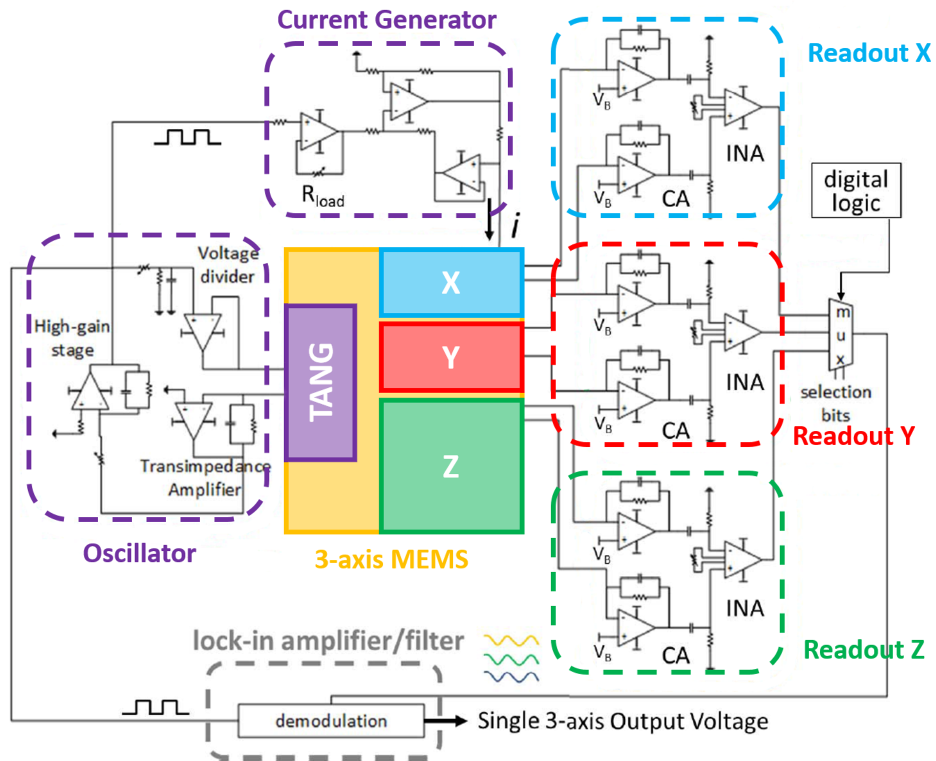

Figure 3.27: *Complete schematic of the designed PCB for the drive signal generation and readout of capacitive 3-axis Lorentz-Force based MEMS magnetic field sensor.*

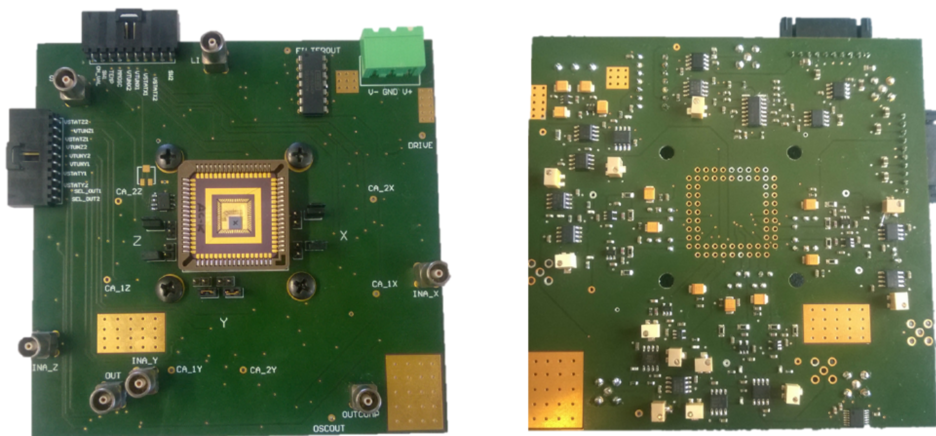

Figure 3.28: *Up and bottom view of the 4-layer fabricated PCB.*

3.4 Key parameters prediction

3.4.1 Sensitivity

Consider the differential capacitive magnetometers presented in section 3.2, with a nominal resonance frequency f_0 = 18.3 kHz, driven off-resonance by a quantity Δf = 200 Hz through an AC current with peak amplitude i. The sensitivity (scale-factor) in terms of system output voltage variation ∂V_{out} per unit magnetic field change ∂B can be written, referring to equation 2.14 and 3.3:

$$SF_V = \frac{\partial V_{out}}{\partial B} = SF_C \cdot \frac{\partial V_{out}}{\partial C} \cdot G_{eln} \tag{3.5}$$

In off-resonance operation the displacement along the sensing direction, caused by the AC Lorentz force $F_L = B \cdot i \cdot L_{eff} \cdot N_{loop,eq}$ (L_{eff} being the average spring length), is amplified by Q_{eff}. It is thus possible to derive the sensitivity expression per unit current consumption:

$$\frac{SF_V}{\partial i} = \frac{\partial V_{out}}{\partial B \cdot \partial i} = N_{loop,eq}\, L_{eff} \cdot \frac{Q_{eff}}{k_{eff}} \cdot 2\frac{C_0}{g} \cdot \frac{V_{bias}}{C_F}\, G_{eln} \tag{3.6}$$

In the equation above, k_{eff} is the effective device stiffness, in units of N/m. For the in-plane field sensing device, this corresponds (for small tilting angles) to the torsional stiffness divided by the square of the average torque arm, *d* (see figure 3.12). For the out-of-plane sensing magnetometer, it corresponds to the stiffness of one half of the device (anti-phase motion), pre-multiplied by a factor 2 due to the distribution of the Lorentz force across the springs. G_{eln} represents the gain of all electronic stages beyond the CA. With the nominal parameters given in tables 3.1 and 3.2, the nominal sensitivity per unit Lorentz current for a 200 Hz mode-split (Δf) turns out to be nominally identical for the IP and OOP devices, and independently of the quality factor value, equal to:

$$\frac{\partial V_{out}}{\partial B \cdot i} = 5.56\ \frac{\mu V}{\mu T\ \mu A_{rms}} \tag{3.7}$$

3.4.2 Electronic noise

With the front-end electronics described in section 3.3.2, all the noise considerations of section 2.2.2 directly apply. The electronic noise, in terms of V^2/Hz at the CA outputs, is independent of the device. Considering

the components described in section 3.3.2 (AD8065, featuring $\sqrt{\mathrm{S_{n,V}}}$ = 7 nV/$\sqrt{\mathrm{Hz}}$ and $\sqrt{\mathrm{S_{n,I}}}$ = 0.6 fA/$\sqrt{\mathrm{Hz}}$, as operational amplifier and 600 MΩ as feedback resistance), the op-amp current noise contribution turns out to be negligible in the system working frequency $\mathrm{f_d}$ (see figure 3.29). The feedback resistance $\mathrm{R_F}$ is dimensioned in such a way that its noise contribution is comparable to op-amp voltage noise, if a parasitic capacitance of 5pF is assumed.

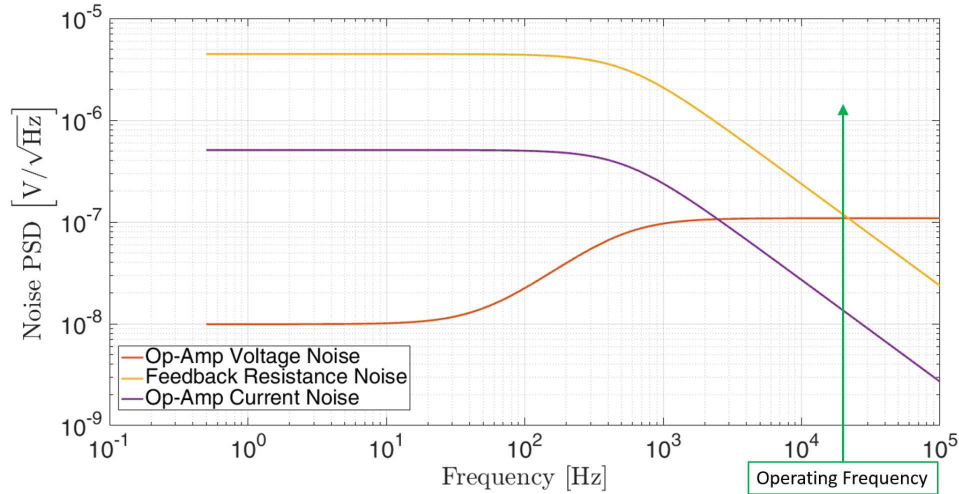

Figure 3.29: *Sense electronics noise contributions, expressed in terms of $V/\sqrt{Hz}$ at the charge-amplifier outputs.*

3.4.3 Damping coefficient and total noise estimation

Recalling the intrinsic thermo-mechanical noise formula for MEMS devices at a certain temperature T, which is the ambient temperature, and being $\mathrm{k_B}$ the Boltzmann constant:

$$\sqrt{S_{B,M}} = \frac{4}{i\ L\ N_{loop,eq}} \cdot \sqrt{k_B T b}\ \frac{nT}{\sqrt{Hz}} \tag{3.8}$$

the noise contributions of the two different devices can be estimated.

MEMS magnetometers (like gyroscopes) operate at pressures in the 1mbar range. With typical operating frequencies slightly above the audio band and typical gap dimensions, the Knudsen number turns out to be higher than 10. Working conditions hence fall within the free-molecule regime, where, according to standard classifications of rarefied gas-dynamics, collisions

between molecules themselves can be neglected [74], [75], [76]. Validations of this hypothesis can be found e.g. in [77], [78]. For this operating conditions, a small number of models are present in literature, and they are most concentrate on parallel-plates squeeze damping. Some examples can be found in [79], [80], [81]. An innovative approach using integral equation techniques based on the collisionless Boltzmann equation by Frangi et al. [82] has been validated on a bunch of simple test structures, implementing the most used drive and sense architectures in MEMS devices [83], and then used to estimate the total dissipation of the complex structures presented in section 3.2.3 and 3.2.4.

Looking at figure 3.30, in which all the noise contributions are considered at the system input (in terms of $\mathrm{T}/\sqrt{\mathrm{Hz}}$), for a 6V biasing voltage $\mathrm{V_{bias}}$ of the devices stators and a parasitic capacitance of 5pF, the MEMS thermo-mechanical noise turns out to be the dominant contribution. For a technology-limited package pressure of about 0.5mbar, the estimated damping coefficients for IP and OOP devices are $6.8 \cdot 10^{-7}\mathrm{Ns/m}$ and $6.5 \cdot 10^{-7}$ $\mathrm{Ns/m}$ respectively. Knowing the structures resonance frequencies, their Q values turn out to be about 1000 for the IP magnetometer and 800 for the OOP one. The intrinsic noise of the two devices is thus similar (145 $\mathrm{nT}/\sqrt{\mathrm{Hz}}$ and 165 $\mathrm{nT}/\sqrt{\mathrm{Hz}}$ for IP and OOP respectively), leading to a total system noise, at its operating frequency (18.1 kHz), of 150 $\mathrm{nT}/\sqrt{\mathrm{Hz}}$ for IP and 169 $\mathrm{nT}/\sqrt{\mathrm{Hz}}$ for OOP devices, coupled with their readout electronic chain.

This means that performance in line with the state of the art can be theoretically obtained for Lorentz current values of 100 $\mu\mathrm{A_{rms}}$ only. Noise continues to be dominated by the Brownian contribution up to parasitic capacitances in the order of 15pF.

In the presented noise analysis it has not been taken into account the phase noise of the oscillator circuit. It has been initially roughly estimated to be negligible with respect to the other noise contributions of the system, an assumption which is confirmed by the performed experimental measurements, presented in 4.

3.4.4 Considerations on power consumption

The system is on the whole compatible with low-power electronics based e.g. on the integrated readout presented in [64]. More in general, from an integrated circuit perspective, using only 100 $\mu\mathrm{A_{rms}}$ leaves as much as

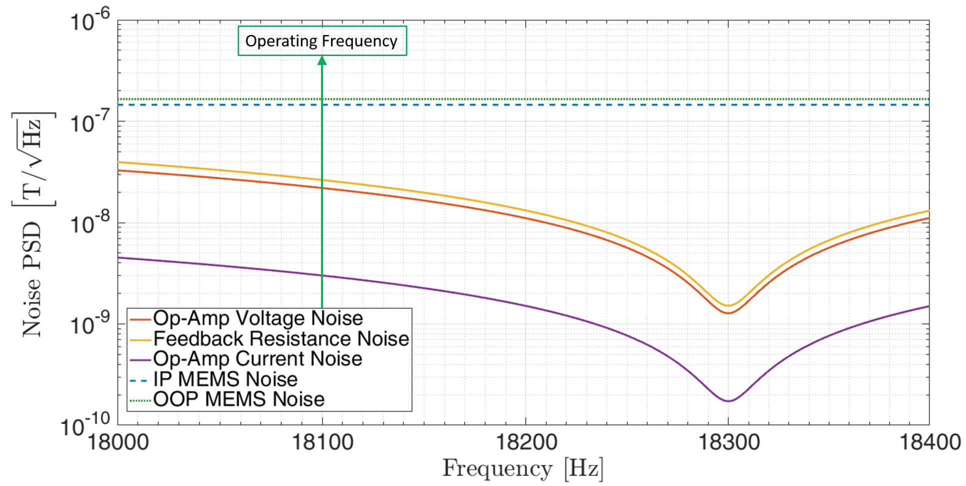

Figure 3.30: *System noise contributions in terms of $T/\sqrt{Hz}$ at the input. All the contributions are thus shaped by the MEMS transfer function, well visible in particular in the electronic ones.*

150 μA_{rms} for the electronics to be competitive with state-of-the-art overall current consumption of multi-DOF IMUs, in the order of 250 μA_{rms} [84].

CHAPTER 4

Performance characterization

4.1 Measurement Setup

Experimental characterizations are performed using a 3-axis Helmholtz coil magnetic field generator from *Micromagnetics Inc.*, which accommodates the driving and readout PCB described in section 3.3 (see figure 4.1). The setup provides a field generation accuracy of 300 nT, with maximum applicable field in the order of 5.5 mT per axis.

As shown in figure 4.2, the biasing voltages for all the electronics stages (± 12V) are provided by a laboratory DC voltage supply, while the voltage references for sense and tuning electrodes, together with digital signals for output selection, are provided by an analog/digital output generation board (*MCC USB-3105* from *Measurement Computing*). The output of the selected magnetometer channel is sent as an input to a Lock-In Amplifier (*HF2LI* from *Zurich Instruments*), which, using as a reference the signal coming from the driving oscillation circuit, demodulates the signal. The output of the tunable low-pass-filter which is embedded after the demodulation is sent to a 16-bit ADC (*MCC USB-1608GX* from *Measurement Computing*), which is connected to a PC. A *LabVIEW* interface have been designed to program the measurement conditions and the characterization

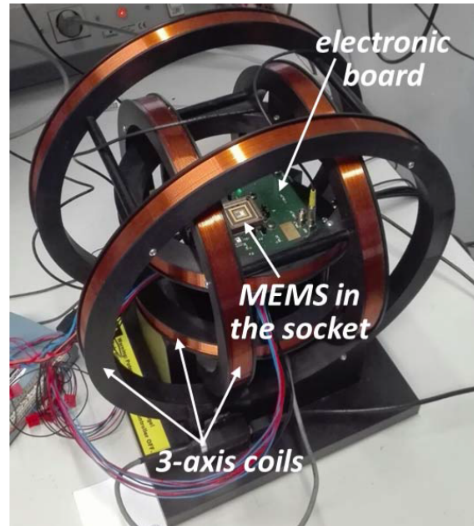

Figure 4.1: *Picture of the setup, with the MEMS mounted on a carrier, plugged into a socket on the driving/readout board within the Helmholtz coil setup.*

routine, to acquire and elaborate the data. This completely customized software is able to generate almost any kind of space-and-time-varying magnetic field shape: it is thus used to perform all the measurements presented in the following.

4.2 Performance Evaluation

4.2.1 Sensitivity

Two types of sensitivity characterizations are performed. The first one is obtained by sweeping the magnetic field from -5 mT to +5 mT along every axis, one at a time. The choice of this range is motivated by a continuous demand of extended FSR in consumer IMUs. The results are reported in figure 4.3, where (a) shows a measured scale-factor of 5.8 $\mu\mathrm{V}/(\mu\mathrm{T}\mu\mathrm{A}_{\mathrm{rms}})$ for the Z-axis device and a cross-axis rejection of 33dB and 42dB for the other two axis under Z-axis field (likely limited by manual alignment). Similarly, (b) and (c) show sensitivities for the twin X- and Y-axis devices in the order of 6.4 $\mu\mathrm{V}/(\mu\mathrm{T}\mu\mathrm{A}_{\mathrm{rms}})$. This value is slightly larger than predicted: a possible motivation is in an underestimation of the vertical capacitance between the rotational frame and the underneath stators, in particular when accounting the effect of perforating holes. The matching between the sensitivities along the three sensing axes is anyway quite good, and the cross-

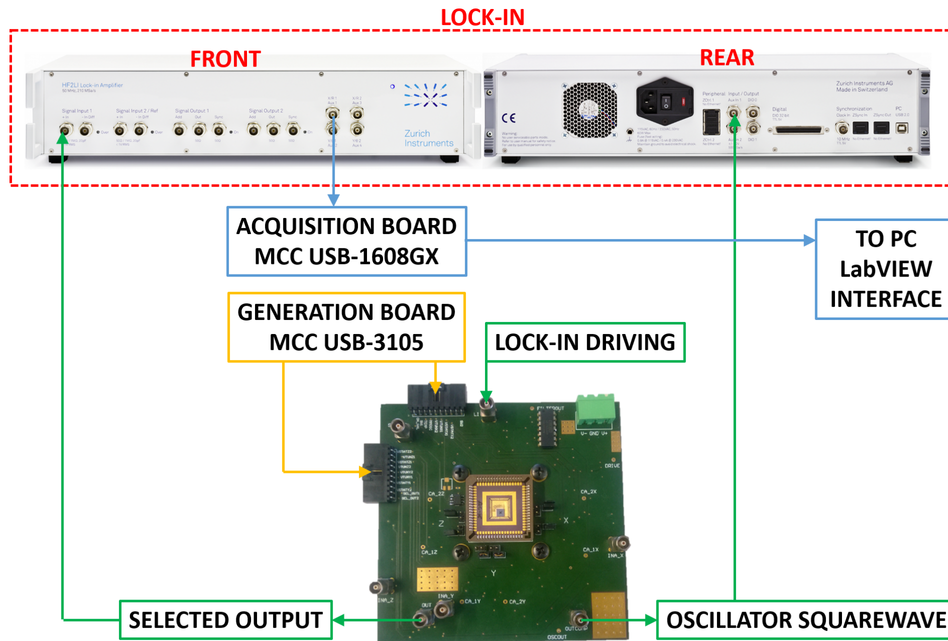

Figure 4.2: *Complete characterization setup.*

axis rejection for IP devices is always larger than 39 dB. The linearity error, calculated as a percentage of the FSR assumed as 5 mT, is lower than 0.3% along the tested magnetic field range (see figure 4.4).

The second type of sensitivity characterization consists in generating a sphere through a magnetic field vector of constant amplitude which rotates in the 3-D space quasi-stationarily in time (see figure 4.5b). This is repeated for different field modulus values. One purpose is to verify that the FSR of the proposed MEMS magnetometers shows no intrinsic limits related to cross-axis effects. This is on the contrary a typical limitation in devices based on magnetic materials: e.g. the FSR of a given axis of an AMR device is not limited by its linearity errors but it is rather limited by the flipping mechanism occurring when a field along an orthogonal direction occurs [4]. Figure 4.5a shows the obtained result for spheres having a growing field radius up to 5.5 mT. After correcting for the small sensitivity differences in the digital domain, the spherical shape is well kept up to the maximum applicable field.

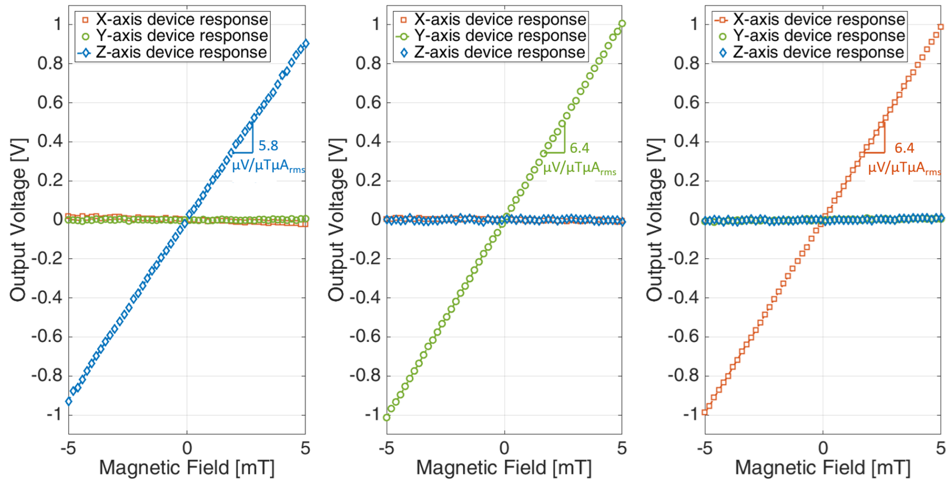

Figure 4.3: *Output voltage of the three different sensing channels versus an input magnetic field applied along (a) the Z-axis, (b) the Y-axis and (c) the X-axis. Corss-axis rejection is always larger than 33dB and 39dB for Z-axis device and X- Y- devices respectively.*

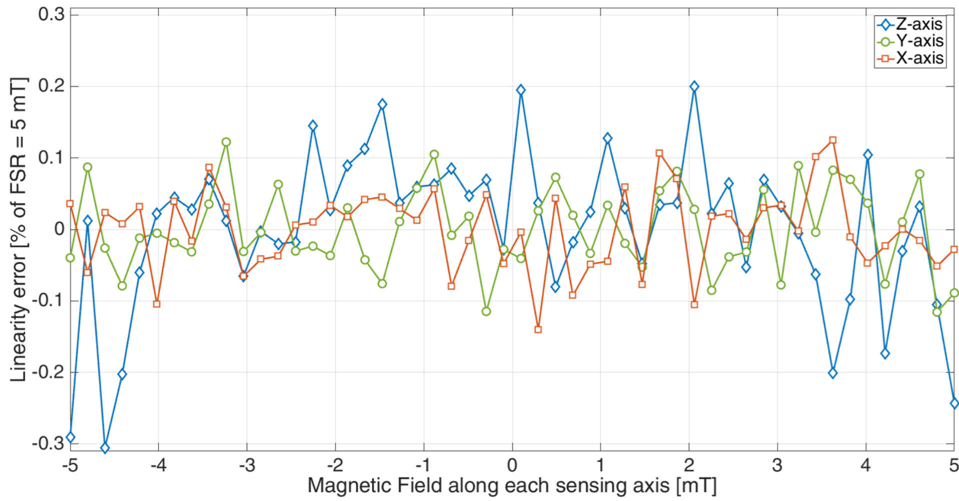

Figure 4.4: *Linearity error for X- Y- and Z-axis devices. All the structures show a very good linearity, lower than ±0.3% on the whole magnetic field range.*

4.2.2 Bandwidth

As stated in section 2.2.3, the bandwidth in off-resonance operation can be set up to large fractions of the frequency difference Δf. The required precaution is to avoid that the response peak occurring for an AC field frequency exactly matching the value Δf (200 Hz in this work) is amplified by

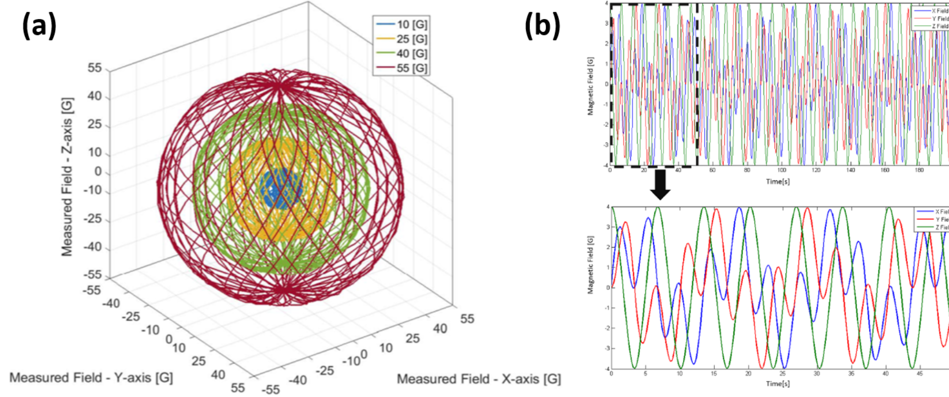

Figure 4.5: *The spheres of different 3-D magnetic field modulus in (b) are captured by the system while slowly sweeping (a) the tip of the magnetic field vector in space, so to describe a spherical path.*

the quality factor. This goal is achieved by using a filter at the LIA output, whose pole has a low-pass frequency of 50 Hz. Figure 4.6 reports the obtained results for all the devices when sweeping the field between 0.5 Hz to 500 Hz. The -3dB value is selected by the low-pass-filter cut-off frequency and thus it is the same for all the sensing axes. The peaks at about 200 Hz are visible and well filtered below the -3dB value.

4.2.3 Noise

Noise characterization, is performed by measuring the Allan deviation while the Lorentz current is serially injected into the three devices, biased as in operating conditions.

Allan variance, first proposed in 1966 [85] for the study of oscillators stability, is a currently used method for the noise evaluation of inertial MEMS sensors, particularly gyroscopes [86]. It represents a comprehensive method for the noise characterization of the sensor: besides the resolution, indeed, other contributions, such as the bias stability, are important for the evaluation of the goodness of a device.

Considering a signal y(t) acquired for a time T with a sampling frequency f_s, the total number of acquired samples is $N = T \cdot f_s$. Subdividing the total time T in observation intervals (clusters y_k) of length τ, with $M = T/\tau$ the number of cluster for each chosen τ value, the Allan variance is the variance of the difference of the mean values of two adjacent clusters. In the time and frequency domain respectively, it can be expressed as:

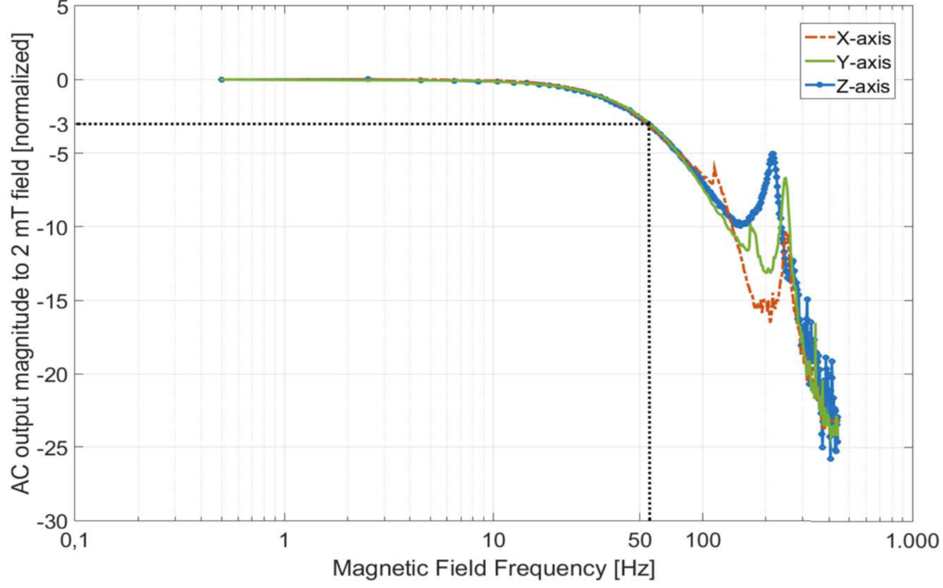

Figure 4.6: *Measured system bandwidth for all the magnetometers of this work. Note the -3 dB value matching about 50 Hz for all the devices. Beyond 200 Hz, the accuracy in the field generation by the Helmholtz coils setup degrades differently for the different axis.*

$$\sigma^2(\tau) = \frac{1}{2(M-1)} \cdot \sum_{k=1}^{M-1} (\overline{y_{k+1}} - \overline{y_k}))^2 \tag{4.1}$$

$$\sigma^2(\tau) = 2 \cdot \int_0^{\infty} S_y(f) \cdot \frac{sin^4(\pi f \tau)}{(\pi f \tau)^2} df \tag{4.2}$$

where the 4.2 represents the relation between the Allan variance and the Noise Power Spectral Density ($S_y(f)$) of the device. The processing performed by the Allan variance method is thus a band-pass filtering of multiple frequencies. The most common way to represent the Allan variance is a log-log graph as the one presented in figure 4.7, with τ on the x-axis and the Allan standard deviation on the y-axis.

Figure 4.7 also shows the most important noise contributions:

- White noise is represented by a -1/2 slope in the $\sigma(\tau) - \tau$ plot: for increasing values of τ both the passing frequency and the bandwidth decrease, thus decreasing the passing noise. The amount of white noise is computed multiplying $\sigma(\tau)$ by τ.

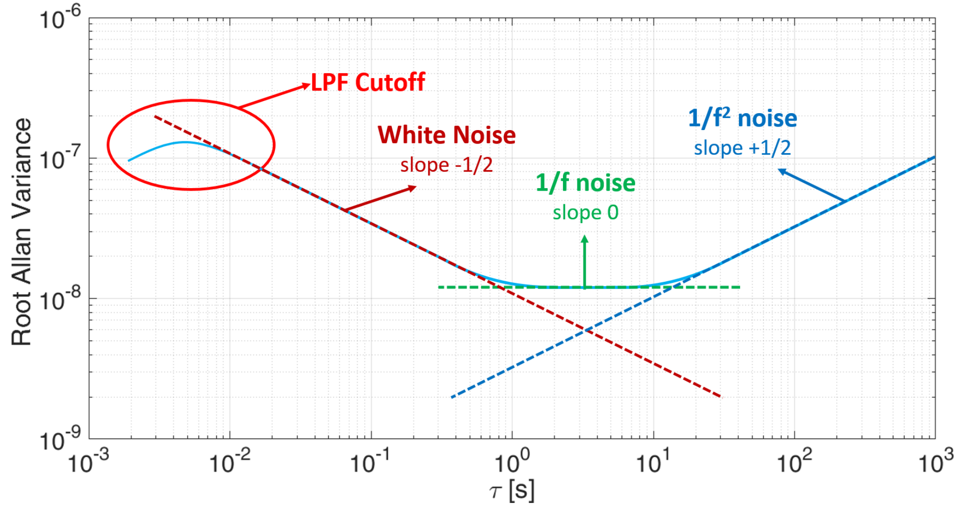

Figure 4.7: *Allan variance example plot, in which the three principal noise contributions of interest are highlighted: the white noise, the 1/f noise (bias stability) and the* $1/f^2$ *noise, corresponding to the -1/2, 0, 1/2 slope respectively.*

- 1/f noise is a plateau in the $\sigma(\tau) - \tau$ plot: to an increase of τ corresponds a reduction of the bandwidth and an increase of the noise, both proportional. The overall area is thus constant with the observation time variation. The bias stability is the lowest value of the Allan deviation graph, which is mainly representative of the offset drift.
- $1/f^2$ noise is represented by a +1/2 slope in the $\sigma(\tau) - \tau$ plot: it corresponds to the effect of temperature and related frequency changes, stresses, and in general any slow variation of the baseline.

The results of this characterization on the structures of sections 3.2.3 and 3.2.4, reported in figure 4.8, demonstrate a white noise density per unit current consumption of 20.3 $\mu T \mu A_{rms}/\sqrt{Hz}$ for the Z-axis device, including the electronic noise contribution. Results are obtained at a 100 μA_{rms} AC driving current. This value is in line with the predictions, if a parasitic capacitance of 17pF is considered, a value which is compatible with the used CLCC68 carrier/socket combination. This is confirmed by the fact that noise for the X- and Y-axis devices is quite similar to the Z-axis device, just improved to 18.5 $\mu T \mu A_{rms}/\sqrt{Hz}$ by the sensitivity difference. The matching between noise performance along all the axes is quite good. For an input current of 100 μA_{rms}, a FOM of 6.6 $\mu T \mu A_{rms}/\sqrt{Hz}$ per axis is thus obtained, and a 70 nT stability is reached at about 30s for both IP devices. For the Z-axis device, stability is poorer by roughly a factor 2 (160

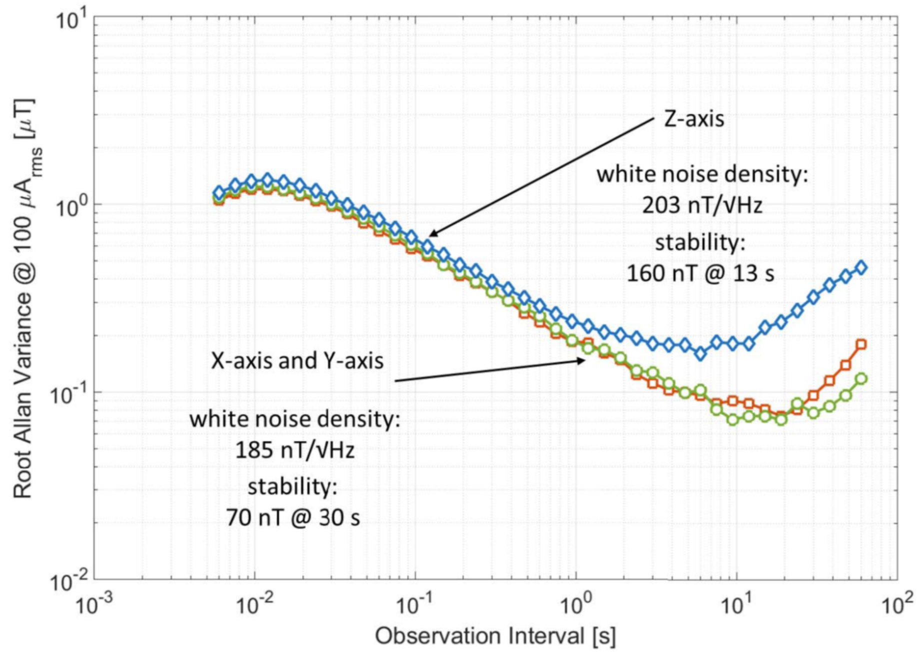

Figure 4.8: *Allan variance for the magnetic field density, for the three devices. Results are obtained at a 100 μA_{rms} AC driving current*

nT) at about half the observation time. Hypothesis to explain this behavior are presented in the following sections.

4.2.4 Offset

In section 2.3.3 the used offset compensation technique has been presented. Without any added stage and any added power consumption, a small DC voltage difference has been applied between the two stators of the differential capacitive cells of each magnetometer. As shown in figure 4.9, the initial offset, in the order of 5-6 mT for both IP and OOP devices, is trimmed down to the μT range, through a difference in the applied voltage between differential stators in the order of ±0.2V. As a consequence of the achieved compensation, the electronic FSR is now fully matched with the magnetic field sensing range.

This approach just compensates the offset without eliminating its source at the origin. This means that offset drifts - e.g. with temperature - will not be compensated via this technique. It is worth reminding that the bias instability observed in figure 4.8 can be likely ascribed to this issue.

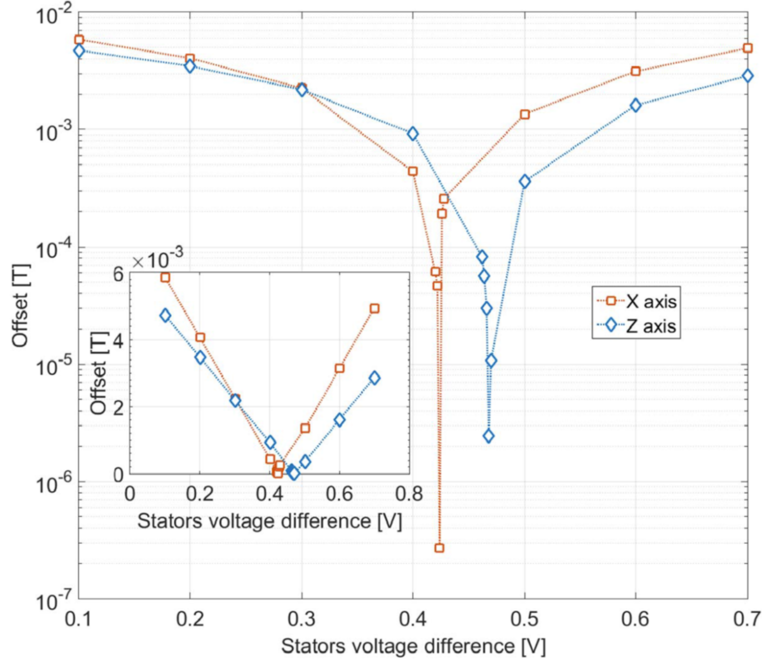

Figure 4.9: *Offset compensation of IP and OOP devices via the application of a small DC voltage difference at the virtual ground of the two charge amplifiers. The compensation is linear with the applied difference, as shown by the inset, and reaches values down to the μT range, as shown in the log-scale in the whole figure.*

4.2.5 Temperature behavior

Bias instability, likely due to offset drifts, has been measured in section 4.2.3. This parameter is mainly limited by temperature effects, which affect the structures resonance frequency, and in turn the frequency split Δf. Given the temperature coefficient of frequency for the magnetometer ($\mathrm{TCF_m}$) and for the MEMS resonator built inside the same module ($\mathrm{TCF_r}$), the $\mathrm{Q_{eff}}$ (see eq. 2.6) dependence on temperature variation $\Delta\mathrm{T} = \mathrm{T} - \mathrm{T_0}$ with respect to a reference temperature $\mathrm{T_0}$ can be written as:

$$Q_{eff} = \frac{1}{2} \frac{f_{m,0}\left[1 + TCF_m \Delta T\right]}{f_{m,0}\left[1 + TCF_m \Delta T\right] - f_{r,0}\left[1 + TCF_r \Delta T\right]} \tag{4.3}$$

where $\mathrm{f_{m,0}}$ and $\mathrm{f_{r,0}}$ are the resonance frequency at temperature $\mathrm{T_0}$ of the magnetometer and the resonator respectively.

Two are the major sources of frequency variation against temperature in MEMS devices: the first, as already seen, is related to temperature, while the second is related to structure geometry. The former is the unavoid-

able dependence of poly-silicon Young modulus on T, with a TCF of about -30ppm/K, which is called TCE [87]. The latter is related to the possible presence of residual stress after the fabrication process, whose value changes with temperature: in this case, the TCF value depends on whether the specific geometry allows a relief of the residual stress on the springs or not.

$$TCF = \frac{2}{\beta_{CC}} \cdot \frac{\partial \beta_{CC}}{\partial \sigma} \cdot \frac{\partial \sigma}{\partial T} + \frac{TCE}{2} + \frac{\alpha}{2} \tag{4.4}$$

β_{CC} is the modal constant of the specific excited mode of the structure, σ represents the applied stress and α is the thermal expansion coefficient.

In the optimum situation, TCE dominates both for resonator and magnetometers: the temperature drift of all the frequencies involved in the operation of the 3-axis magnetometer shows in this case the same coefficient $\mathrm{TCF_0} = \mathrm{TCF_m} = \mathrm{TCF_r}$:

$$Q_{eff} = \frac{1}{2} \frac{f_{m,0}\left[1 + TCF_0 \Delta T\right]}{(f_{m,0} - f_{r,0})\left[1 + TCF_0 \Delta T\right]} = \frac{1}{2} \frac{f_{m,0}}{f_{m,0} - f_{r,0}} \tag{4.5}$$

An identical TCF for $\mathrm{f_r}$ and $\mathrm{f_m}$ indicates stability in the $\mathrm{Q_{eff}}$, and in turn the sensitivity versus temperature.

To verify this, the magnetometer frequencies were measured through an electromechanical characterization platform [88], with the 3-axis module kept inside a climatic chamber. The temperature was swept between $5°\mathrm{C}$ and $95°\mathrm{C}$, by $10°\mathrm{C}$ steps. Figure 4.10 reports the measured results, where the frequency of the Y-axis magnetometer (diamond markers) and of the Tang resonator (triangle markers) show a temperature coefficient of frequency (TCF) of $-0.55\mathrm{Hz/K}$. The overall variation in the $\Delta\mathrm{f}$, shown in the inset, turns out to be in the order of ± 1 Hz in a range of 90 K, corresponding to about -30 ppm/K at a mode-split value of 200 Hz. The frequency of the Z-axis magnetometer showed a $\approx$30% larger TCF: this is probably caused by the presence of clamped-clamped springs, without chances of stress-relief. As shown in figure 4.10, however, a simple linear correction (applied to the scale-factor in the digital domain), brings the values (square markers) quite close to what obtained for the X- and Y-axis devices. The presence of a MEMS resonator built in the same module of the sensors is thus effective in the precise tracking of the frequency split $\Delta\mathrm{f}$.

4.2.6 Accelerations rejection

An important parameter for magnetometers used in consumer application is rejection to both DC and AC accelerations. In its final application indeed

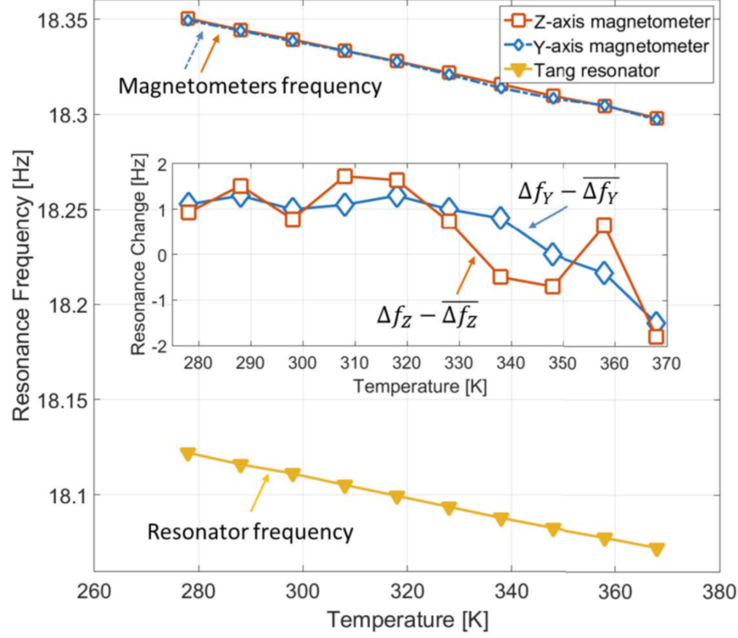

Figure 4.10: *Frequency behavior vs temperature for the magnetometers and the Tang resonator. The TCF for X- and Y-axis sensors perfectly matches the resonator one. The TCF for the Z-axis device well matches the resonator one after linear compensation. The inset indicates the frequency difference between magnetometers and resonator modes (i.e. the variation in the Δf term) versus temperature.*

the sensor will be mounted either within a smartphone or other mobile device, and will be constantly subject to different kinds of acceleration. If the acceleration induces a signal which could be read as a magnetic field effect, the measurement would be unequivocally altered. In order to highlight the harmfulness of accelerations, in the particular case of off-resonance operation, a numerical example is first given. Considering the effect of $a = 1\hat{g}$ acceleration on a device resonating at about 18 kHz, the corresponding displacement can be derived by:

$$x_{acc} = \frac{a}{\omega_{0,2}^2} = \frac{a}{(2\pi f_{0,2})^2} = 0.75nm \tag{4.6}$$

where $\omega_{0,2}$ is the resonance frequency of the acceleration sensitive structure mode (see tables 3.1 and 3.2). On the other side, the displacement x_{mag} occurring when measuring a 100 nT_{rms} magnetic field change at 100 μT_{rms} driving current - i.e. the best stability situation obtained in the Allan variance graph of figure 4.8 - considering the spring length and the stiffness

value of the proposed devices, and off-resonance operation with loop recirculation, is:

$$x_{mag} = \frac{B \cdot i \cdot N_{loop} \cdot L_{eff} \cdot Q_{eff}}{2 \cdot k_{eff}} = 75 fm \tag{4.7}$$

There are therefore 4 orders of magnitude between the displacement caused by an even small acceleration and the target field to measure. Even if vibrations usually occur at frequencies lower than the modulation frequency f_m, and even in presence of a good electronic filtering, canceling out such a huge difference remains challenging. The fact that accelerations represent a critical issue is, by the way, testified also by typical gyroscopes architectures based on tuning forks: it is indeed a parallel situation, where forces to be sensed are very small compared to those caused by accelerations. The strategy here adopted to improve robustness against these effect is the use, for all the axes, of an architecture that implements a capacitive sensing configuration which inherently rejects accelerations as a common mode, differing from most of previous works, especially for Z-axis devices [35], [46], [39], [44]. The strategy is further completed by shift of the mode sensitive to accelerations to high frequency.

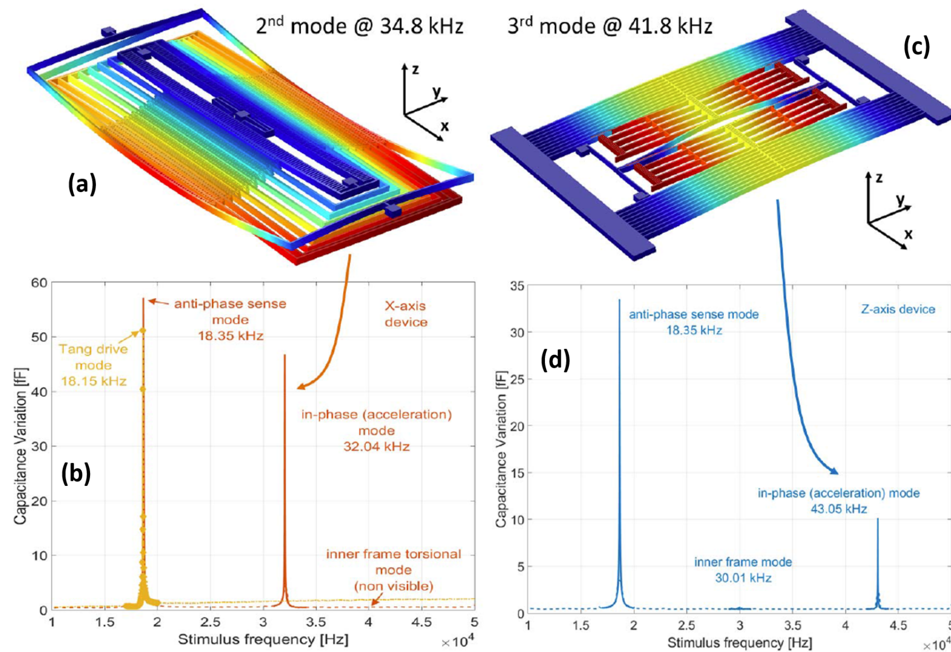

Figure 4.11

In particular, for device sensitive along the X- or Y-axis:

- accelerations along the Z direction (orthogonal to the substrate surface) are the most critical ones. Their effect is minimized because the structure is balanced around the mass center: this implies that an acceleration does not excite the first, differential mode but a high-order mode. This wing-like, in-phase torsional mode, presented in figure 3.14 and here reported in figure 4.11a, occurs at about 32 kHz, as experimentally demonstrated through an electromechanical characterization of the modes shown in figure 4.11b. Upward shifting the acceleration sensitive mode by a factor $\approx$2 turns into a $\approx$4-fold larger immunity, as suggested by equation 4.6. Besides, the excitation of such a mode gives rise to a common-mode capacitance variation, inherently rejected by the differential readout;
- the effects of accelerations along the X direction, parallel to the torsional beams, are minimum as the device is very stiff along this direction;
- accelerations along the other in-plane (Y) direction give rise to lateral in-plane displacements. The corresponding mode falls at about 43 kHz. Thanks to a 5 μm enclosure distance of the bottom electrodes mask within the frame mask, such lateral motions does not cause capacitance variations, as the electrodes facing area does not change.

For devices sensitive to the Z axis:

- accelerations along the X direction, parallel to the substrate surface, are the most critical ones for this device. Their effect is minimized by design thanks to the diamond-shaped geometry of the tuning fork, with clamped-clamped beams at its ends. This geometry is known to shift the in-phase mode to a frequency larger than the anit-phase mode. This is predicted by FEM simulations of figure 3.8, here reported in figure 4.11c, and experimentally verified in the modes electromechanical characterization of figure 4.11d. The upward frequency shift, in this case, gives a 5.5-fold larger immunity to accelerations than in a situation (like all those referenced above), where the mode sensitive to the accelerations is the same as for the magnetic field. Once more, for the proposed geometry, the effects of such a motion is a common mode, rejected in the differential readout;
- effects of accelerations along the order in-plane direction (Y), as well as of vertical (Z-axis) accelerations, are minimum as the device is very stiff along both these axes.

To proof the goodness of the design in terms of acceleration rejection, the sensitivity measurements described in section 4.2.1 were repeated under different conditions of accelerations. These include $1\hat{g}$ (DC) along the Z-direction (repeated 6 times), $\pm 1\hat{g}$ (DC) along the X-direction (repeated 3 times each), $\pm 1\hat{g}$ (DC) along the Y-direction (repeated 3 times each), and $\pm 3\hat{g}$ (AC) random-direction accelerations (repeated 3 times). To obtain these different accelerations while measuring the sensitivity, the whole setup was tilted or subject to shakes and shocks. The acceleration ground truth was obtained through a reference accelerometer rigidly mounted on the setup. The frequency of the applied AC accelerations is limited to $< 10\text{Hz}$ due to the bulky setup (figure 4.1).

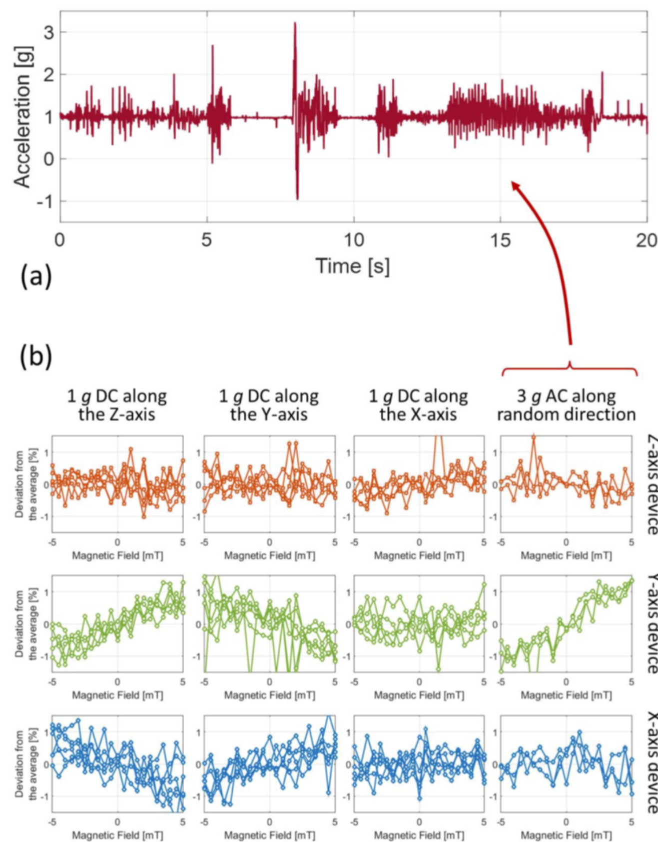

Figure 4.12: *(a) example of applied AC acceleration modulus profile; (b) deviations of the measured sensitivity from the average value, when operating measurements under DC and AC accelerations as indicated at the top of each column. Each row corresponds to a different device, as indicated to the right. For all the measurements, a sensitivity change lower than 1% is observed.*

Figure 4.12 reports a summary of the results: every column corresponds to a different type of applied acceleration, and every row to a different type of device. In each graph, the percentage deviation of each measurement with respect to the average sensitivity measurement from all these collected data is plotted versus the applied magnetic field. The number of curves in each graph corresponds thus to the number of repetitions of the measurement under that specific acceleration. One can note that deviations are always lower than 1%, thus indicating a good tolerance of the whole magnetic field sensing unit to such actions.

No significant offset change was found while tilting the device: the DC value (for no applied field from the Helmholtz coils) changed by few to few tens µT according to the change in the orientation with respect to Earth magnetic field.

4.2.7 Tolerance to magnetic field disturbances

Almost all the actual commercial magnetic field sensors requires to be mounted in a specific PCB location within the final system, far from magnetic field disturbances that can alter the magnetic domains behavior. The devices presented in chapter 3, and in general Lorentz-Force MEMS capacitive magnetometers, do not show inherent full-scale range limitations, due to the high linearity of the capacitive sensing architecture. In order to show the robustness of the sensor in presence of huge DC magnetic field offsets, an adjustable permanent magnet has been mounted within the Helmholtz coil magnetic field generator.

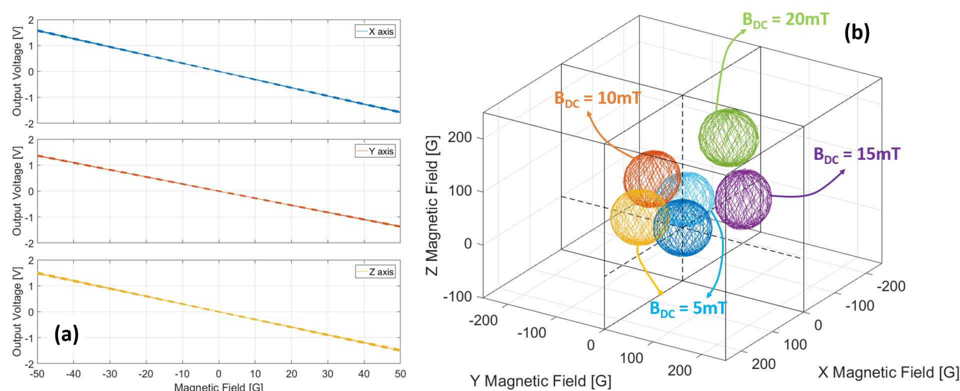

Figure 4.13: *(a) Sensitivity curves with different magnet positions. Their spread is in the order of the repeatability tolerance of the measurement; (b) 5-mT-magnetic field spheres, measured with different offsets due to different permanent magnet positions.*

As visible in figure 4.13a the sensitivity of the three axes does not change with different positions of the permanent magnet. The magnet position has thus been changed, providing constant offsets up to 20 mT. Magnetic field vectors, describing spheres with a 5 mT modulus, have then applied to the MEMS magnetometer. The results in figure 4.13b show how the spherical shape is maintained without noticeable distortion, even under huge magnetic offsets, making the sensor robust against high field disturbances typical of harsh environments. A dedicated software correction would allow the identification of the disturbance, its compensation and the continuation of the sensor operation [89].

4.2.8 Performance summary

The presented structures eventually demonstrate overall performance beyond the MEMS Lorentz-Force devices presented in literature and in line with the state-of-the-art commercial products. The most relevant parameters, to be directly compared with tables 1.3 and 1.2, are reported in table 4.1.

FSR [±mT]	Current [μA]	Resolution [nT/$\sqrt{\text{Hz}}$]	Pressure [mbar]	BW [Hz]	FOM [μTμA /$\sqrt{\text{Hz}}$]	Active Area [mm^2]	Die Size [mm^2]
OOP device						2.5x2	4x4
>25	33	203	0.5	>50	6.6		
IP device							
>25	33	185	0.5	50	6.6		

Table 4.1: *Most relevant parameter of the designed devices.*

The comparison with other MEMS magnetometers shows that, looking at each parameter individually, some works seem to be better with respect to the one presented, in some cases leading also to a better FOM. FOM is a parameter of merit but it can not take into account all the key parameters for consumer application. As an example, [38] and [36] push on resolution performance, which is one of the parameter evaluated by FOM, yet sacrificing FSR and bandwidth. The same is true also for commercial devices, moreover they are built in different technologies, which inherently have advantages on some parameters while disadvantage on others. Looking at the overall performance, thus, the presented sensor is beyond the state of the art of MEMS magnetometers, and it is in line with the actual commercial devices.

CHAPTER 5

An innovative single-mass 3-axis Lorentz-Force MEMS Magnetometer

5.1 Motivations and constraints

The last limiting parameter of Lorentz-Force MEMS magnetometers towards the integration in commercial IMUs for consumer application is the *area occupation*. Performance shown in previous chapters are better than or comparable with state of the art commercial magnetometers, both in terms of full-scale-range, linearity, resolution, bandwidth and power consumption. However, an active area of about $2.5{\times}2\ \mathrm{mm}^2$ is not compatible with consumer packages dimensions. As a representative example, in order to be competitive they must fit into a $2{\times}2\ \mathrm{mm}^2$ finished product, together with a 3-axis accelerometer to form a 6-axis eCompass. Looking at figure 5.1 it means that a 3-axis magnetometer has to fit into about a $700{\times}500\ \mu\mathrm{m}^2$ active area, which is about a 15-fold improvement.

Pursuing the way of three single-axis structure is therefore not possible: it is mandatory to find a way to integrate all the three sensing axes into one mechanical structure, a strategy exploited nowadays for almost all consumer gyroscopes.

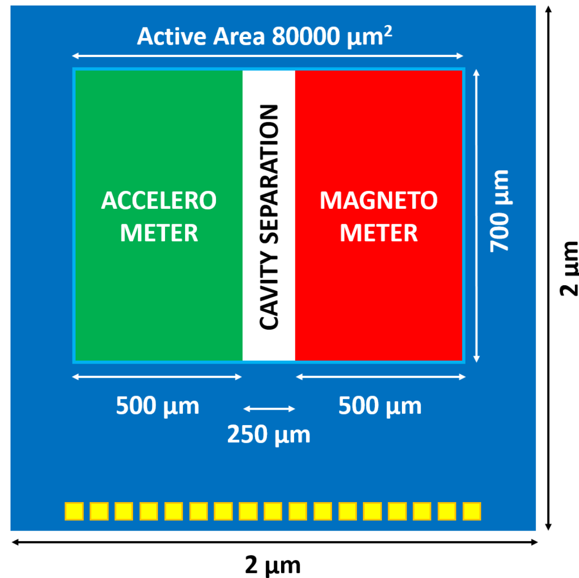

Figure 5.1: *Schematic package layout illustrating the required dimensions the 3-axis magnetometer has to fit in order to obtain a 2×2 mm^2 6-axis eCompass. The cavity separation is required as the accelerometer needs a pressure of about 50÷70 mbar, while the magnetometer operates at pressure in the mbar range.*

5.2 Structure design

5.2.1 Mechanical design

The monolithic mechanical structure - designed to be fabricated with 24-µm-thick ThELMA technology from STMicroelectronics - needs to be sensitive to the three magnetic field components individually, and at the same time it has to guarantee the spiral path for the current. As stated in chapter 2, indeed, the loop number is the key feature to boost both sensitivity and resolution at the same time. The structure needs thus three resonant modes, well decoupled in terms of mechanical movement and very close one another in terms of resonance frequency. A possible implementation of such a structure, presented in figure 5.3, is composed by an external frame sustaining the spiral loops. These loops are all connected by serpentine links - as in the 1-axis devices presented in chapter 3 - and sustain a parallel-plate sensing frame for the in-plane motion sensitive to a Z-axis external magnetic field. The structure needs also to perform two torsional motions, in order to be sensitive to the two X- and Y- magnetic field directions. For this reason, a torsional spring to decouple the out-of-plane motion of the

loops and the parallel-plate frame is needed. When torsional modes are excited, indeed, the parallel-plates sensing frame has ideally to remain still in its rest position. This is easily achieved on the X- torsional mode, thanks to the inner anchor points which decouple the motion of the loops and the sensing frame, while it is more difficult to obtain on the Y- torsional mode. The most important functional blocks of the structure, shown in the insets of figure 5.3, are described in details in the following:

- *external frame*: to decouple the motion of the two torsional modes, shown in figure 5.5. Thanks to the six *torsional springs* - two between the frame and external anchor points along the Y- symmetry axis, and four connecting the loops with the frame and the inner anchor points (along the X- symmetry axis) - the frame plays a role in the X-sensitive mode (see figure 5.5a), remaining unexcited in the Y-sensitive one (see figure 5.5b). This makes the two torsional motions well independent one another, allowing the X- and Y- magnetic field components to be detected without any intrinsic cross-axis effect;
- *tuning fork*: as shown in the inset labeled "tuning fork" of figure 5.3, the structure features a particular kind of tuning fork. It does not connect to the structure along its Y-direction symmetry axis, as a standard one, but it is splitted along that axis and each half is mirrored (1). The two halves, connected to the parallel-plate frame at its end points, are linked through a central double-folded spring (2), in order to couple but not fix them one another. Two thin straight springs (3) connect the two mid points of the tuning fork to a fixed structural part, giving a high stiffness to the out-of-plane translating motion, at the same time adding a negligible stiffness to the in-plane translating mode. This allows the rejection of undesired out-of-plane modes of the parallel-plate sensing frame, without playing any role in the in-phase in-plane Y-acceleration-sensitive mode (figure 5.4a). This allows to make this mode resonate about 10 kHz away from the anti-phase in-plane desired mode (see figure 5.4b);
- *central decoupling spring*: it is necessary to decouple the movement of the parallel-plate sensing frame and the Y-torsional mode. This is achieved by means of a folded spring (4) which is connected, through thick straights links (5), to the loops on one side and to the parallel-plate frame on the other side. The folded spring is designed to be as close as possible to the structure center, thus exhibiting a low torsional stiffness. This allows the parallel-plate frame to remain in its rest

position while the loops performs the torsional motion shown in figure 5.5b. Being the folds relatively short, their stiffness in the in-plane motion is instead high enough to avoid them playing any role in the determination of the anti-phase in-plane translational mode, as visible in figure 5.4b.

As visible in figure 5.5, the resonance frequencies of the two torsional modes are dimensioned to have, in operation, a 600 Hz mismatch one another. Depending on the electrostatic softening caused by the stator biasing, the three natural resonance frequencies are designed at three different appropriate values. As visible in figure 5.4 and 5.5, indeed, the Z-sensitive mode is designed to resonate at about 48.5 kHz without any bias, in order to make it resonate at 48 kHz with 6V voltage difference between rotor and stators. X- and Y- sensitive modes are instead designed to naturally resonate at about 49 kHz and 50 kHz respectively. As the electrostatic softening is different for the two movements, they end up to resonate, in operation, at 48.1 kHz and 48.7 kHz respectively. The in-plane Z-field sensitive mode frequency f_Z will thus be matched with the X-sensitive mode one f_X, so that a drive frequency f_d of 48.4 kHz would allow to operate with a frequency split of 300 Hz for all the three modes. The frequency reference f_d is provided by a Tang resonator similar to the one presented in section 3.2.5, designed, in this implementation, to resonate at 48.4 kHz. The frequency increase with respect to the structures presented in chapter 3 is due to the dimensional constraints shown in section 5.1 coupled with technological constraints on the minimum metal width, resulting in an increase of the structure stiffness (k). On one side, thus, the stiffness increase lowers the structure performance, while on the other side the higher frequency increases the Q_{eff} value for the same frequency split, allowing to obtain comparable performance both in terms of sensitivity (see equation 2.14) and resolution (see equation 2.26).

As visible in figure 5.2, in order to maximize the output signal, the sensing area for the two torsional modes is maximized. Sense electrodes (SENSE X and SENSE Y) cover indeed the largest possible area underneath the structure parts which perform differential motion for the corresponding mode. In-plane movement detection is instead performed through nested parallel-plates cells. All the movements feature differential sensing, in order to reject common mode movements due e.g. to accelerations along the three axes. Tuning electrodes have also been designed for all the three sensing modes: they are used to correct imperfections due to over- or underetch, or residual stresses after fabrication, bringing back the resonance fre-

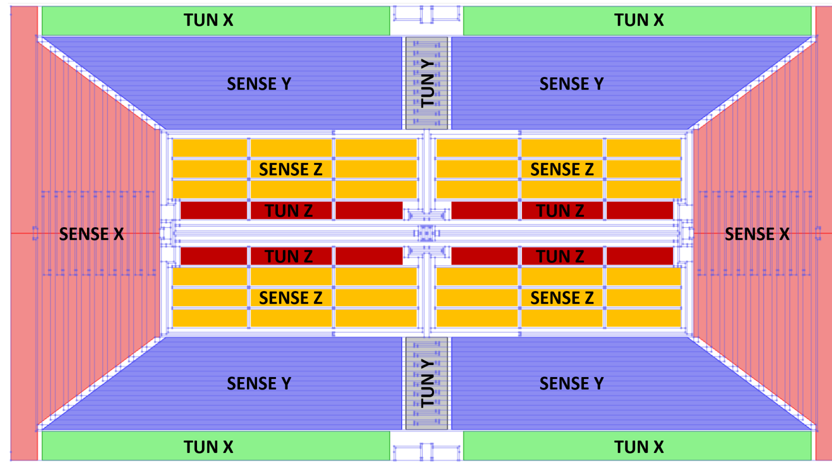

Figure 5.2: *Schematic view of electrodes for the sense and tuning of all the three modes.*

quencies to the desired ones. Electrodes area are designed to obtain a span Δf_{TUN} of at least about 500 Hz for each axis, as reported in table 5.1.

Axis	f_{min}[Hz]	f_{op}[Hz]	f_{max}[Hz]	Δf_{TUN}[Hz]
X	47268	48100	48374	1106
Y	46696	48700	49350	2654
Z	47686	48100	48237	551

Table 5.1: *Resonance frequency tuning ranges for the three modes.*

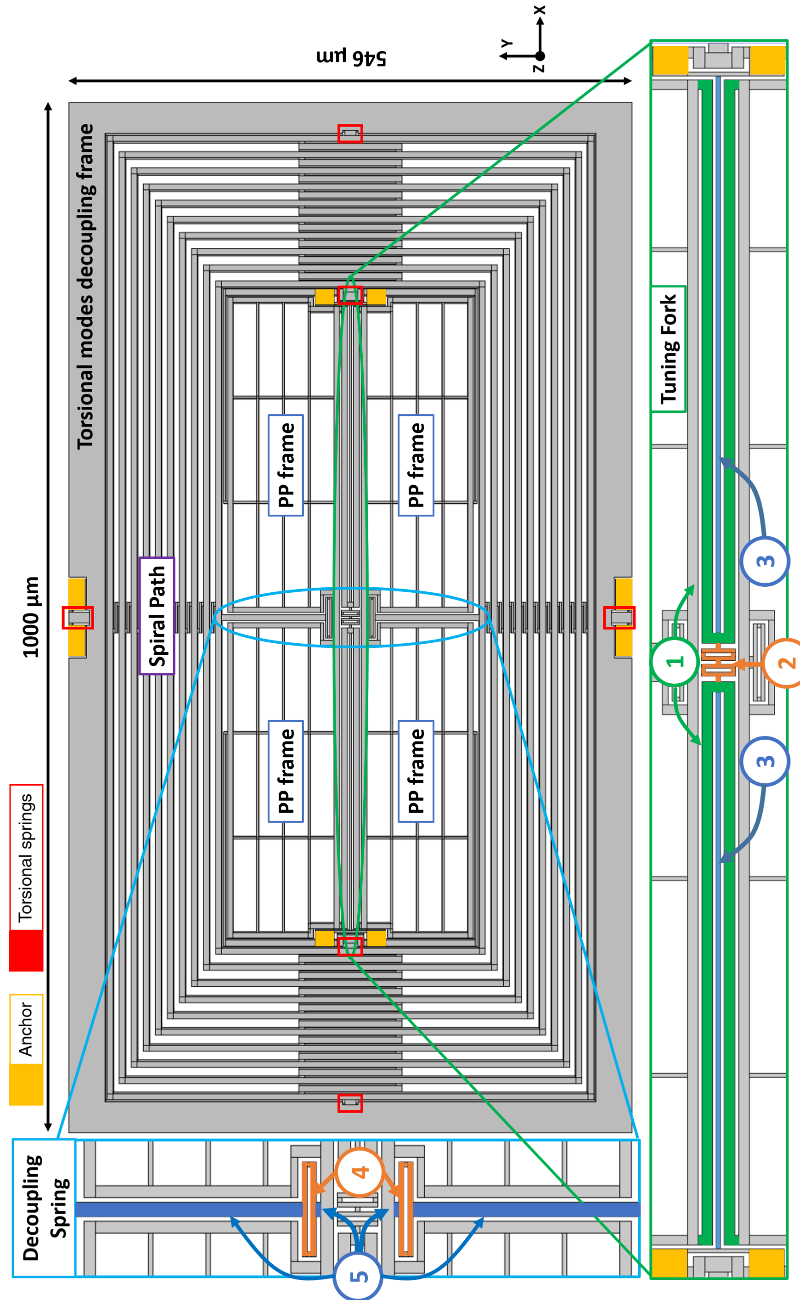

Figure 5.3: *Structure of the designed single-mass 3-axis Lorentz-Force MEMS magnetometer. Constitutive elements are put in evidence: parallel-plate sensing frame to detect the anti-phase in-plane movement caused by a Z-axis field, spiral path for the current recirculation, decoupling frame for the two torsional modes responsible for the detection of X- and Y-axis field, and the particular tuning fork shape.*

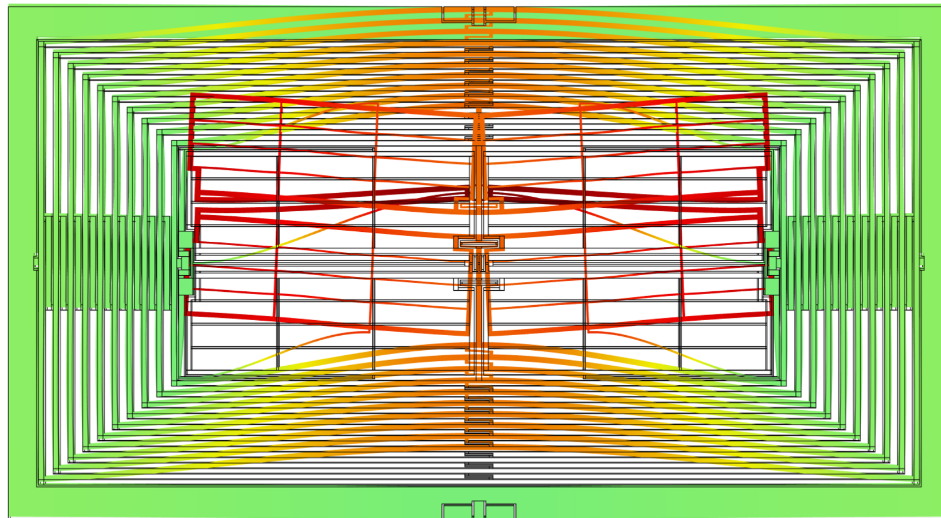

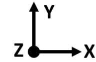

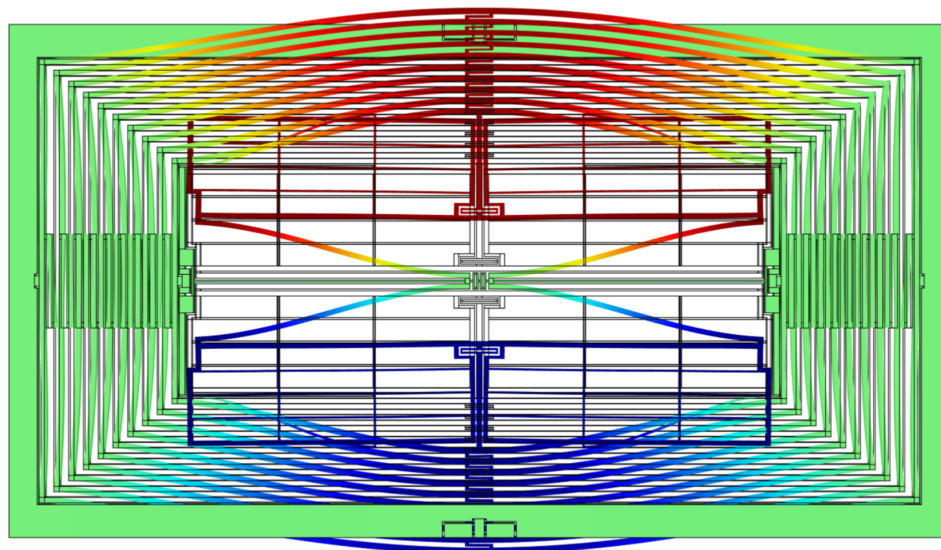

Figure 5.4: *In-plane modes: (a) in-phase movement sensitive to an acceleration along the Y-axis. It is designed to have a resonance frequency about 10 kHz lower than the (b) desired anti-phase mode, excited by the presence of an out-of-plane magnetic field.*

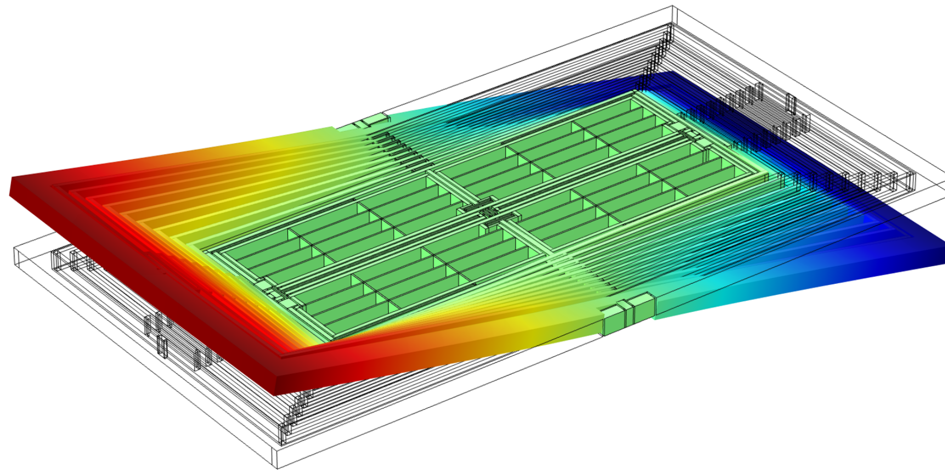

out-of-plane X-field mode

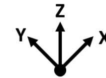

Natural resonance frequency $f_{0,N}$ = 48925 Hz

In-Operation resonance frequency $f_{0,OP}$ = 48100 Hz

---

out-of-plane Y-field mode

Natural resonance frequency $f_{0,N}$ = 49957 Hz

In-Operation resonance frequency $f_{0,OP}$ = 48700 Hz

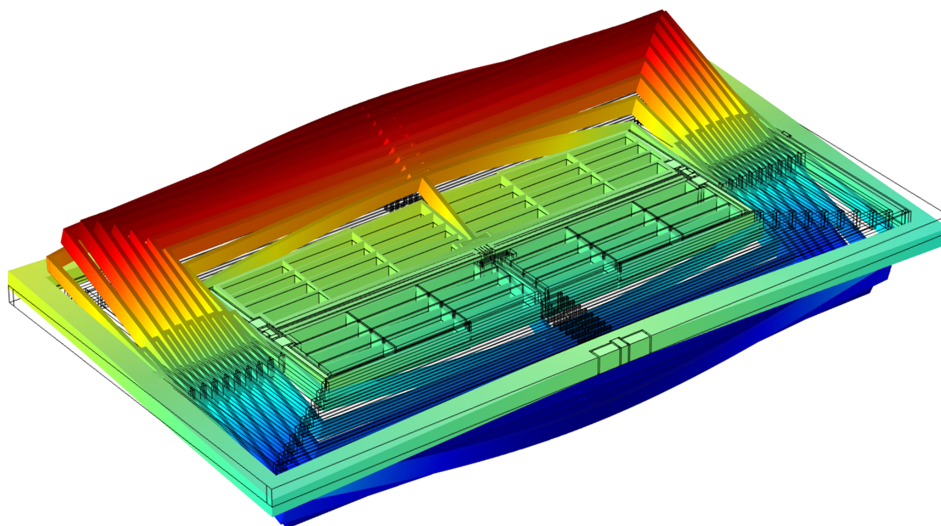

Figure 5.5: *Torsional modes: responsible for the detection of an external magnetic field (a) along the X-axis, (b) along the Y-axis.*

5.2.2 Electrical design

Though the structure is symmetric from a mechanical point of view, the spiral current path is still guaranteed by a metal layer deposited on top of the polysilicon one. The current flows through the low-resistive aluminum path as shown in figure 5.6.

It is worth notice that it has also been studied the possibility of designing a spiral (asymmetric) polysilicon structure, so to avoid the need for the metal layer to be deposited on top of the serpentine links. This implementation turned out not to be feasible because the intrinsic mechanical asymmetry makes the two torsional mode shapes to be the more cross-coupled the more their resonance frequencies become closer one another, thus making indistinguishable the two in-plane magnetic field components.

As no insulator layer is present between the sustaining polysilicon and the metal one, some expedients have been adopted to minimize the current leaky paths. In the two insets of figure 5.6 are indeed shown the two different implementations of the links connecting the springs. Ideally they would have to be as resistive as possible, which means as long and as thin as possible. However, there are two trade-offs:

- the *serpentine-links* connecting the *longer springs* need to be very rigid to transfer all the Lorentz force to the parallel-plate sensing frame, so to maximize its in-plane movement. This means they ideally have to be as short and as thick as possible, which is in contrast with what stated above. The adopted compromise is a 2 μm wide and 30 μm long link.

- the *serpentine-links* connecting the *shorter springs* need to let a metal layer be deposited on top of them, so to guarantee the spiral path of the current. This happens only if the resistance of the corresponding spring part not covered by metal is large enough to maximize the resistance of the polysilicon leaky path with respect to the resistance of one metal loop. This means a serpentine as long as possible, which have a negative impact on the stiffness and shape of the X- and Y-torsional modes. The adopted compromise is a 6 μm wide and 100 μm long link.

The 23-mm-long metal path features a total nominal resistance of 185Ω, while the small serpentines and the leaky paths on the springs are about 300Ω each. This leads to a resistive model similar to the one of figure 3.2, with $\mathrm{R}_{\mathrm{link}}$ also connecting the shorter springs, and 10 loops. The improved

ThELMA process in which this device would be fabricated feature a different etching technique for the metal layer, allowing to obtain a rectangular section 700nm thick and 5 µm wide. Current flow FEM simulation has thus been performed. Whose result, visible in figure 5.7, shows that polysilicon leaky paths are responsible for a current loss of 9% only, leading to an effective loop number $N_{loop,eff}$ of 9.1.

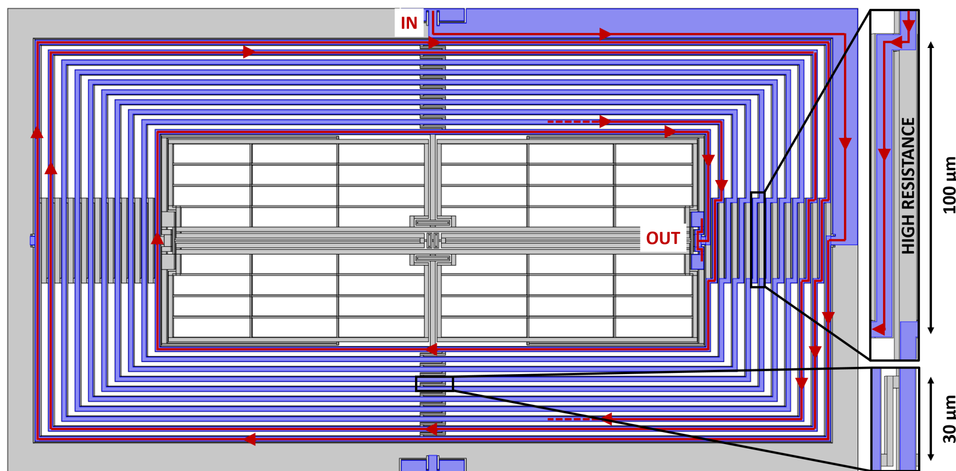

Figure 5.6: *Metal layer and corresponding current path for the monolithic 3-axis structure. In the insets the two serpentine-link implementations are shown.*

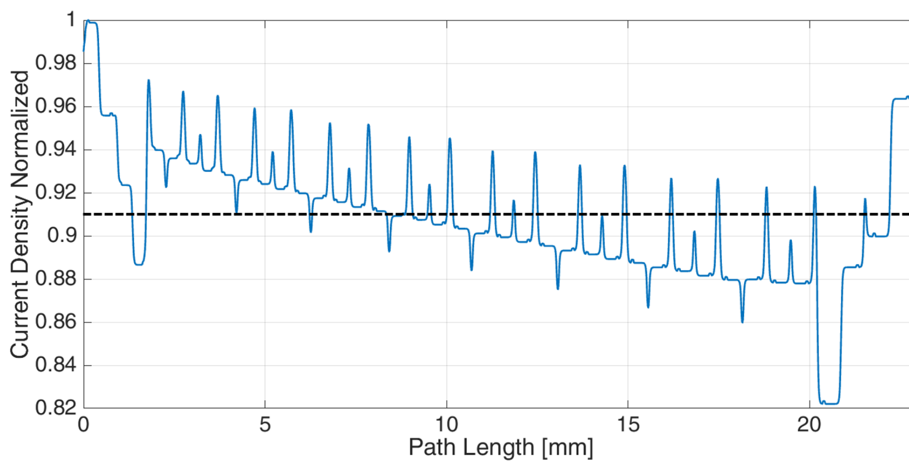

Figure 5.7: *Current density along the whole 23-mm-long aluminum path. The peaks correspond to the serpentine links. These leaky paths cause a 9% loss in terms of current concurring to generate Lorentz-Force, leading to an equivalent number of loops of* $N_{loop,eff} = 9.1$

Parameter	Unit	Value
Area	μm^2	1000 x 546
Biasing Voltage	V	6
Driving Current	μA_{rms}	100
X-field mode		
Effective stiffness	N/m	320
Quality factor	-	4000
Vertical gap	µm	1.2
Single-ended rest capacitance	fF	408
Average Lorentz length	µm	367
Natural (untuned) frequency (B_X mode) ($f_{0,Nx}$)	Hz	48925
In-operation frequency (B_X mode) ($f_{0,OPx}$)	Hz	48100
Y-field mode		
Effective stiffness	N/m	353
Quality factor	-	4000
Vertical gap	µm	1.2
Single-ended rest capacitance	fF	389
Average Lorentz length	µm	795
Natural (untuned) frequency (B_Y mode) (f_0y)	Hz	49957
In-operation frequency (B_Y mode) ($f_{0,OPy}$)	Hz	48700
Z-field mode		
Effective stiffness	N/m	260
Quality factor	-	3000
Gap	µm	1.8
Single-ended rest capacitance	fF	394
Average Lorentz length	µm	795
Natural (untuned) frequency (B_Z mode) (f_{0z})	Hz	48549
In-operation frequency (B_Z mode) ($f_{0,OPz}$)	Hz	48100

Table 5.2: *Most relevant parameters for all the three resonant modes of the presented structure.*

5.3 Key parameters evaluation

5.3.1 Sensitivity

In order to better evaluate the sensitivity of the device, reliable capacitance estimation is required. As the monolithic structure features an high electro-mechanical complexity, capacitive simulations have been carried out exploiting *Comsol Multiphisics*, which also allows to accurately take into account electric field fringe effects. The extracted values, together with other significant parameters for all the three axes, are reported in table 5.2.

With sensing stators biased at 6V and using a 100 μA_{rms} driving current, in case of off-resonance operation with a 300 Hz frequency split (Δf) all the three axes exhibit sensitivity values in line with the one presented in chapter 3, with a 10-fold saving in terms of area occupation. The estimated values are reported in table 5.3.

Axis	$\mathbf{SF_C}$ [aF/(mT)]	$\mathbf{\Delta C_{FSR}}$ [fF]	$\mathbf{SF_V}$ [$\mu V/(\mu T \mu A_{rms})$]
X	80	0.4	1.92
Y	150	0.75	3.65
Z	136	0.68	3.3

Table 5.3: *Estimated value for the sensitivities of the three axes.*

5.3.2 Resolution

With an estimated quality factor (see section 3.4.3) of about 3000 for the anti-phase in-plane Z-sensing mode, and about 4000 for the two torsional modes, all the noise contributions of the three axes and related front-end electronics are reported in figure 5.8 at the charge-amplifier outputs.

The figure shows the noise around the system operating frequency f_d, that is exactly where the different contributions have to be compared each other: it is clear that the thermo-mechanical noise dominates for all the three axes. In order to evaluate the noise in terms of magnetic field at the system input, each noise contribution has to be scaled by the sensitivity of the related axis. This means that the electronics noise has a different weight, in terms of input equivalent magnetic field, for the three sensing modes, even if in terms of voltage at the charge amplifier outputs it has a unique value. The values of all the noise contributions are reported in table 5.4 both in terms of $nT/\sqrt{Hz}$ and in terms of minimum detectable magnetic field for a 25 Hz bandwidth.

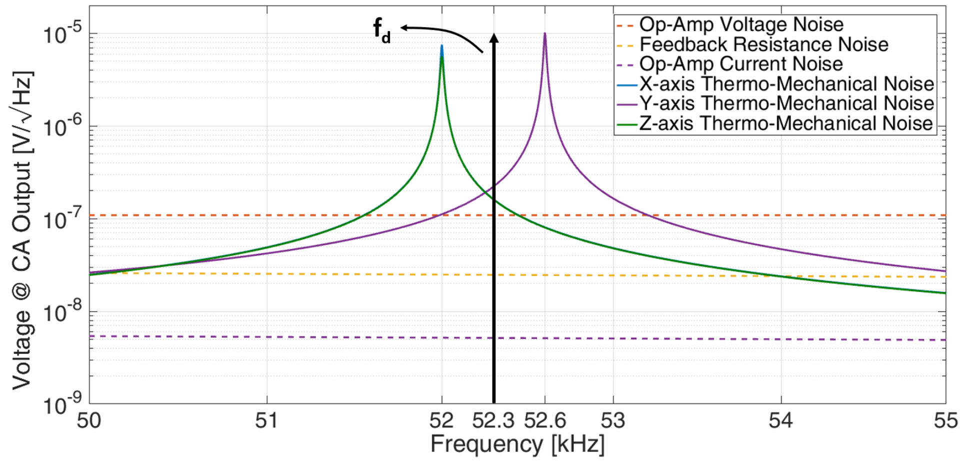

Figure 5.8: *Noise contributions at the charge amplifiers output. At the system working frequency (f_d), intrinsic thermo-mechanical noise is the dominant contribution for all the three axes.*

Axis	**Thermo-Mechanical** $[nT/\sqrt{Hz}]$	**Op-Amp Voltage** $[nT/\sqrt{Hz}]$	**Feedback Resistance** $[nT/\sqrt{Hz}]$	**Total** $[nT/\sqrt{Hz}]$	**FOM** $[\mu T \mu A_{rms}/\sqrt{Hz}]$	**Resolution @ 25 Hz** [nT]
X	201	114	28	**233**	7.6	1150
Y	96	60	15	**114**	3.7	550
Z	136	66	16	**152**	5.0	750

Table 5.4: *Estimated noise contributions and minimum detectable magnetic field for a 25 Hz bandwidth for the three axes.*

Even for the noise, the performance of the device are in line with, or better than, the device of chapter 3, but they are obtained with a 10 times smaller structure.

The obtained resolution performance are well suitable for compassing application, and with the improvements depicted in the following section, Lorentz-Force MEMS magnetometers could become suitable commercial devices, allowing navigation in consumer applications.

5.4 Future perspectives of the research

5.4.1 Future work on the presented device

At the time of this writing the presented structure and its working principle are under patenting process. In order to effectively validate the proposed design, together with its predicted performance, it is necessary to fabricate and test it. This step will be carried out by STMicroelectronics, thanks to its 24-µm-thick ThELMA technology, in the next months. Figure 5.9 shows the 2D CAD layout of the polysilicon, metal and anchor layers designed for masks definition.

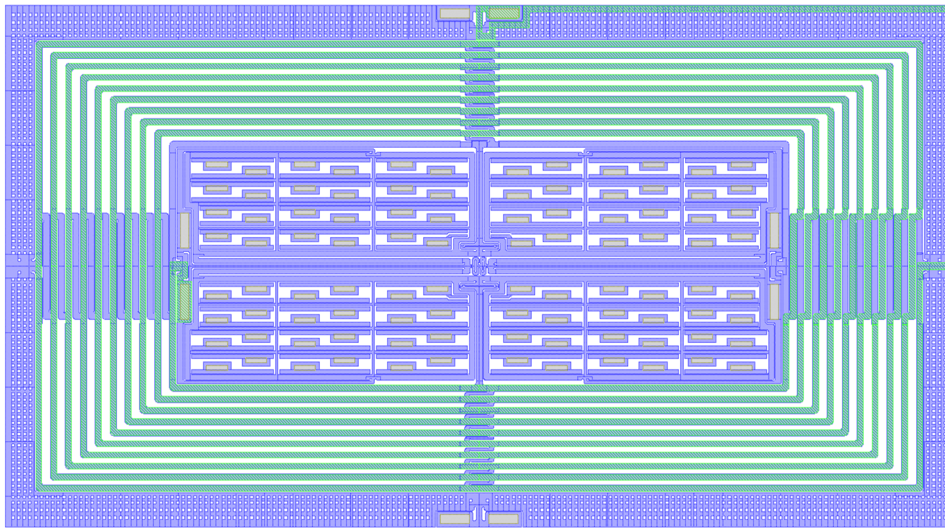

Figure 5.9: *2D CAD layout for masks definition of polysilicon (blue), metal (green) and anchor (gray) layers*

Figure 5.10 shows the layout of the complete designed module. The presented layers are used to define all the masks needed for the device fabrication. All the electrical interconnections between MEMS structures and external pads are also put in evidence. The complete module features two 3-axis monolithic magnetometers and one Tang resonator, which is very similar to the one presented in section 3.2.5, with dimensions and springs modified in order to target the new driving frequency (48.4 kHz). The two magnetometers have the following characteristics:

- The first (3AX MAG 1) is exactly the one presented in this chapter;
- The second (3AX MAG 2) is nearly identical to the previous one, but it does not feature the tuning electrodes. This in order to maximize

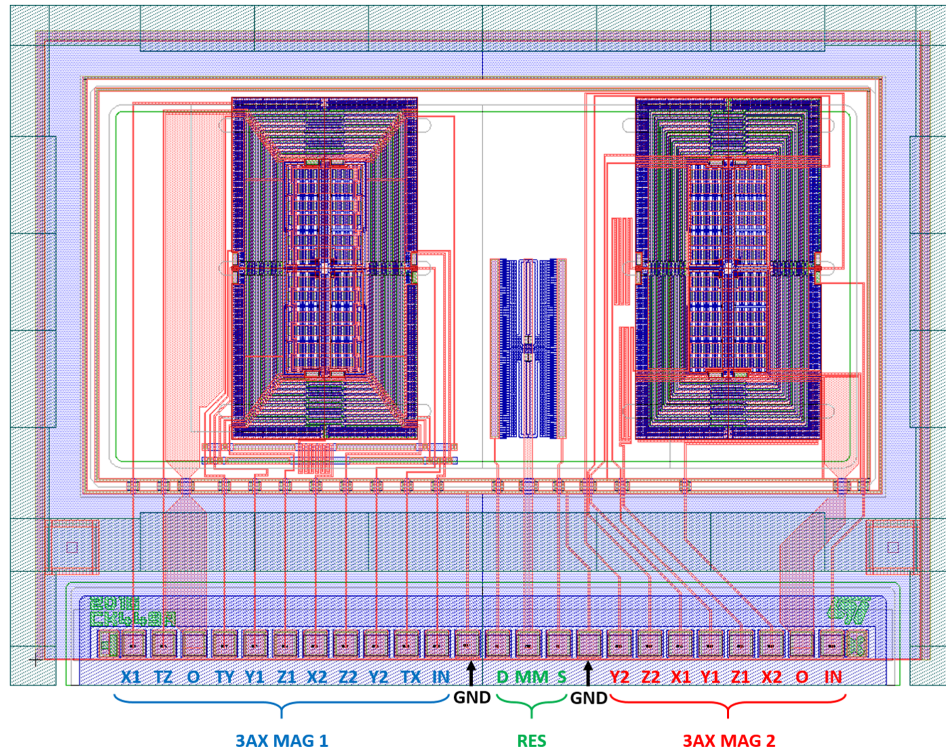

Figure 5.10: *2D CAD layout for masks definition of all the relevant layer for its fabrication with ThELMA process of STMicroelectronics. In red is shown the heavily-doped polysilicon layer used to create sensing electrodes for the torsional modes and all the electrical interconnections between the structure and the external pads.*

the sensing capacitances of all the three axes, and thus the sensitivity of the device (which is needed to make the electronics noise negligible). It also targets slightly different resonance frequencies for the three modes: in particular they are about 200 Hz higher with respect to the first implementation. The lack of tuning electrodes, indeed, forces the resonance frequencies to be directly tuned by means of the sensing electrodes voltages. An increase of these voltages affects both the resonance frequencies (decreasing them) and the sensitivities (increasing them) of the three axes. For this reason - due to possible process variations that could affect in a different way sensor and resonator - it has been preferred to risk of obtaining sensor frequencies higher than the target value for the correct mismatch. In this way, even in the worst case, the target frequency mismatch could be obtained increasing the electrodes voltages, thus not decreasing the device sensitivity.

At the time of this writing the masks layout have been sent to STMicroelectronics and the devices are under fabrication process.

In the next months the drive and sense electronics should be adapted (e.g. changing the filters for the feedthrough compensation of the oscillator circuit) for the higher working frequency of the new system.

A complete characterization of the device have then to be carried out, exploiting the same setup and routines presented in chapter 4, with the purpose of experimentally validating its working principle and performance.

Possible issues of the presented device, or possibly improvements to it, should be identified or developed in order to enhance its performance and make it become more and more closer to commercialization.

5.4.2 Further performance improvements

As visible in figure 5.3, the designed device does not fit the area constraints of section 5.1. Exploiting the same process presented in section 3.1, without an insulating layer between aluminum and polysilicon, and complying with the dimensional constraints on the minimum metal width, performances would not be maintained with a smaller structure. The purpose of this device is indeed the demonstration of the 3-axis single-mass structure for Lorentz-Force based magnetic field detection, with a 10-fold improvement in terms of area occupation with respect to the previous implementation of chapter 3.

Referring to figure 5.11, in future designs, with smaller metal widths and the presence of an insulating layer, more than one metal strip could be deposited on the same poly-silicon block. Therefore, even better performance could be achieved with a very similar, but smaller, structure. The isolation of the two layers also opens the possibility to bias the moving mass instead of the stators. This technique, already exploited in gyroscopes [51], allows to provide about 15V to 20V to the polysilicon layer, enhancing the charge flow through the stators, which in turn need no bias (or a very small one). The possibility of biasing the moving mass with a constant voltage would also eliminate some offset sources (as the electrical one described in section 2.3) and attenuate some others, as the feed-through one described in section 2.3.2. Moreover, in the hypothesis of a stack of insulator-metal layers, performance, both in terms of sensitivity and noise, would be increased without any impact on area occupation and power consumption. The process implementation which would allow the feasibility of this enhanced structure is under development, and some concrete possibilities have already been proposed.

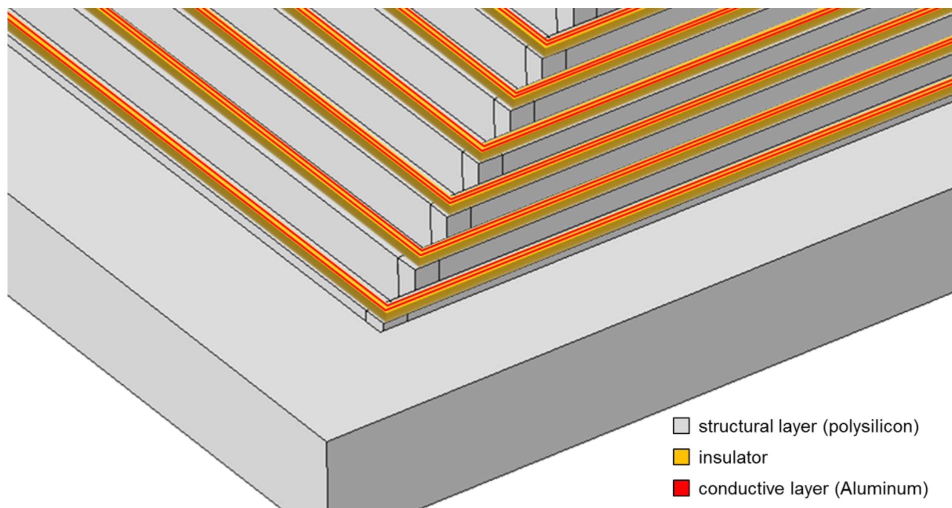

Figure 5.11: *With smaller minimum metal width, more than one strip can be deposited on top of the same polysilicon block, if covered by an insulating layer. This would enhance the performance of the device without impacting neither on the area occupation nor on power consumption.*

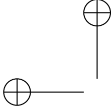
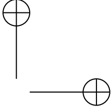

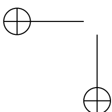

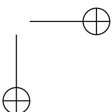

Conclusions

The work deeply analyzed strengths and issues of consumer-grade Lorentz-Force MEMS magnetic field sensors. It gave design and operation criteria to be followed, showing that performance beyond the state of the art of commercial (not MEMS) magnetometers can be reached exploiting a standard industrial process, opening the way to the fabrication of all-MEMS multi-axis IMUs.

Validation of the innovative design concepts and operation techniques, as well the achievement of performance beyond the state of the art, have been demonstrated on a 3-axis prototype composed by three different uniaxial structures, which however does not fit the requirements for small area occupation of consumer application.

A solution to this point has been proposed in chapter 5 by designing a monolithic 3-axis structure, which allows a 15-fold saving in terms of area occupation, and it is estimated to perform even better than the one presented and fully characterized in chapter 3 and 4.

Moreover, the possibility of inserting an insulating layer between the metal and the structural one would guarantee a huge performance increase. It enables the possibility to directly bias the moving mass, a technique already exploited in gyroscopes, which allows both to improve the sensitivity and to reduce the offset. It also makes possible to put more than one metal path onto the same polysilicon block.

In the hypothesis of using the same structure as the one of chapter 5, with isolated metal layer with smaller minimum width and 20 V applied to the moving mass, 30 and 40 current loops becomes available for Y- and

Z-axis, and X-axis respectively, as the latter can also exploit the external frame motion. In these conditions, navigation-grade performance can be obtained, as shown in tables 5.5 and 5.6, which can easily be doubled (or even more) if a stack of insulating-metal layer could be fabricated.

Axis	$\mathbf{SF_C}$ [aF/(mT)]	$\mathbf{\Delta C_{FSR}}$ [fF]	$\mathbf{SF_V}$ [μV/(μTμA$_{rms}$)]
X	465	2.3	37.6
Y	740	3.7	59.8
Z	511	2.6	41.3

Table 5.5: *Estimated value for the sensitivities of the three axes in the hypothesis of an insulating layer between metal and polysilicon.*

Axis	**Thermo-Mechanical** [nT/$\sqrt{\text{Hz}}$]	**Op-Amp Voltage** [nT/$\sqrt{\text{Hz}}$]	**Feedback Resistance** [nT/$\sqrt{\text{Hz}}$]	**Total** [nT/$\sqrt{\text{Hz}}$]	**FOM** [μTμA$_{rms}$ /$\sqrt{\text{Hz}}$]	**Resolution @ 25Hz** [nT]
X	39	6	2	**40**	1.3	265
Y	24	3	1	**24**	0.8	120
Z	39	5	1	**39**	1.3	195

Table 5.6: *Estimated noise contributions and minimum detectable magnetic field for a 25Hz bandwidth for the three axes in the hypothesis of an insulating layer between metal and polysilicon.*

From one side it is clear that the performance achieved by this sensor satisfy the target required for the state of the art consumer applications (e.g. navigation). From the other side technological progress, which could allow the 3-D fabrication of insulator-metal layer stack, would open the doors for Lorentz-Force based MEMS magnetometers to other applications (e.g. medical) which require better performance with respect to consumer field.

Despite thousand of research years, magnetic field sensing is still an open field, with more applications as much technology makes it progress. Even in consumer application, the way towards miniaturization and resolution enhancement is never ending, and MEMS devices represent a very promising alternative. Concurrent technologies have been under research for more than five decades, but MEMS magnetometers have already almost reached their performance, giving a superior advantage in the view of integration of multi-sensing platforms in devices that will definitely continue to dwindle.

Bibliography

[1] W. Lowrie. *Fundamentals of Geophysics*. Cambridge University Press, 2007.

[2] J. Lenz and S. Edelstein. Magnetic sensors and their applications. *IEEE Sensors Journal*, 6(3):631–649, June 2006.

[3] M.J. Caruso, C.H. Smith, T. Bratland and R. Schneider. A New Perspective on Magnetic Field Sensing. 1998.

[4] S. Tumanski. *Thin Film Magnetoresistive Sensors*. Institute of Physics Publishing, Bristol and Philadelphia, 2000.

[5] R.S. Popovic. *Hall effect devices*. Institute of Physics Publishing, Bristol and Philadelphia, 2004.

[6] P. Ripka. *Sensors: Advancements in Modeling, Design Issues, Fabrication and Practical Applications*. Springer, 2008.

[7] A. Baschirotto and F. Borghetti and E. Dallago and P. Malcovati and M. Marchesi and E. Melissano and P. Siciliano and G. Venchi. Fluxgate magnetic sensor and front-end circuitry in an integrated microsystem. *Sensors and Actuators A: Physical*, 132(1):90 – 97, 2006.

[8] Ashai Khasei. *AK8963, Operating Manual*, 2013. available online at https://www.akm.com/akm/en/file/datasheet/AK8963C.pdf.

[9] Ashai Khasei. *AK09911, Operating Manual*, 2014. available online at https://www.akm.com/akm/en/file/datasheet/AK09911C.pdf.

[10] Bosch. *BMM150, Operating Manual*, 2013. available online at https://ae-bst.resource.bosch.com/media/_tech/media/datasheets/BST-BMM150-DS001-01.pdf.

[11] Freescale. *MAG3110, Operating Manual*, 2013. available online at https://www.nxp.com/files/sensors/doc/data_sheet/MAG3110.pdf.

[12] Honeywell. *HMC5883L, Operating Manual*, 2013. available online at https://aerospace.honeywell.com/~/media/aerospace/files/datasheet/3-axisdigitalcompassichmc5883l_ds.pdf.

[13] MEMSIC. *MMC3316xMT, Operating Manual*, 2012. available online at http://www.memsic.com/userfiles/files/Datasheets/Magnetic-Sensors-Datasheets/MMC3316xMT-Rev-B.pdf.

[14] STMicroelectronics. *LIS3MDL, Operating Manual*, 2015. available online at http://www.st.com/content/ccc/resource/technical/document/datasheet/54/2a/85/76/e3/97/42/18/DM00075867.pdf/files/DM00075867.pdf/jcr:content/translations/en.DM00075867.pdf.

[15] Yamaha. *YAS537, Operating Manual*, 2014. available online at http://www.willow.co.uk/html/components/com_virtuemart/shop_image/product/Duplicates/pdfs/MS-3T_YAS537_PBAS537A-000-01-e_Jul15.pdf.

[16] Alps Electrics. *HSCDTD008A, Operating Manual*. available online at http://www.alps.com/prod/info/E/HTML/Sensor/Geomagnetic/HSCD/HSCDTD008A.html.

[17] Bosch. *BMC156, Operating Manual*, 2014. available online at https://ae-bst.resource.bosch.com/media/_tech/media/datasheets/BST-BMC156-DS000-01.pdf.

[18] Freescale. *FXOS8700CQ, Operating Manual*, 2016. available online at http://cache.nxp.com/files/sensors/doc/data_sheet/FXOS8700CQ.pdf?fpsp=1&WT_TYPE=DataSheets&WT_VENDOR=FREESCALE&WT_FILE_FORMAT=pdf&WT_ASSET=Documentation&fileExt=.pdf.

[19] Kionix. *KMX62, Operating Manual*, 2016. available online at http://kionixfs.kionix.com/en/datasheet/KMX62-1031SpecificationsRev2.0.pdf.

[20] mCube. *MC6470, Operating Manual*, 2016. available online at http://www.mcubememes.com/wp-content/uploads/2016/03/MC6470-Preliminary-Datasheet-APS-048-0033v1.5.pdf.

[21] STMicroelectronics. *LSM303AGR, Operating Manual*, 2016. available online at http://www.st.com/content/ccc/resource/technical/document/datasheet/74/c4/19/54/62/c5/46/13/DM00177685.pdf/files/DM00177685.pdf/jcr:content/translations/en.DM00177685.pdf.

[22] A.L. Herrera-May, L.A. Aguilera-Cortés, P.J. García-Ramírez and E. Manjarrez. Resonant Magnetic Field Sensors Based On MEMS Technology. *Sensors*, 9(10):7785, 2009.

[23] M. Kok and J. D. Hol and T. B. Schön and F. Gustafsson and H. Luinge. Calibration of a magnetometer in combination with inertial sensors. In *Information Fusion (FUSION), 2012 15th International Conference on*, pages 787–793, July 2012.

[24] F. Camps and S. Harasse and A. Monin. Numerical calibration for 3-axis accelerometers and magnetometers. In *2009 IEEE International Conference on Electro/Information Technology*, pages 217–221, June 2009.

[25] A. S. Edelstein, G. Fischer, J. Pulskamp, M. Pedersen, W. Bernard and S. F. Cheng. Minimizing the effect of 1/f noise with a MEMS flux concentrator. In *Sensors, 2004. Proceedings of IEEE*, pages 1562–1565 vol.3, Oct 2004.

[26] Y. Hui and T. Nan and N. X. Sun and M. Rinaldi. High Resolution Magnetometer Based on a High Frequency Magnetoelectric MEMS-CMOS Oscillator. *Journal of Microelectromechanical Systems*, 24(1):134–143, Feb 2015.

[27] H.H. Yang and N.V. Myung and J. Yee and D.-Y. Park and B.-Y. Yoo and M. Schwartz and K. Nobe and J.W. Judy. Ferromagnetic micromechanical magnetometer. *Sensors and Actuators A: Physical*, 97–98:88 – 97, 2002.

[28] D. DiLella and L.J. Whitman and R.J. Colton and T.W. Kenny and W.J. Kaiser and E.C. Vote and J.A. Podosek and L.M. Miller. A micromachined magnetic-field sensor based on an electron tunneling displacement transducer. *Sensors and Actuators A: Physical*, 86(1–2):8 – 20, 2000.

[29] D. Ettelt and P. Rey and G. Jourdan and A. Walther and P. Robert and J. Delamare. 3D Magnetic Field Sensor Concept for Use in Inertial Measurement Units (IMUs). *Journal of Microelectromechanical Systems*, 23(2):324–333, April 2014.

[30] V. Kempe. *Inertial MEMS Principles and Practice*. Cambridge University Press, 2011.

[31] G. Langfelder, C. Buffa, A. Frangi, A. Tocchio, E. Lasalandra, and A. Longoni. Z-Axis Magnetometers for MEMS Inertial Measurement Units Using an Industrial Process. *IEEE Transactions on Industrial Electronics*, 60(9):3983–3990, Sept 2013.

[32] G. Langfelder and A. Tocchio. Operation of Lorentz-Force MEMS Magnetometers With a Frequency Offset Between Driving Current and Mechanical Resonance. *IEEE Transactions on Magnetics*, 50(1):1–6, Jan 2014.

[33] Z. Kádár, A. Bossche, P.M. Sarro and J.R. Mollinger. Magnetic-field measurements using an integrated resonant magnetic-field sensor. *Sensors and Actuators A: Physical*, 70(3):225 – 232, 1998.

[34] H. Emmerich, M. Schofthaler and U. Knauss. A novel micromachined magnetic-field sensor. In *Micro Electro Mechanical Systems, 1999. MEMS '99. Twelfth IEEE International Conference on*, pages 94–99, Jan 1999.

[35] M. J. Thompson and D. A. Horsley. Parametrically Amplified Z -Axis Lorentz Force Magnetometer. *Journal of Microelectromechanical Systems*, 20(3):702–710, June 2011.

[36] V. Kumar and M. Mahdavi and X. Guo and E. Mehdizadeh and S. Pourkamali. Ultra sensitive lorentz force MEMS magnetometer with pico-tesla limit of detection. In *2015 28th IEEE International Conference on Micro Electro Mechanical Systems (MEMS)*, pages 204–207, Jan 2015.

[37] E. Mehdizadeh, V. Kumar, X. Guo and S. Pourkamali. High-Q Lorentz force MEMS magnetometer with internal self-amplification. In *IEEE SENSORS 2014 Proceedings*, pages 706–709, Nov 2014.

[38] J. Kyynäräinen, J. Saarilahti, H. Kattelus, A. Kärkkäinen, T. Meinander, A. Oja, P. Pekko, H. Seppä, M. Suhonen, H. Kuisma, S. Ruotsalainen, M. Tilli. A 3D micromechanical compass. *Sensors and Actuators A: Physical*, 142(2):561 – 568, 2008.

[39] M. Li and D. A. Horsley. Offset Suppression in a Micromachined Lorentz Force Magnetic Sensor by Current Chopping. *Journal of Microelectromechanical Systems*, 23(6):1477–1484, Dec 2014.

[40] S. Sonmezoglu and D. A. Horsley. Off-resonance operation of a MEMS Lorentz force magnetometer with improved thermal stability of the scale factor. In *2016 IEEE 29th International Conference on Micro Electro Mechanical Systems (MEMS)*, pages 103–106, Jan 2016.

[41] B. Bahreyni and C. Shafai. A Resonant Micromachined Magnetic Field Sensor. *IEEE Sensors Journal*, 7(9):1326–1334, Sept 2007.

[42] M. Li, S. Nitzan and D. A. Horsley. Frequency-Modulated Lorentz Force Magnetometer With Enhanced Sensitivity via Mechanical Amplification. *IEEE Electron Device Letters*, 36(1):62–64, Jan 2015.

[43] W. Zhang and J. E.-Y. Lee. Frequency-based magnetic field sensing using Lorentz force axial strain modulation in a double-ended tuning fork. *Sensors and Actuators A: Physical*, 211:145 – 152, 2014.

[44] M. Li, S. Sonmezoglu and D. A. Horsley. Extended Bandwidth Lorentz Force Magnetometer Based on Quadrature Frequency Modulation. *Journal of Microelectromechanical Systems*, 24(2):333–342, April 2015.

[45] D. Ren, L. Wu, M. Yan, M. Cui, Z. You and M. Hu. Design and Analyses of a MEMS Based Resonant Magnetometer. *Sensors*, 9(9):6951, 2009.

[46] G. Langfelder, G. Laghi, P. Minotti, A. Tocchio and A. Longoni. Off-Resonance Low-Pressure Operation of Lorentz Force MEMS Magnetometers. *IEEE Transactions on Industrial Electronics*, 61(12):7124–7130, Dec 2014.

[47] W. L. Sung, F. Y. Lee, C. L. Cheng, C. I. Chang, E. Cheng and W. Fang. MEMS above CMOS process for single proof-mass 3-AXIS Lorentz-force resonant magnetic sensor. In *2016 IEEE 29th International Conference on Micro Electro Mechanical Systems (MEMS)*, pages 978–981, Jan 2016.

[48] C. I. Chang, M. H. Tsai, Y. C. Liu, C. M. Sun and W. Fang. Development of multi-axes CMOS-MEMS resonant magnetic sensor using Lorentz and electromagnetic forces. In *Micro Electro Mechanical Systems (MEMS), 2013 IEEE 26th International Conference on*, pages 193–196, Jan 2013.

[49] A.L. Herrera-May, P.J. García-Ramírez, L.A. Aguilera-Cortés, E. Figueras, J. Martinez-Castillo, E. Manjarrez, A. Sauceda, L. García-González and R. Juárez-Aguirre. Mechanical design and characterization of a resonant magnetic field microsensor with linear response and high resolution. *Sensors and Actuators A: Physical*, 165(2):399 – 409, 2011.

[50] G. Langfelder, A. Tocchio and D. Paci. Magnetic sensor including a lorentz force transducer driven at a frequency different from the resonance frequency, and method for driving a lorentz force transducer, 2015.

[51] C. Acar, A. Shkel. *MEMS Vibratory Gyroscopes*. Springer, 2009.

[52] A. Frangi, G. Laghi, G. Langfelder, P. Minotti and S. Zerbini. Optimization of Sensing Stators in Capacitive MEMS Operating at Resonance. *Journal of Microelectromechanical Systems*, 24(4):1077–1084, Aug 2015.

[53] T. B. Gabrielson. Mechanical-thermal noise in micromachined acoustic and vibration sensors. *IEEE Transactions on Electron Devices*, 40(5):903–909, May 1993.

[54] M. Tartagni and R. Guerrieri. A fingerprint sensor based on the feedback capacitive sensing scheme. *IEEE Journal of Solid-State Circuits*, 33(1):133–142, Jan 1998.

[55] Jiangfeng Wu and G. K. Fedder and L. R. Carley. A low-noise low-offset capacitive sensing amplifier for a 50- mu;g/ radic;Hz monolithic CMOS MEMS accelerometer. *IEEE Journal of Solid-State Circuits*, 39(5):722–730, May 2004.

[56] E. Tatar and S. E. Alper and T. Akin. Quadrature-Error Compensation and Corresponding Effects on the Performance of Fully Decoupled MEMS Gyroscopes. *Journal of Microelectromechanical Systems*, 21(3):656–667, June 2012.

[57] R. Antonello and R. Oboe and L. Prandi and C. Caminada and F. Biganzoli. Open loop compensation of the quadrature error in MEMS vibrating gyroscopes. In *Industrial Electronics, 2009. IECON '09. 35th Annual Conference of IEEE*, pages 4034–4039, Nov 2009.

[58] M. Li and V. T. Rouf and M. J. Thompson and D. A. Horsley. Three-Axis Lorentz-Force Magnetic Sensor for Electronic Compass Applications. *Journal of Microelectromechanical Systems*, 21(4):1002–1010, Aug 2012.

[59] G. Langfelder and S. Dellea and F. Zaraga and D. Cucchi and M. Azpeitia Urquia. The Dependence of Fatigue in Microelectromechanical Systems on the Environment and the Industrial Packaging. *IEEE Transactions on Industrial Electronics*, 59(12):4938–4948, Dec 2012.

[60] G. Langfelder and A. Caspani and A. Tocchio. Design Criteria of Low-Power Oscillators for Consumer-Grade MEMS Resonant Sensors. *IEEE Transactions on Industrial Electronics*, 61(1):567–574, Jan 2014.

[61] B. R. Simon and A. A. Trusov and A. M. Shkel. Anti-phase mode isolation in tuning-fork MEMS using a lever coupling design. In *Sensors, 2012 IEEE*, pages 1–4, Oct 2012.

[62] H. Weinberg. *Gyro mechanical performance: The most important parameter*. Analog Devices Tech. Article, vol. 2158, pp. 4938–4948, Sep. 2011.

[63] M. M. Turner. Verification of particle-in-cell simulations with Monte Carlo collisions against exact solutions of the Boltzmann-Poisson equations. In *2015 IEEE International Conference on Plasma Sciences (ICOPS)*, pages 1–1, May 2015.

[64] P. Minotti and S. Brenna and G. Laghi and A. G. Bonfanti and G. Langfelder and A. L. Lacaita. A Sub-400-nT/$\sqrt{Hz}$, 775-μW , Multi-Loop MEMS Magnetometer With Integrated Readout Electronics. *Journal of Microelectromechanical Systems*, 24(6):1938–1950, Dec 2015.

[65] W. C. Tang and T. C. H. Nguyen and R. T. Howe. Laterally driven polysilicon resonant microstructures. In *Micro Electro Mechanical Systems, 1989, Proceedings, An Investigation of Micro Structures, Sensors, Actuators, Machines and Robots. IEEE*, pages 53–59, Feb 1989.

[66] C. T. C. io and R. T. Howe. An integrated CMOS micromechanical resonator high-Q oscillator. *IEEE Journal of Solid-State Circuits*, 34(4):440–455, Apr 1999.

[67] G. Laghi and C. R. Marra and P. Minotti and A. Tocchio and G. Langfelder. A 3-D Micromechanical Multi-Loop Magnetometer Driven Off-Resonance by an On-Chip Resonator. *Journal of Microelectromechanical Systems*, 2016.

[68] G. Laghi. *Ottimizzazione della geometria e delle prestazioni di magnetometri MEMS tramite innovative tecniche di pilotaggio della corrente*. Master Thesis, 2013.

[69] Analog Devices. *AD8065, Datasheet*. available online at `http://www.analog.com/media/en/technical-documentation/data-sheets/AD8065_8066.pdf`.

[70] Texas Instruments. *INA129, Datasheet*. available online at `http://www.ti.com/lit/ds/symlink/ina129.pdf`.

[71] A. Sharma and M. F. Zaman and F. Ayazi. A 104-dB Dynamic Range Transimpedance-Based CMOS ASIC for Tuning Fork Microgyroscopes. *IEEE Journal of Solid-State Circuits*, 42(8):1790–1802, Aug 2007.

[72] J. Raman and E. Cretu and P. Rombouts and L. Weyten. A Closed-Loop Digitally Controlled MEMS Gyroscope With Unconstrained Sigma-Delta Force-Feedback. *IEEE Sensors Journal*, 9(3):297–305, March 2009.

[73] Analog Devices. *AD8276, Datasheet*. available online at `http://www.analog.com/media/en/technical-documentation/data-sheets/AD8276_8277.pdf`.

[74] G. A. Bird. *Molecular Gas Dynamics and the Direct Simulation of Gas Flows*. Oxford, U.K.: Clarendon, 1994.

[75] Williams, R. M. M. A review of the rarefied gas dynamics theory associated with some classical problems in flow and heat transfer. *Zeitschrift für angewandte Mathematik und Physik ZAMP*, 52(3):500–516, 2001.

[76] Gad-el-Hak, M. The Fluid Mechanics of Microdevices—The Freeman Scholar Lecture. *Journal of Fluids Engineering*, 121(1):5–33, 1999.

[77] Frangi, A. and Frezzotti, A. and Lorenzani, S. On the Application of the BGK Kinetic Model to the Analysis of Gas-structure Interactions in MEMS. *Comput. Struct.*, 85(11-14):810–817, June 2007.

[78] M. A. Gallis and J. R. Torczynski. An improved Reynolds-equation model for gas damping of microbeam motion. *Journal of Microelectromechanical Systems*, 13(4):653–659, Aug 2004.

Bibliography

[79] H. Sumali. Squeeze-film damping in the free molecular regime: model validation and measurement on a MEMS. *Journal of Micromechanics and Microengineering*, 17(11):2231, 2007.

[80] M. Bao and H. Yang and H. Yin and Y. Sun. Energy transfer model for squeeze-film air damping in low vacuum. *Journal of Micromechanics and Microengineering*, 12(3):341, 2002.

[81] T. Veijola and A. Pursula and P. Råback. Extending the validity of squeezed-film damper models with elongations of surface dimensions. *Journal of Micromechanics and Microengineering*, 15(9):1624, 2005.

[82] A. Frangi and A. Ghisi and L. Coronato. On a deterministic approach for the evaluation of gas damping in inertial {MEMS} in the free-molecule regime. *Sensors and Actuators A: Physical*, 149(1):21 – 28, 2009.

[83] A. Frangi and P. Fedeli and G. Laghi and G. Langfelder and G. Gattere. Near Vacuum Gas Damping in MEMS: Numerical Modeling and Experimental Validation. *Journal of Microelectromechanical Systems*, 2016.

[84] Invensense Inc. *MPU9255, Operating Manual*, 2015. available online at `https://www.invensense.com/products/motion-tracking/9-axis/mpu-9255-2/`.

[85] D. W. Allan. Statistics of atomic frequency standards. *Proceedings of the IEEE*, 54(2):221–230, Feb 1966.

[86] M. Vágner and P. Beneš and Z. Havránek. Experience with Allan variance method for MEMS gyroscope performance characterization. In *Instrumentation and Measurement Technology Conference (I2MTC), 2012 IEEE International*, pages 1343–1347, May 2012.

[87] B. Kim and M. A. Hopcroft and R. N. Candler and C. M. Jha and M. Agarwal and R. Melamud and S. A. Chandorkar and G. Yama and T. W. Kenny. Temperature Dependence of Quality Factor in MEMS Resonators. *Journal of Microelectromechanical Systems*, 17(3):755–766, June 2008.

[88] ITmems s.r.l. *MCP-G, Product Specification*, 2015. available online at `http://www.itmems.it`.

[89] M. Kok and J. D. Hol and T. B. Schön and F. Gustafsson and H. Luinge. Calibration of a magnetometer in combination with inertial sensors. In *Information Fusion (FUSION), 2012 15th International Conference on*, pages 787–793, July 2012.